

**THE UNIVERSITY OF READING**

***Long-Path Scintillometry over Complex Terrain to  
Determine Areal-Averaged Sensible and Latent Heat  
Fluxes***

**PhD Thesis**

**Soil Science Department**

**Jonathan G Evans**

**April 2009**

## **Abstract**

Landscape scale measurements (1 - 10 km<sup>2</sup>) of sensible and latent heat fluxes over heterogeneous areas are required for hydrological and meteorological modelling. Evaporation is strongly dependent on land surface properties, thus aggregating field-scale measurements has much uncertainty because of the need for detailed land-cover maps and the possible disproportionate contribution of vegetation transition zones; in any case, such a collection of field-scale instruments is a highly resource intensive approach. A potentially better alternative is reported here: the long-path (large aperture) scintillometer (LAS) has been used over topographically complex chalk downland with mixed vegetation, to measure the sensible heat fluxes at the landscape scale, using a 2.4 km pathlength. These sensible heat fluxes agreed well with aggregated eddy covariance measurements made at the field scale for different vegetation types – the contrasting range of sensible heat fluxes in the late summer over various agricultural fields in southern England is reported.

The LAS in combination with a new custom-built millimetre-wave (94 GHz) scintillometer (MWS) was trialled to measure large-scale area averaged latent and sensible heat fluxes, using the two-wavelength method of scintillometry, over the same complex terrain. The LAS-MWS fluxes were found to close the energy balance well, except during periods of either high windspeed or very low cross-wind conditions. The

latter conditions may lead to inappropriate filtering or reach a fundamental limitation of the method. The over-estimation of flux at high windspeeds may be due to limitations of the Monin-Obukhov similarity theory which was developed for homogeneous surfaces.

The difference in the effective heights of the two scintillometers for the measurement of their respective fluxes is recognised, and the formula for these heights is derived. Application over certain complex topography shows that an increased measurement height would lead to better-matched source areas for the LAS and MWS.

## Declaration

I confirm that this is my own work and the use of all material from other sources has been properly and fully acknowledged.

In loving memory of my brother,

Simon Lawrence Evans

8<sup>th</sup> February 1966 – 5<sup>th</sup> September 2009

# Table of Contents

Table of Contents.....	i
Table of Figures .....	vii
Table of Tables .....	xiii
Acknowledgements.....	xiv
Chapter 1 Introduction.....	1
Chapter 2 Scintillometry Theory for Sensible and Latent Heat Flux Measurements .....	11
2.1 Overview of Theory.....	11
2.2 Turbulence Theory.....	13
2.3 Electromagnetic Wave Propagation in the Turbulent Atmosphere... 18	
2.3.1 Aperture Averaging of the Large Aperture Scintillometer .....	24
2.3.2 Path Weighting Functions.....	26
2.4 Measuring Structure Parameters by Scintillometry.....	29
2.4.1 The Standalone Near-infrared LAS to Measure $C_T^2$ .....	30

2.4.2	Two-wavelength Scintillometry .....	32
2.4.3	Two-Wavelength Scintillometry with Bichromatic Covariance ..	33
2.5	Sensible and Latent Heat Fluxes from Structure Parameters: the Application of MOST.....	34
2.6	Theoretical Turbulence Spectra Measured by Scintillometers .....	38
2.6.1	The Theoretical Spectrum of the MWS.....	38
2.6.2	The Theoretical Spectrum of the LAS.....	46
2.6.3	Sensitivity of Scintillometers to Eddy Size .....	49
Chapter 3	Evaporation and Sensible Heat Fluxes Measured with a Large Aperture Scintillometer Over Undulating, Mixed Agricultural Terrain .....	52
3.1	Introduction.....	52
3.2	Measurements and Methods .....	56
3.2.1	LAS Measurements .....	56
3.2.2	Meteorological and Soil Measurements.....	60
3.2.3	EC Measurements.....	62
3.2.4	LAS Effective Height and Source Area Analysis.....	64
3.2.5	Data Quality Control .....	68

3.3	Results.....	69
3.3.1	EC Performance .....	69
3.3.2	Field EC Measurements Compared with the LAS Sensible Heat Fluxes .....	72
3.3.3	LAS Sensible Heat Fluxes Compared with Aggregated EC Sensible Heat Fluxes .....	76
3.3.4	Latent Heat Fluxes Estimated from the LAS Compared with Aggregated EC Measurements.....	77
3.3.5	Diurnal variations.....	78
3.4	Discussion .....	81
3.5	Conclusion.....	85
Chapter 4	The Effective Height for the Calculation of Heat Fluxes from Scintillometry over Complex Topography.....	88
4.1	Introduction.....	88
4.2	Structure Parameter Dependency on Height.....	90
4.3	Approximate Path Weighting Functions for the LAS and MWS .....	93
4.4	Results of the Effective Height Calculations .....	94
4.4.1	Flat Topography and Slanted Paths .....	94

4.4.2	A Case Study over Complex Topography at Sheepdrove Organic Farm.....	94
4.5	The Effective Height Scaling of $C_{n^2\_LAS}$ for the Calculation of $C_{Q^2}$ ...	96
4.5.1	The Calculated Values of $C_{n^2\_LAS}$ Scaling Factor ( $J_{LAS}$ ) .....	97
4.6	Discussion of $z_{efH}$ and $z_{efLE}$ .....	98
Chapter 5 Sensible and Latent Heat Flux Measurements over Complex Terrain by Two-wavelength Scintillometry.....		
		102
5.1	Introduction.....	102
5.2	Design Specification of the MWS.....	105
5.3	Measurements and Methods .....	108
5.4	Results.....	112
5.4.1	MWS Spectra .....	113
5.4.2	Weather Conditions .....	118
5.4.3	Measured $C_{n^2\_LAS}$ and $C_{n^2\_MWS}$ .....	120
5.4.4	Sensible and Latent Heat Fluxes.....	123
5.5	Discussion .....	131

5.6	Conclusions .....	139
Chapter 6	Discussion .....	142
6.1	Overview.....	142
6.2	The Assumptions Required to Measure Structure Parameters by Scintillometry .....	144
6.3	Structure Parameter-Flux MOST Relationships.....	146
6.4	The Determination of the Effective Heights .....	148
6.5	Determining a Source-area-averaged Friction Velocity .....	149
6.6	The Estimation of the Scintillometer Source Area.....	150
6.7	Calibration of Scintillometers .....	151
6.8	LAS-MWS Filtering: Water Vapour Absorption and the Case of Near-zero Crosswind speeds .....	154
6.9	Closure of the Surface Energy Balance.....	156
6.10	Recommended Measurement Strategies and Future Work.....	158
Appendix 1:	Eddy Covariance Data Processing.....	162
A1.1:	Exploration of the Planar Fit Method for EC Processing .....	162
A1.2:	The Relative Contribution of Eddy Covariance Processing Steps...	164

A1.3: Validation of EC Measurements by Closure of the Surface Energy  
Balance ..... 170

References..... 175

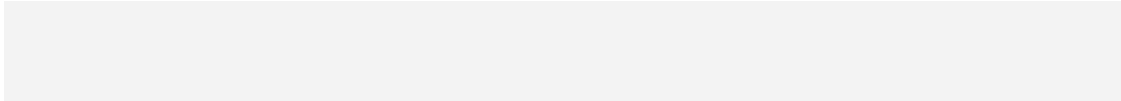


## Table of Figures

Figure 2-1 Path weighting functions for the SAS (e.g. MWS) and for the LAS.  
 .....28

Figure 2-2 Calculated theoretical temporal power spectral density of the MWS:  
 solid line is the refraction contribution (without absorption); the dotted line  
 is the absorption contribution; the dot-dash line shows the resultant of  
 absorption and refraction (where this deviates from the solid line below  
 0.01 Hz); the dashed line is a reference line of slope -8/3; crosswind  
 speed = 5 m s<sup>-1</sup>, pathlength = 2.43 km,  $C_{n^2R} = 5 \times 10^{-14} \text{ m}^{-2/3}$ , and  $C_{n^2I} = 1$   
 $\times 10^{-20} \text{ m}^{-2/3}$ . .....44

Figure 2-3 Calculated theoretical temporal power spectral density of the MWS  
 for different crosswind speeds, without absorption. (Pathlength = 2.43 km,  
 $C_{n^2R} = 5 \times 10^{-14} \text{ m}^{-2/3}$ ). .....44

Figure 2-4 Calculated theoretical intensity variance spectra of the MWS for  
 different crosswind speeds, without absorption. (Pathlength = 2.43 km,  
 $C_{n^2R} = 5 \times 10^{-14} \text{ m}^{-2/3}$ ). .....45

Figure 2-5 Calculated theoretical temporal power spectral density of the LAS:  
 solid line is the refraction contribution; the dotted line is the absorption  
 contribution; the dot-dash line is absorption and refraction (where this  
 deviates from the solid line below 0.1 Hz); the dashed reference line has

slope = -12/3; crosswind speed = 5 m s<sup>-1</sup>, pathlength = 2.43 km,  $C_{n^2R\_LAS} = 1 \times 10^{-14} \text{ m}^{-2/3}$ , and  $C_{n^2I\_LAS} = 1 \times 10^{-24} \text{ m}^{-2/3}$ . .....48

Figure 2-6 Normalised integrand of the path weighting function for the MWS, evaluated at centre of path ( $\gamma = 0.5$ , solid line) and  $\gamma = 0.25$  (dashed line), both normalised with total integral for  $\gamma = 0.5$ . The dash-dot line shows the absorption contribution ( $\gamma = 0.5$ ), normalised with its integral – Note this does *not* indicate the relative magnitude of absorption with respect to refraction scintillations, only the wavenumber dependence of each. ....50

Figure 2-7 Normalised integrand of the path weighting function for the LAS, evaluated at centre of path ( $\gamma = 0.5$ , solid line) and  $\gamma = 0.25$  (dashed line), both normalised with total integral for  $\gamma = 0.5$ . The dash-dot line shows the absorption contribution ( $\gamma = 0.5$ ), normalised with its integral – Note this does *not* indicate the relative magnitude of absorption with respect to refraction scintillations, only the wavenumber dependence of each. ....51

Figure 3-1 Map of Sheepdrove Organic Farm showing field instrument locations and LAS transmitter to receiver path (dark green indicates valleys, light green ridges). .....56

Figure 3-2 View from LAS receiver at Stancombe Reservoir .....58

Figure 3-3 LAS 2.4 km path setup at Sheepdrove Organic Farm .....59

Figure 3-4 Winter Wheat (WW) Radiometers (left) and EC Flux Station (right).  
.....63

Figure 3-5 The vertical profile of the land surface (black line) directly beneath the LAS path (red line).....65

Figure 3-6 Typical LAS source area strength contour map overlaid on the field instrument map. The instrument locations are denoted: GC - grass/red clover; GP – grass pasture; SW – spring wheat; WW – winter wheat; WS – weather station. The LAS path is shown as the solid blue line. The aerial photograph is earlier than 2004 with different land cover. Typical condions are south-westerley wind direction and  $L_{Ob} = -67$  .....67

Figure 3-7  $H_{LAS}$  regressions for each  $H_{EC}$ : grass pasture (GP, green), grass/red clover (GC, yellow), spring wheat (SW, red), and winter wheat (WW, black); from 30<sup>th</sup> July to 16<sup>th</sup> August 2004.....72

Figure 3-8 Short chronological periods of  $H_{LAS}$  compared with grass/red clover (GC)  $H_{EC}$ , showing the change in the regression slope over time. Note data with  $H_{EC} > 20 \text{ W m}^{-2}$  were selected to avoid the sign ambiguity in the determined  $H_{LAS}$  values.....74

Figure 3-9  $H_{LAS}$  compared with  $H_{EC\_Agg}$  (31<sup>st</sup> July to 16<sup>th</sup> August 2004);  
 $H_{LAS} = 0.98 \times H_{EC\_Agg} + 7.0, r^2 = 0.93$ .....76

Figure 3-10  $LE_{LAS}$  compared with  $LE_{EC\_Agg}$ ;  $LE_{LAS} = 0.96 \times LE_{EC\_Agg} - 2.7, r^2 = 0.90$ .....78

Figure 3-11 Diurnal course of sensible heat fluxes, showing high inter-field variability and close agreement of LAS with aggregated EC sensible heat flux. ....79

Figure 3-12 Diurnal  $LE_{LAS}$  compared with  $LE_{EC\_Agg}$  (top panel). Net radiation and ground heat flux (bottom panel). ....80

Figure 4-1 Sensitivities to structure parameters for the Sheepdrove Organic Farm scintillometer path (refer to text for full explanation). (1) The ‘Combined relative path weighting’ is defined here as  $G(\gamma).z(\gamma)^{-4/3}$  i.e. the path weighting function multiplied by the dependence of  $C_{n^2}$  on  $z$ , for free convection conditions.....95

Figure 5-1 The Kipp and Zonen LAS 150 (left) and the CEH-RAL MWS (right) – the LAS-MWS two-wavelength scintillometer system. Shown is the receiver site at Stancombe Reservoir. .... 109

Figure 5-2 Photograph (pre-2003), with overlay of typical LAS source area to SW of path (blue line), weather station (WS), grass pasture (GP) and Melville’s Trees (MT) EC stations. .... 110

Figure 5-3 The Sheepdrove Organic Farm scintillometer source area loo... 113

Figure 5-4 Power spectral density (PSD) versus frequency for the unfiltered MWS receiver signal, compared with the expected Kolmogorov slope of -8/3 (black line), with high crosswind speed ( $7.3 \text{ m s}^{-1}$ )..... 115

Figure 5-5 MWS frequency (f) spectrum for high crosswind speed ( $7.3 \text{ m s}^{-1}$ ), showing that most of the signal variance due to turbulence is between 0.1 and 10 Hz, with MWS noise evident between 10 and 20 Hz..... 116

Figure 5-6 Power spectral density versus frequency for the unfiltered MWS receiver signal, compared with the expected Kolmogorov slope of  $-8/3$  (black line), with low crosswind speed ( $1.1 \text{ m s}^{-1}$ )..... 117

Figure 5-7 The MWS frequency (f) spectrum for low crosswind speed ( $1.1 \text{ m s}^{-1}$ ), showing that most of the signal variance which is due to turbulence is below 2 Hz. The MWS noise is evident between 2 - 10 Hz..... 118

Figure 5-8 The weather conditions during the Sheepdrove 2006 Two-wavelength Scintillometer Experiment. Rain rate and wind direction are indicated by blue lines..... 119

Figure 5-9  $C_{T^2}$  and  $C_{Q^2}$  measured by the LAS and LAS-MWS combination respectively..... 121

Figure 5-10 Mean transmission and  $C_n^2$  time-series for the LAS and the MWS. .... 122

Figure 5-11 Comparison of LAS with EC measured sensible heat flux, for Melville's Trees (black circles) and Grass Pasture (red triangles). There is a high correlation ( $r^2 = 0.82$ ), with a slope of 1.14 and offset of  $28 \text{ W m}^{-2}$  for Melville's Trees. For GP,  $r^2 = 0.79$  with a slope of 1.65 and offset of  $14 \text{ W m}^{-2}$ . .... 124

Figure 5-12 The energy balance for the first period (between 17/6/2006 and 25/6/2006, blue points) and the second period (between 26/6/2006 and 3/7/2006, red triangles). The first period energy balance closure has a slope of 1.00, and  $r^2$  of 0.78; for the second period, the slope is 0.91, and  $r^2$  is 0.77; the offsets are  $31 \text{ W m}^{-2}$  and  $7.5 \text{ W m}^{-2}$ , respectively. .... 126

Figure 5-13 Time series of energy balance components:  $H_{LAS}$ ,  $L_v E_{MWS}$  and  $R_n - G$ ; first period. .... 127

Figure 5-14 Time series of energy balance components:  $H_{LAS}$ ,  $L_v E_{MWS}$  and  $R_n - G$ ; second period. .... 128

Figure 5-15 The sensible heat flux fraction of available energy for EC and LAS measurements. .... 130

Figure 5-16 Comparison of  $u_*$  from LAS iteration and measured by EC. .... 131

## Table of Tables

Table 3-1 Summary of In-Field Measurements .....	61
Table 3-2 Contribution to LAS source area by EC vegetation type.....	68
Table 3-3 EC Flux Station Energy Balance Closures.....	70
Table 3-4 Linear regression coefficients by land cover type. $H_{LAS} = Slope \times H_{EC} + Offset$ .....	73
Table 3-5 Linear regression coefficients by time period for grass/read clover (GC). $H_{LAS} = Slope \times H_{EC} + Offset$ .....	75

## Acknowledgements

The UK Natural Environment Research Council funded this work under the LOCAR Thematic Programme, and a Blue Skies grant. I gratefully acknowledge the financial and training support of the Centre for Ecology & Hydrology (CEH), Wallingford for enabling my professional development by studying for this PhD.

I would like to warmly thank Henk De Bruin and John Gash for introducing, developing and advising on the applications of scintillometry at CEH. Henk and John, together with my University of Reading supervisor Anne Verhoef, and CEH supervisor Richard Harding, have sustained their commitment to mentoring my scientific development by providing inspiration, insight, discipline, rigour and encouragement. Thanks are also due to Eleanor Blyth for keeping my thesis writing on track in the crucial last few months. I have been privileged to work with, and gain experience from, some of the best scientists in the field of evaporation and micrometeorological research. In particular, I have had the good fortune to work with Henk, who is the leading authority on the application of scintillometry in this field, and is a gifted teacher and mentor – thank you for your generosity as a pre-pensioner; and I look forward to working with you as a pensioner.

The collaboration with John Bradford, Jon Eastment, and Charles Wrench of the Radio Communications Research Unit, Rutherford Appleton Laboratory,

has produced a new Millimetre-Wave Scintillometer (MWS) instrument, which has enabled much of this work; I gratefully acknowledge their contribution and that of all the superb technical staff at Chilbolton.

I have learnt a lot of important skills and theory from the meteorology group at Wageningen University, The Netherlands. In particular, I am grateful for their discoveries on the scintillometers' noise spikes found through collaborative work with Oscar Hartogenesis, Bram van Kesteren and Arnould Moene.

I would especially like to thank all those that have supported my fieldwork both in the field and laboratory, in particular Dave McNeil, Ty Murray and Bruce Main. I am grateful for the additional net radiation and LAI data collected by Ty Murray in 2004. Thanks to Geoff Wicks, Alan Warwick, John White and Cyril Barrett for electronic and mechanical workshop support, and to Roger Wyatt, Ned Hewitt and Amanda Lloyd (the LOCAR Catchment Services Team) for providing the weather station data and other support. Of vital importance to enabling the field experiment, the generosity and enthusiasm of the Kindersleys and all the staff at Sheepdrove Organic Farm is gratefully appreciated – it was a pleasure to be able to work in such a beautiful location. Thanks to Jon Finch and Richard Ellis for their assistance in geographical mapping.

I am indebted to my wife, Ally, for her patient support and her continued hard work in maintaining family life whilst I disappeared into the study – thank you, and to Ben for providing a welcome distraction. I would also like to thank all my good friends and colleagues for their fantastic friendship and support.

# Chapter 1 Introduction

Evaporation is one of the major components of the catchment water balance, and yet its quantification has a high degree of uncertainty. In the south of England, for example, typical rainfall is about 700 mm per annum and the evaporation would be expected to be between 500 and 600 mm (Finch and Harding, 1998). An accurate estimate of catchment-scale evaporation is therefore required to accurately assess the recharge of groundwater or the runoff into streams and rivers. Evaporation is, however, one of the most difficult components of the catchment water balance to measure.

Evaporation may also be considered as the latent heat flux ( $L_v E$ ), which is one of the turbulent fluxes contributing to the land surface energy balance, the other being the sensible heat flux ( $H$ ). Measurements of both of these fluxes are required to close the surface energy balance (Stull, 1988):

$$H + L_v E = R_n - G$$

## Eq 1-1

Here  $R_n$  is the net all-wave radiation input, and  $G$  is the ground heat flux. Both  $L_v E$  and  $H$  are responsible for a very large proportion of the land surface energy exchange with the atmosphere (with a much smaller proportion being due to radiative exchange).  $H$  also controls to some extent

the nature of the turbulence (the stability) since it is responsible for buoyancy.  $L_v E$  and  $H$  therefore control the diurnal development of the atmospheric boundary layer, and are key in determining the atmospheric conditions in the surface layer in which humans reside. At larger grid scales (1 - 10 km<sup>2</sup> and greater) these fluxes are important in numerical weather prediction models and other land-surface-atmosphere models including those required to predict climate change. Ultimately, the development of meso-scale and large-scale weather systems, results from the differences in the state variables of temperature, humidity and pressure, caused largely by the movement of heat and moisture by turbulent fluxes.

There are a number of well-established methodologies to measure evaporation directly (for example, the catchment water balance, lysimeters and micrometeorological techniques, see e.g. Verhoef and Campbell (2005)). Micrometeorological techniques, include the Bowen ratio method and eddy covariance (also known as eddy correlation, e.g. Arya, 1988). In particular the eddy covariance (EC) technique has become prevalent, as instrumentation has improved over the last 15 years, and also because the same technique can be used to measure carbon dioxide fluxes (Lee et al., 2004). However such techniques only measure at the small field scale (typically 100-200 m upwind of the measurement mast), since they essentially employ point sensors, and ideally require a uniform upwind fetch. They are also quite complex to operate, with the appropriate data processing requiring many steps, some of which are quite complex (Lee et al., 2004). Such techniques therefore are only feasible within research catchments, with few spatial replicates within these catchments, because of the high equipment cost and the skilled data analysis required. The EC technique also has the limitation that the majority of studies show an inability to close the surface energy

balance, suggesting a systematic underestimate of the turbulent flux measurements typically by 10-20% (Foken, 2008).

The partitioning of energy between  $L_vE$  and  $H$ , however, varies spatially, depending on the vegetation cover, soil type and driving variables ( $R_n$ , wind speed, humidity etc.). This means that only a limited range of land covers within a catchment or grid cell can be sampled, and these may be unrepresentative of the spatial average (Blyth et al., 2006). Even if the major components of the land cover can be sampled (or their fluxes modelled) it is not obvious that they simply aggregate to a large scale mean. Boundaries between the main land cover types, such as hedgerows, isolated trees and small areas of woodland may have an enhanced contribution to the area-averaged evaporation (Herbst et al., 2007). Possible influences on fluxes at these transition zones, may be the horizontal advection of energy from neighbouring areas of different vegetation cover, or the disproportional access to soil-water through deep or horizontally extensive root systems (e.g. Blyth et al., 1995).

Hence there is great scientific interest in the possibility of measuring  $L_vE$  and  $H$  at much larger scales than has been possible with the EC method and other earlier techniques, in order to capture the landscape variability of these fluxes, including the integrated measurement of transition zones. Scintillometry offers just such a prospect: it is a unique ground-based remote sensing technique, providing large scale measurements of  $L_vE$  and  $H$  for areas up to 10 km<sup>2</sup>. Rather than depending on arrays of point sensors, which would have to be deployed *in situ*, a scintillometer is capable of long-path measurements using optical or millimetre-wave electromagnetic radiation

transmitted as a narrow beam, and collected by a receiver, above the measurement area. By remotely sensing the turbulence, the measurement is non-invasive, and does not interfere with land use activity, such as the harvesting of crops – and does not cause flow distortion of the turbulence (which point sensors do). Unlike satellite platforms for remote sensing, the instrumentation is sited below cloud level, allowing continuous operation, except in the case of fog, mist or rain. Aircraft may measure with similar scale, but they are expensive and do not provide the possibility of continuous monitoring. Along with the ability to measure diverse extensive areas, the long-path scintillometer allows a very large spatial volume to be sampled – providing statistically robust data over short temporal averaging periods (a few minutes or less, Kleissl et al., 2008).

The measurement principle of the scintillometer will now be briefly described, before discussing its current limitations, as reported by field trials. The scintillometer fundamentally measures the intensity variations of electromagnetic radiation propagating through the turbulent atmosphere. The phenomenon of scintillation caused by atmospheric turbulence is also observed as the twinkling of stars, or the shimmering heat haze above an extensive warm surface. The intensity variations or scintillations are caused by refractive index changes of the air through which the beam passes, and the measured signal intensity variance can be related to the refractive index structure parameter at the wavelength of propagation, provided that the pathlength is known (Wheelon, 2006). Theory predicts the relationship between the measured refractive index structure parameter and the temperature and humidity structure parameters (Hill et al., 1980). The temperature and humidity structure parameters can be used to calculate  $H$

and  $L_v E$ , by applying Monin-Obukhov Similarity theory (MOST, Hill et al., 1992; Wyngaard et al., 1971).

Using an optical scintillometer, at a near-infrared wavelength, the scintillations are primarily sensitive to the temperature structure parameter, whereas at millimetre wavelengths they are more sensitive to the humidity structure parameter as well as the temperature structure parameter (Andreas, 1989; Wesely, 1976). The optical scintillometer can be used standalone to measure  $H$ , but both types of scintillometer are required to measure  $L_v E$  (Andreas, 1989). The full details of the theory are presented in Chapter 2, and Hill (1992) gives a review of the optical scintillation methods.

Wang et al. (1978) developed the optical Large Aperture Scintillometer (LAS) which operates in the near-infrared, and uses aperture-averaging to increase its resistance to saturation of the optical scintillation signal (which may occur for combinations of long pathlengths, large  $H$ , and for paths that are near to the ground (where scintillation is strongest). One of the first experiments with a LAS measuring time-series fluxes was reported by de Bruin et al. (1995), using a LAS instrument built by Kohsiek (1987). This showed a very good comparison with EC measured  $H$ , over a vineyard, with some variation in topography. McAneney et al. (1995) demonstrated a much longer pathlength (1.7 km) over homogenous terrain for which accurate values of  $H$  were measured with a LAS. de Bruin et al. (1996) conducted an experiment in Crete with a 4.8 km pathlength, again finding mostly good agreement, but with some systematic differences compared to EC.

In applying scintillometry to the measurement of fluxes, the main theoretical constraints come from the assumptions required by MOST. These are that the

surface, over which measurements are made, should be homogeneous, extensive and flat. Clearly, imposing these conditions stringently on the application of scintillometry would greatly limit the use of the technique; in particular it bars the measurement of heterogeneity over complex topography. Hence, research in the last decade has strived to extend the theory – or to demonstrate that it remains valid under certain conditions, even with moderate heterogeneity (Chehbouni et al., 1998; Lagouarde et al., 1996; Lagouarde et al., 2002). Meijninger et al. (2002b) systematically studied this issue, in the Flevoland experiment, demonstrating that over a flat mixed agricultural land landscape in The Netherlands, sensible heat fluxes from the LAS compared well with area-aggregated EC fluxes. The concept of the blending height had been developed – asserting that MOST should remain valid when applied to scintillometer measurements made at sufficient height, where fluxes from separate patches of the landscape are well mixed. In this experiment, with two LASs at different heights, it was found that even just below the blending height there was no serious violation of MOST. Ezzahar et al. (2007) supports and extends this result over mixed vegetation.

Few experiments have been conducted over varying topography, and of these most have been restricted to fairly homogeneous land surfaces (Chehbouni et al., 2000; Hartogensis et al., 2003; Lagouarde et al., 2006; Meijninger and de Bruin, 2000). Beyrich et al. (2002) describes a LAS measurement path near the Meteorological Observatory Lindenberg, Germany, where there is both land surface heterogeneity and gentle topographic variability; here the LITFASS-98 experiment showed reasonable agreement of  $H$  measured by the LAS over a 4.7 km path compared with a weighted average of local measurements. The operation for over ten years of this LAS path, demonstrates the potential and relative ease of long-term monitoring by

scintillometry (Beyrich and Engelbart, 2008). More extensive comparison with EC stations was carried out in the LITFASS-2003 experiment (Beyrich et al., 2006), finding good agreement with the LAS.

Very few microwave (sometimes termed radio-wave) or millimetre-wave scintillometers have been built, due to their high cost and the need for a microwave engineer. Hill et al. (1988) reported a millimetre-wave (173 GHz) experiment to test scintillation theory, with an extensive, flat, homogeneous site that was very well represented by two micrometeorological masts – and combined with an optical scintillometer, both latent and sensible heat fluxes were determined by scintillometry. Sarma and Hill (1988) describe a 94 GHz scintillometer for flux measurement, with the intention that it be combined with optical (LAS) and mid-infrared (10  $\mu\text{m}$  wavelength) scintillometers in order to solve the three unknowns required to calculate the temperature and humidity structure parameters and thus both sensible and latent heat fluxes, without additional assumptions. Otto et al. (1996) applied this methodology at Sevilleta, New Mexico, but appear to have suffered instrumental problems with the 94 GHz scintillometer, as its structure parameter measurements did not agree with those calculated from micrometeorological measurements. Green et al. (2000) and Green et al. (2001) combined a LAS with a 27 GHz scintillometer to measure  $H$  and  $L_v E$ .

The component technology at microwave wavelengths is more mature and therefore lower in cost and more reliable than at millimetre wavelengths; however the scintillation strength is weaker and undesirable water vapour absorption is stronger. The latter was cited as limiting the accuracy of flux measurements by Green et al. (2001). Nieveen et al. (1998) investigated the effect of water vapour absorption on the LAS. Green et al. (2000) showed

some agreement of the LAS – 27 GHz scintillometers' measured  $L_v E$  with measurements by EC, but the agreement broke down at high wind speed near-neutral conditions.

Meijninger et al. (2002a) used the same LAS – 27 GHz scintillometer combination (applying the so called two-wavelength method) to measure  $L_v E$ , which agreed reasonably well with aggregated EC measurements over the flat heterogeneous terrain of the Flevoland experiment. It was again found that  $L_v E$  was over-estimated under near-neutral conditions. The scintillometer-measured fluxes were slightly higher than the aggregated EC measurements; this may have been partly due to the under-closure of the energy balance by EC, or scintillometer mast vibrations, or the aforementioned water vapour absorption.

Lüdi et al. (2005a) described both the theory and practice of an improved method for the measurement of the temperature and humidity structure parameters, using a LAS – 94 GHz scintillometer combination in LITFASS-2003. This 'bichromatic scintillation' technique cross-correlates the high-frequency scintillations of optical and millimetre-wave scintillometers to enable the direct measurement of the temperature-humidity structure parameter, which can only be assumed by the two-wavelength method. The same scintillometer combination was used to measure  $H$  and  $L_v E$  by the two-wavelength method in LITFASS-2003, and Meijninger et al. (2006) reported fairly good agreement with EC measured fluxes, although scintillometer measured  $L_v E$  was about 25% higher. It was noted that this difference corresponded to the difference in energy balance closure of the EC and scintillometer flux systems.

Having briefly surveyed the application of long-range scintillometers to the measurement of area-averaged  $H$  and  $L_v E$ , the goals of this thesis can be presented, viz.:

- ➔ To test the over-arching hypothesis that long-path scintillometry can be applied to measure  $H$  and  $L_v E$  at the landscape scale over complex terrain (i.e. heterogeneous land surface with strongly varying topography).
- ➔ To measure the heterogeneity of sensible heat fluxes over an agricultural landscape at the field scale by eddy covariance, providing a systematic comparison with landscape-scale LAS measurements made over this complex terrain (Chapter 3).
- ➔ To apply a standalone LAS to measure landscape scale  $H$  and to estimate  $L_v E$  using the surface energy balance over complex terrain (Chapter 3).
- ➔ To specify and commission a custom-built millimetre wave scintillometer and apply two-wavelength scintillometry over complex terrain, to directly measure landscape scale  $H$  and  $L_v E$ . (Chapter 5)
- ➔ To analyse some of the current limitations of long-path scintillometry for applications over complex terrain – in particular, the derivation of the effective height for two-wavelength scintillometry (Chapter 4).

- To summarise the current state-of-the-art of long-path scintillometer flux measurement for complex terrain, and to prioritise future work (Chapter 6).

## **Chapter 2 Scintillometry Theory for Sensible and Latent Heat Flux Measurements**

### **2.1 Overview of Theory**

The influence of refractive index changes in the atmosphere on electromagnetic (EM) radiation transmitted through it has been observed and studied for centuries (possibly for millennia but this is less well documented). In the 18th century, Sir Isaac Newton wrote of the twinkling of the stars, as the light emitted from them fluctuates as it propagates through the turbulent atmosphere (Newton, 1730). There appeared to be a determining influence of the motions of the atmosphere and the fluctuations of the observed light travelling through it from the stars (which act as point sources). The theoretical challenge was to link the determining properties of the atmosphere with the observed intensity fluctuations. The theory reveals the atmospheric information that can be retrieved from such observations – providing a theoretical basis for the remote sensing of the atmosphere by scintillometry. Much of the theoretical development was driven not by this goal of probing the atmosphere, but by the needs of engineers for designing microwave and millimetre wave communication links, and for military purposes e.g. Wheelon (2001).

It was in the latter half of the 20th century that wave propagation theory developed to mathematically describe such phenomena. Much of this early work was embodied in Tatarski (1961), which assumed the Kolmogorov turbulence model (described in Section 2.2). A thorough review of methods for remote sensing of many atmospheric variables by optical scintillation is given by Hill (1992); in contrast, the scope of the theory presented here is limited to scintillation methods for the measurement of surface fluxes of sensible heat and water vapour (latent heat). The main emphasis is to provide the theory used elsewhere in this thesis, and importantly to describe the assumptions and restrictions of the validity of those theories.

In the following sections of this chapter, it will be shown that the refractive index structure parameter can be measured by scintillometry. From the measured refractive index structure parameter, with the addition of some meteorological data, the temperature structure parameter can be determined - this is an important measure of the turbulent atmosphere. The scintillometer measures a path-averaged ensemble mean of the refractive index structure parameter, and this will be discussed in some detail.

The theory for two-wavelength scintillometry is described, whereby a second scintillometer, usually operating at millimetre wavelengths (more sensitive to humidity fluctuations), may be combined with the optical scintillometer to measure the humidity structure parameter.

In order to calculate sensible and latent heat fluxes from the measured temperature and humidity structure parameters, boundary layer turbulence theory must be applied. Due to the lack of closure of turbulence theory, the application of similarity theory is particularly useful (grouping variables by

dimensional analysis using Buckingham Pi theory) - Monin and Obukhov first gave the similarity theory for these turbulent surface fluxes (Stull, 1988). The application of this similarity theory is described, allowing the sensible and latent heat fluxes to be calculated from scintillometer measurements.

## **2.2 Turbulence Theory**

Turbulence remains one of the great unsolved problems of classical physics. There are a number of approaches which provide useful mathematical descriptions for certain conditions, but, as yet, the complexity of the problem has not allowed a complete theory to be developed that models the entire phenomenon. There are a large number of equations that are available which characterise turbulence, yet there are more unknowns than equations, and therefore the description of turbulence is not closed (Stull, 1988).

The available tools for describing turbulence fall into two main categories: theory derived by similarity, and empirical equations based on experimental measurements of turbulent flow. The latter usually only apply in particular flow regimes, as will be discussed later, whereas the former are based on dimensional analyses, and thus are often more generally applicable. Full presentations of turbulence theory and its development are given by e.g. Townsend (1980).

Turbulent flow may be thought of as containing eddies of many different length scales, differently oriented in three dimensions, which may or may not be isotropic but are all superimposed on one another. The range of turbulent scales is particularly challenging, often spanning five decades from hundreds

of metres to millimetres. It would therefore require a very high resolution model to attempt to computationally estimate the entire turbulent field which even over a modest volume requires an impracticable number of grid cells. With such chaotic motion, statistical methods are invaluable in quantifying and understanding the random turbulent field. Essential descriptors of turbulent quantities are their means, variances and covariances (the latter two are also referred to as second statistical moments). These succinct statistical variables are sufficient in many problems (e.g. for the calculation of eddy covariance fluxes), whilst in other micrometeorological, civil and aeronautical engineering fields it can also be necessary to have knowledge of the higher order statistical moments. These give a fuller account of the turbulence field in the form of probability distribution functions. For example, it is important to know how the fluctuations of a variable are distributed about its mean value and how the state of the variable at a point in space and time relates to its state at another neighbouring point. One such descriptor is the structure parameter, which is formally described below.

Spectra are another valuable tool in turbulence studies, and are of particular importance in scintillometry; these reveal the turbulent energy distribution with frequency. The spectra show qualitative and quantitative information that is not otherwise readily accessible, and thus proves a powerful analytical technique. Furthermore, statistical variables are sensitive to the methods of calculation, in particular the choice of low frequency detrending method and the associated time-period selected Culf (2000); there is no such ambiguity (bias error) in the calculation of spectra, since de-trending is not required (Panofsky and Dutton, 1984).

Atmospheric turbulence has a range of length and time scales associated with characteristic regimes of behaviour. Conceptually, kinetic energy is introduced into the airflow at the largest scales – called the Production Range – by buoyancy (warmer and/or moister air), wind shear and by turbulent wakes caused by obstacles. In the atmospheric boundary layer wind shear is caused mainly by the frictional drag of rough surfaces, but above the boundary layer it may occur at frontal zones and near the jet stream (clear air turbulence). The large-scale unstable eddies of the Production Range break-up into smaller and smaller eddies over time and space in the turbulent flow. This is the classical cascade of energy from large scales to smaller scales, and in this process the total kinetic energy is conserved – i.e. these intermediate scales are too small for turbulent production to contribute additional energy but too large for viscous dissipation of energy. This is called the Inertial Subrange of the turbulence spectrum. By the simple consideration of the conservation of kinetic energy, such that transfer of energy from high to lower wavenumbers must equal the dissipation rate, it was first shown by Kolmogorov (using dimensional analysis) that as wave-number ( $K$ ) increases, the power spectral density must decrease at a rate proportional to  $K^{-5/3}$  (Stull, 1988). At the smallest turbulent scales, viscous force becomes significant and eddies dissipate as heat – hence this is known as the Dissipation Range.

In the turbulent velocity field two length scales are important in defining different regimes of turbulent behaviour, and allowing simplifying assumptions to be made specifically for these regimes. The first is the *Outer Length Scale* ( $L_0$ ), which marks the eddy scale at which mechanical and buoyant energy production ceases and the transition to the largest scale of the inertial subrange occurs; for applications herein it is related to the measurement

height. The second length scale is the *Inner Length Scale*  $l_0$  and it is the smallest scale of eddies; it also represents the eddy scale at which *inertial* (meaning without gain or loss of kinetic energy) behaviour changes to *viscous energy dissipation*.

Next, it is necessary to introduce some mathematical definitions which allow the derivation of the Kolmogorov turbulence spectrum. Scintillometric measurements depend on the concept of the *structure function* which has been developed in turbulence theory. Kolmogorov uses structure functions in his theory of local isotropy (e.g. Stull, 1988; Townsend, 1980); they provide a means of relating the magnitude of a variable,  $x$ , (only scalars are considered here) to the size ( $r$ ) of the eddies (Tatarski, 1961). If  $x$  is measured at a point  $\underline{r}_1$  in space and another point separated by a small distance  $r$  ( $r \ll z_m$ , where  $z_m$  is the measurement height), then, for *incremental, stationary and isotropic turbulence*, the second order structure function can be written as (Wyngaard et al., 1971)

$$D_{.xx}(r) = \overline{[x(\underline{r}_1) - x(\underline{r}_1 + r)]^2}$$

**Eq 2-1**

$D_{.xx}(r)$  has units of  $x^2$ , the same as variance, and is related to the second order moment, otherwise known as the *covariance function*. A discussion of the simplifying assumptions is given by Monin and Yaglom (1971).

For scalar fluctuations, Obukhov and Corrsin (refer to Wheelon, 2006) presented hypotheses (in parallel to those of Kolmogorov for the locally

isotropic velocity field), in order to derive the following equation, using dimensional arguments, for the inertial subrange (Moene et al., 2004):

$$D_{xx}(r) = a^2 \frac{\overline{N}}{\varepsilon^{1/3}} r^{2/3} \quad l_0 \ll r \ll L_0$$

**Eq 2-2**

Where  $\overline{N}$  is the average scalar fluctuation dissipation (the rate at which the scalar inhomogeneity dissipates per unit time due to molecular diffusion),  $\varepsilon$  is the average energy dissipation and  $a^2$  is a constant with a value of about 3 (the literature suggests a range of 2.8 to 3.2, (Stull, 1988)). By defining the structure function parameter  $C_{x^2}$  for a scalar  $x$  as:

$$C_{x^2} = a^2 \overline{N} \varepsilon^{-1/3}$$

**Eq 2-3**

then,

$$D_{xx}(r) = C_{x^2} r^{2/3}$$

**Eq 2-4**

Of special interest in scintillometry are:  $C_{n^2}$ , the refractive index structure parameter at a particular electromagnetic wavelength;  $C_{T^2}$ , the temperature structure parameter ( $K^2 m^{-2/3}$ ); and  $C_{Q^2}$  the humidity structure parameter ( $g^2 m^{-6} m^{-2/3}$ ). The magnitude of  $C_{x^2}$  is typically very small, in the case of  $C_{n^2}$  it is of the order  $10^{-14}$  to  $10^{-15} m^{-2/3}$  at optical wavelengths.

Kolmogorov hypothesised that the smaller eddies have no memory of the larger scale processes from which they came, so that turbulence becomes statistically homogeneous and locally isotropic at smaller scales (i.e. in the inertial subrange). This leads to the derivation of the three-dimensional Kolmogorov spectrum  $\Phi(K)$ , where  $K$  is the wavenumber ( $K = 2\pi/l$ , with  $l$  the size of the eddy):

$$\Phi_n(K) = 0.033C_{n^2}K^{-11/3}$$

**Eq 2-5**

Note that this differs from the power law of section 2.2, because this is the three-dimensional refractive index spectrum instead of the one-dimensional spectral density given earlier.

The *Large Aperture Scintillometer* (LAS) measures the path-averaged value of  $C_{n^2}$ , with a weighted sensitivity biased towards the middle third of the path length; this path weighting function is discussed later. First it is necessary to describe the theory that relates the scintillometer signal to  $C_{n^2}$  – the interaction of electromagnetic radiation with the turbulent atmosphere that leads to the scintillometer transfer function.

## **2.3 Electromagnetic Wave Propagation in the Turbulent Atmosphere**

The propagation of electromagnetic (EM) radiation of a particular wavelength through the turbulent atmosphere (*a random medium*) is not fully described by

theory: like turbulence, some approximations (with corresponding assumptions) can be made, which lead to theory that is applicable and agrees with experimental results only under certain regimes. The requirement is to have a relationship between the scintillometer output and  $C_{n^2}$ , which involves a detailed model for the propagation of EM waves in a turbulent atmosphere.

The characteristics of the signal measured at a receiver of EM radiation transmitted at a particular wavelength ( $\lambda$ ) can be described mathematically by the application of small angle scattering theory, in the absence of any atmospheric absorption. The receiver, with an aperture diameter  $D_R$ , is separated from the transmitter, with an aperture diameter  $D_T$ , by a distance  $L$ , along an axis  $x$ . For the scintillometer systems presented here,  $D_R = D_T$ , and henceforth a single aperture diameter is referred to as  $D$ . Typically  $L$  is of the order of kilometres. In the ideal case there is no absorption and only *normal scattering* contributes to the variance of the receiver signal; however in practical scintillometers,  $\lambda$  always coincides with some atmospheric molecular absorption lines, as they are so prevalent that they practically cannot be avoided (e.g. those of H<sub>2</sub>O and CO<sub>2</sub>).

An important concept in diffraction theory applied to scintillometry is that of the first *Fresnel Zone*. An optical point source centred at the  $x$  axis and emitting a spherical wavefront along the  $x$  axis produces a diffraction pattern on a screen placed normal to the  $x$  axis. In a perfectly homogeneous medium (without turbulence) the diffraction pattern consists of concentric light and dark rings of constructive and destructive interference. The first Fresnel zone is the diameter ( $F$ ) of the first destructive interference ring in the plane normal to the  $x$  axis, at a specified distance from the source. In scintillometry this

distance is the scintillometer pathlength ( $L$ ), since we are interested in the intensity of the wavefront at the scintillometer receiver. This diffraction theory was developed by Fresnel in 1815, using the Huygens principle that each point on a spherical wavefront acts a new point source of spherical wavefronts (Hecht, 1988; Jenkins and White, 1957). The geometric formula for  $F$  is then:

$$F = \sqrt{\lambda L}$$

**Eq 2-6**

The significance of  $F$  in scintillometry is shown in 2.6.3. The relative size of the scintillometer aperture ( $D$ ) compared with  $F$  gives rise to two distinct classes of scintillometer. Firstly, the Small Aperture Scintillometer (SAS) where:

$$F = \sqrt{\lambda L} \gg D$$

**Eq 2-7**

and secondly the Large Aperture Scintillometer (LAS), where:

$$F = \sqrt{\lambda L} \ll D$$

**Eq 2-8**

Optical diffraction theory is still applied at the much longer wavelength of the MWS (e.g. 3.2 mm), and the first Fresnel zone is very much larger than the aperture diameter, thus the MWS is classed as a SAS.

To mathematically describe the variance of the received signal through the turbulent medium, a description of that turbulence is required – and indeed it is this dependency that makes the scintillometer sensitive to atmospheric

turbulence. The previous section (2.2) gives such a description – the Kolmogorov spectrum, and this is the accepted form assumed for scintillometers operating in the inertial subrange. Thus the combination of the theoretical turbulence spectrum and the theory for EM wave propagation through this turbulence spectrum leads to the theoretical response measured by a scintillometer.

As well as the random turbulent decay at particular frequencies, there are also large-scale mean motions of the whole turbulence spectrum due to the wind speed (Clifford, 1971); this invokes Taylor's frozen turbulence hypothesis – that for short periods of time the turbulent eddies can be considered momentarily constant (not decaying), as they transit through the scintillometer path with the wind component perpendicular to the scintillometer path (the crosswind). The significance of this hypothesis is discussed in relation to spectral analysis in Section 2.6.

It is important to note that both types of scintillometer have spherical wavefronts, since the SAS is a point source, and the LAS may be considered a collection of point sources.

Currently, the most complete solution of the wave equation for use with scintillometers is the Rytov method – the solution is dealt with in detail in: Meijninger (2003), Moene et al. (2004) and Kesteren (2008). This approach includes both diffraction effects and is a perturbation method, like that of Tatarski (1961). Perturbation methods are considered to be superior to the earlier approaches of geometrical optics (where eddies were considered as a series of lenses, and diffractive spreading was ignored). However the Rytov

method still has the shortcoming of requiring perturbations to be small, and therefore is limited to weak turbulence or short path-lengths.

Tatarski (1961) solved Maxwell's wave equation for small angle scattering in a turbulent medium using the Rytov approximation. Whilst the full solution is lengthy and not covered here, it is important for the application of scintillometry to note the fundamental assumptions that were made by Tartarski, in order to provide a solution. Firstly, the usual assumption for the transmitting medium of local isotropy is made – at sufficiently small scales of less than a few metres this may generally be valid, although it is expected to quickly breakdown at larger scales as the vertical and horizontal components are subject to different boundary conditions (Monin and Yaglom, 1971; Stull, 1988). Secondly, the aforementioned small angle scattering may be violated for a particular combination of  $\lambda, L, D$  and scattering strength of the medium. Thirdly, the turbulence is assumed to be statistically independent at a scale greater than the outer length scale ( $L_0$ ), which is accepted as a good assumption.

To permit an analytical solution of the wave equation, the perturbation expansion only includes the first scattering term, resulting in *saturation* effects when compared to experimental observations. Here the term saturation means that  $C_{n^2}$  no longer increases as expected (and may even decrease) with increasing strength of turbulence. The Rytov method utilises a logarithmic transformation of the wave equation, which expresses the amplitude ( $\chi$ ) and phase ( $S'$ ) *fluctuations* in terms of the unperturbed parts ( $A_0$ , and  $S_0$  respectively) and perturbed parts ( $A$ , and  $S$  respectively):

$$\chi = \ln\left(\frac{A}{A_0}\right)$$

**Eq 2-9**

and

$$S' = S - S_0$$

**Eq 2-10**

The unperturbed part is the signal that would be received in free space (a perfect vacuum), whilst the perturbed part is the signal received after scattering through the turbulent atmosphere (Tatarski, 1961), in practice the unperturbed part is taken to be the mean signal, which does slowly vary with atmospheric opacity. The derivation of Tatarski (1961) leads to the following solution of the wave equation, for the variance of  $\chi$  (denoted  $\sigma_\chi^2$ ) for a spherical wave propagating through locally isotropic and statistically homogeneous turbulence (refractivity field):

$$\sigma_\chi^2 = 4\pi^2 \omega^2 \int_0^1 \int_0^\infty K \Phi(K) \sin^2 \left[ \frac{K^2 \gamma L (1 - \gamma)}{2\omega} \right] dK d\gamma$$

**Eq 2-11**

$\omega = 2\pi / \lambda$  is the wavenumber of the propagating EM radiation, and  $\gamma$  is the normalised position along the propagation path. Inserting Eq 2-5 into Eq 2-11 and integrating yields the scintillometer transfer function for a SAS with  $F \gg l_0$  (i.e. applicable to the MWS):

$$\sigma_{\chi}^2 = 0.124 \omega^{7/6} L^{11/6} \langle C_n^2 \rangle \quad l_0 \ll F \ll L_0 \quad \text{and} \quad \sigma_{\chi}^2 < 0.3$$

**Eq 2-12**

Here the  $\langle \rangle$  represents the ensemble mean over the path length. The weak scattering limitation is cited by Meijninger (2003), after Clifford et al. (1974). Note that for the MWS inner scale effects do not contribute to the signal as with  $\lambda = 3$  mm,  $F$  is of the order of metres; however it is necessary to take care that outer scale contributions are minimised – this can be done by increasing the measurement height making  $z_m \gg F$ .

It should also be noted that for an optical wavelength SAS  $F \sim l_0$ , therefore the contribution of the inner scale cannot be ignored, and the refractivity spectrum model must be appropriately extended to that region. The most accepted form of the spectrum in the dissipation range is the Hill spectrum (Hill and Clifford, 1978). Such scintillometers are not used here, so this subject is not discussed further.

### **2.3.1 Aperture Averaging of the Large Aperture Scintillometer**

Eq 2-12 shows the EM wavenumber dependence – at millimetre wavelengths the scintillation signal is much weaker, and therefore is not prone to saturation. However, at optical wavelengths, saturation is a practical consideration for a SAS, limiting its path-length to only a few hundred metres (e.g. Ochs and Clifford, 1972; Ochs et al., 1976). To overcome this restriction on the application of scintillometers at optical wavelengths, a means of reducing scintillation sensitivity was developed by Wang et al. (1978) at the

National Oceanic and Atmospheric Administration's Wave Propagation Laboratory at Boulder, Colorado, U.S.A. Essentially, averaging the received signal over a relatively large aperture makes the scintillometer insensitive to eddy wavenumbers smaller than the aperture diameter ( $D$ ). The LAS reduces the susceptibility to signal saturation, thus allowing much longer propagation paths to be used (up to 5 km). The LAS signal may be analysed as a collection of point sources, whereas the SAS signal is considered a single point source. The LAS reduces the measured fluctuations by averaging over the source and receiver aperture diameters ( $D$ , here only equally sized apertures are considered), so that it is most sensitive to eddies similar in size to  $D$  (this is shown formally in 2.6.3), whilst fluctuations from much smaller eddies tend to cancel as they are averaged across the aperture – this is known as *aperture averaging*. The condition for aperture averaging to reduce the measured fluctuation is that:

$$D > F$$

**Eq 2-13**

Taking account of this aperture averaging, the scintillometer transfer function for the LAS becomes (Wang et al., 1978):

$$\sigma_{\chi}^2 = 0.223 D^{-7} L^3 \langle C_n^2 \rangle \quad l_0 \ll F \ll D \ll L_0$$

**Eq 2-14**

It is assumed in evaluating the integral that:

$$D > 2F = 2\sqrt{\lambda L}$$

**Eq 2-15**

Note that compared with the SAS,  $D$  replaces the wavelength dependence in Eq 2-14. It is also important that the aperture size is sufficiently large to avoid dependence on  $l_0$ , which would require knowledge of the turbulence micro scale to calibrate the LAS. Hill and Ochs (1978) state that the requirement for the calibration to be independent of  $l_0$  is  $D > 30l_0$ . Similarly, Moene et al. (2004) observe that for the LAS calibration to have negligible dependence on the macro scale requires  $L_0 > 10D$ , which for a LAS with  $D = 0.15m$  in turn requires the measurement height to be at least 1.5 m. With these criteria met, then it is accepted that the Kolmogorov spectrum is appropriate to evaluate the above LAS calibration, without introducing significant error. Moreover, it can be verified from high-frequency LAS data that the received fluctuations follow the spectral model employed.

### 2.3.2 Path Weighting Functions

The scintillometer's sensitivity with position along the path is not constant. The ends of the path are fairly insensitive, with the middle third of the path having the highest sensitivity. Rearranging Eq 2-11, we can define the path weighting function  $G(\gamma)$ , by:

$$\sigma_\chi^2 = 0.132\pi^2\omega^2 \int_0^1 C_{n^2}(\gamma)G(\gamma)d\gamma$$

**Eq 2-16**

Where,

$$G(\gamma) = \int_0^{\infty} K^{-8/3} \sin^2 \left[ \frac{K^2 \gamma L (1 - \gamma)}{2\omega} \right] dK$$

**Eq 2-17**

The path weighting function can be conveniently approximated by:

$$G(\gamma) \approx A(\gamma(1-\gamma))^{5/6}, \text{ where } A \text{ is scaling constant.}$$

The normalised path weighting function for a SAS and LAS are shown in Figure 2-1.

For the LAS the aperture averaging effect must also be included in the path weighting function (Hill and Ochs, 1978):

$$G_{LAS}(\gamma) = \int_0^{\infty} K^{-8/3} \sin^2 \left[ \frac{K^2 \gamma L (1 - \gamma)}{2\omega} \right] \times \left[ \left( \frac{2J_1(0.5KD_{LAS}\gamma)}{0.5KD_{LAS}\gamma} \right) \left( \frac{2J_1(0.5KD_{LAS}(1-\gamma))}{0.5KD_{LAS}(1-\gamma)} \right) \right] dK$$

**Eq 2-18**

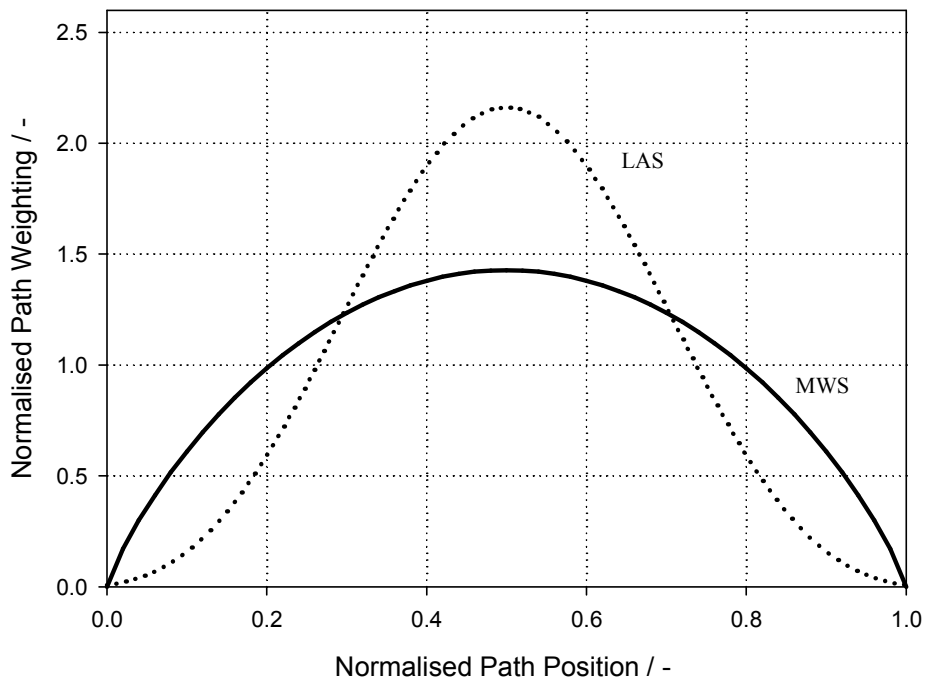


**Figure 2-1 Path weighting functions for the SAS (e.g. MWS) and for the LAS.**

## **2.4 Measuring Structure Parameters by Scintillometry**

A concise summary of the relationships between different structure parameters is given by Meijninger (2003). Firstly, it has been shown that the refractive index structure parameter ( $C_{n^2}$ ) has negligible dependence on pressure (Moene et al., 2004). In the turbulent atmosphere  $C_{n^2}$  depends primarily on temperature fluctuations, and secondarily on humidity fluctuations. The relative contribution of each depends on the wavelength at which  $C_{n^2}$  is measured, although the temperature fluctuations usually dominate, particularly for optical wavelengths.  $C_{n^2}$  is related to  $C_{T^2}$ ,  $C_{Q^2}$  and the temperature-humidity cross structure parameter  $C_{TQ}$  (Hill et al., 1980) by:

$$C_{n^2} = \frac{A_T^2}{\bar{T}^2} C_{T^2} + \frac{2A_T A_Q}{\bar{T} \bar{Q}} C_{TQ} + \frac{A_Q^2}{\bar{Q}^2} C_{Q^2}$$

**Eq 2-19**

$A_T$  and  $A_Q$  are dependent on  $\lambda$ , and are the partial derivatives of the real part of the refractive index with respect to the natural logarithm of the mean air temperature,  $\bar{T}$  in K, and the mean humidity,  $\bar{Q}$  in  $\text{kg m}^{-3}$  (Lawrence and Strohbehn, 1970); for wavelengths between 0.36 and 3  $\mu\text{m}$  they are given by:

$$A_T = -m_1(\lambda) \left( \frac{\bar{P}}{\bar{T}} \right) - R_v m_2(\lambda) \bar{Q}$$

**Eq 2-20**

$$A_Q = R_v m_2(\lambda) \bar{Q}$$

**Eq 2-21**

where  $R_v$  is the specific gas constant for water vapour ( $461.5 \text{ J K}^{-1} \text{ kg}^{-1}$ ). In the near infrared  $m_1 = 0.78 \times 10^{-6} \text{ KPa}^{-1}$  and  $m_2 = -0.126 \times 10^{-6} \text{ KJ}^{-1} \text{ m}^3$ .

The appropriate expressions at millimetre wavelengths ( $\lambda > 3 \text{ mm}$ ) are (Andreas, 1989; Kohsiek and Herben, 1983):

$$A_T = 0.776 \times 10^{-6} \left( \frac{\bar{P}}{\bar{T}} \right) + 1.723 \frac{\bar{Q}}{\bar{T}}$$

**Eq 2-22**

$$A_Q = 1.723 \frac{\bar{Q}}{\bar{T}}$$

**Eq 2-23**

Note that  $A_Q$  is very much smaller than  $A_T$  in the near-infrared but they are of similar magnitude for millimetre waves. Hence in the optical region scintillations are largely due to temperature fluctuations, whereas at millimetre wavelengths both temperature and humidity fluctuations have similar magnitude contributions to  $C_{n^2}$ .

### **2.4.1 The Standalone Near-infrared LAS to Measure $C_T^2$**

The LAS can be deployed as a single scintillometer system to measure  $C_{n^2}$  in the near-infrared. However, Eq 2-19 cannot be solved without further assumptions or approximations, as there are too many unknowns. Moene et

al. (2004) improved the rigour of the derivation first given by Wesley, (1976).

This showed that Eq 2-19 can be written as:

$$C_{n^2} = \frac{A_T^2}{\bar{T}^2} C_{T^2} \left( 1 + r_{TQ} \frac{A_Q \bar{T} C_{Q^2}}{A_T \bar{Q} C_{T^2}} \right)^2$$

#### Eq 2-24

assuming that,

$$r_{TQ} \sqrt{C_{T^2} C_{Q^2}} = C_{TQ}$$

#### Eq 2-25

where  $r_{TQ}$  is the correlation coefficient between temperature and humidity in the inertial subrange. To further simplify Eq 2-24, it has to be assumed that  $r_{TQ} = \pm 1$  (the sign is selected depending on other atmospheric information e.g. stability). It has been shown that the Bowen ratio  $\beta$  can be expressed as (see the derivation given by Moene, 2003):

$$\beta = \frac{H}{L_v E} = \frac{\rho c_p \overline{w'T'}}{L_v \overline{w'Q'}} = \frac{\rho c_p C_{T^2}}{L_v C_{Q^2}}$$

#### Eq 2-26

with  $H$  the sensible heat flux,  $L_v E$  the latent heat flux ( $E$  evaporation in  $\text{kg m}^{-2}\text{s}^{-1}$ ),  $\rho$  the air density (in  $\text{kg m}^{-3}$ ),  $c_p$  the specific heat capacity of air at constant pressure (in  $\text{J kg}^{-1} \text{K}^{-1}$ ) and  $L_v$  the latent heat of vaporisation of water (in  $\text{J kg}^{-1}$ ). Substituting into Eq 2-24 and rearranging gives the working relationship to obtain  $C_{T^2}$  from a single optical scintillometer:

$$C_{T^2} = C_{n^2} \frac{\bar{T}^2}{A_T^2} \left( 1 + r_{TQ} \frac{A_Q \bar{T} \rho c_p}{A_T Q L_v \beta} \right)^{-2}$$

Eq 2-27

## 2.4.2 Two-wavelength Scintillometry

$C_{Q^2}$  may be measured by two-wavelength scintillometry, due to the dependence of  $C_{n^2}$  on temperature as well as humidity fluctuations at all wavelengths, and the assumption of Eq 2-25, since  $C_{TQ}$  is otherwise unknown (Kohsiek and Herben, 1983). Theoretically a third wavelength might be used to remove this assumption (Kohsiek, 1982), but there is no part of the EM spectrum where a third wavelength would give sufficiently different sensitivities, in order that  $C_{TQ}$  can be determined.

Following the sensitivity analysis of Andreas (1989), the optimal combination of near-millimetre and visible to near-infrared wavelengths was suggested for two-wavelength scintillometry. A method for the solution of the pair of simultaneous equations of the form of Eq 2-19, at each measurement wavelength (subscripted 'LAS' and 'MWS') and assuming Eq 2-25, has been provided by Hill et al. (1988):

$$C_{Q^2} = \frac{A_{T\_MWS}^2 C_{n^2\_LAS} + A_{T\_LAS}^2 C_{n^2\_MWS} + 2r_{TQ} A_{T\_MWS} A_{T\_LAS} \sqrt{C_{n^2\_MWS} C_{n^2\_LAS}}}{(\bar{\Gamma T})^2}$$

Eq 2-28

$$C_{T^2} = \frac{A_{Q\_MWS}^2 C_{n^2\_LAS} + A_{Q\_LAS}^2 C_{n^2\_MWS} + 2r_{TQ} A_{Q\_MWS} A_{Q\_LAS} \sqrt{C_{n^2\_MWS} C_{n^2\_LAS}}}{(\Gamma \bar{Q})^2}$$

**Eq 2-29**

where

$$\Gamma = \frac{A_{T\_MWS} A_{Q\_LAS} - A_{T\_LAS} A_{Q\_MWS}}{\bar{TQ}}$$

**Eq 2-30**

### **2.4.3 Two-Wavelength Scintillometry with Bichromatic Covariance**

The two-wavelength method has required the questionable assumption of  $r_{TQ} = \pm 1$ , until more recently when Lüdi et al. (2005a) showed how  $r_{TQ}$  can be measured directly from the *bichromatic covariance* of the intensity fluctuations of the two scintillometers. The method is only slightly more demanding technically due to the requirement for the covariance of the raw scintillometer signals to be calculated at high frequency, and published results for non-homogeneous terrain (Beyrich et al., 2005; Lüdi et al., 2005) show that the scintillometric path-averaged  $r_{TQ}$  is usually about 0.8 for unstable conditions, and agrees well with values determined from eddy covariance data.

Lüdi et al. (2005a) derived the required relationship for the covariance of intensity fluctuations for two extended transmitting apertures, separated by a fixed distance, and observed by two individual receivers, with a second

separation. Hence the cross structure parameter ( $C_{n\_LAS.n\_MWS}$ ) for the two wavelengths can be calculated from the covariance of the intensity fluctuations of the two separate receivers. Lüdi et al. (2005a) also found a unique solution for  $C_{T^2}$ ,  $C_{Q^2}$  and  $C_{TQ}$  from these three measured refractive index structure parameters ( $C_{n^2\_LAS}$ ,  $C_{n^2\_MWS}$ ,  $C_{n\_LAS.n\_MWS}$ ). Thus this bichromatic correlation method is able to directly measure  $C_{TQ}$  and hence also  $r_{TQ}$ .

## **2.5 Sensible and Latent Heat Fluxes from Structure Parameters: the Application of MOST**

MOST (Monin Obukhov Similarity Theory) uses dimensional analysis (Buckingham Pi theory) to form dimensionless groups of turbulence variables which must relate to other such groups through empirical relationships (e.g. Stull, 1988). For the validity of these relationships, it is assumed that the terrain is flat and homogeneous, and that conditions are stationary.

MOST relates  $C_{T^2}$  and  $C_{Q^2}$ , at height  $z$ , to  $H$  and  $L_v E$ , respectively, through Wyngaard et al. (1971):

$$C_{X^2} \left( \frac{z^{1/3}}{X_*} \right)^2 = c_{X1} \left( 1 - \frac{c_{X2} z}{L_{Ob}} \right)^{-2/3} \quad L_{Ob} < 0$$

**Eq 2-31**

where  $C_{X^2}$  is the structure parameter,  $c_{X1}$  and  $c_{X2}$  are constants (the subscript  $X$  denoting either temperature or humidity),  $X_*$  is the surface layer temperature or humidity scale, and  $L_{Ob}$  is the Obukhov length:

$$L_{Ob} = \frac{u_*^2 T}{g k_v T_*}$$

**Eq 2-32**

Here,  $u_*$  is the friction velocity,  $g$  is the acceleration due to gravity,  $T$  is air temperature,  $k_v$  is the von Kármán constant, and the temperature scale  $T_*$  is given by:

$$T_* = \frac{-H}{\rho c_p u_*}$$

**Eq 2-33**

where  $\rho$  denotes air density and  $c_p$  the specific heat of air at constant pressure.

In a manner similar to Tillman (1972), the following form is obtained:

$$\frac{H}{\rho c_p} = \left[ \left( \frac{C_T^2 z^{\frac{2}{3}}}{c_{T1}} \right)^{\frac{3}{2}} \frac{k_v g z}{T} \left( \frac{1 - c_{T2} \frac{z}{L_{Ob}}}{\frac{-z}{L_{Ob}}} \right) \right]^{\frac{1}{2}} \quad L_{Ob} < 0$$

**Eq 2-34**

Assuming that fluctuations of temperature and humidity are perfectly correlated, then, similarly to de Bruin et al. (1993), the evaporation ( $E = \rho q_* u_*$ ) can be written as:

$$E = \left( \frac{C_Q^2 z^{\frac{2}{3}}}{c_{T1}^3} \right)^{\frac{1}{2}} \left[ \left( C_T^2 z^{\frac{2}{3}} \right)^{\frac{1}{2}} \frac{k_v g z}{T} \left( \frac{1 - c_{T2} \frac{z}{L_{Ob}}}{\frac{-z}{L_{Ob}}} \right) \right]^{\frac{1}{2}} \quad L_{Ob} < 0$$

**Eq 2-35**

Note that even if it were possible to measure  $C_{Q^2}$  by scintillometry without measuring  $C_{T^2}$ , the latter is in any case required to calculate  $L_v E$  as it provides the buoyancy term.

In the derivations of Eq 2-34 and Eq 2-35 a  $C_{T^2}$ -flux (and  $C_{Q^2}$ -flux) MOST-relationship must be assumed, and herein the version proposed by de Bruin et al. (1993) is adopted, which is a revised version of the expression proposed earlier by Wyngaard et al. (1971). Note that the latter authors used a von Karman constant of 0.34, whereas here a value of 0.4 is used (de Bruin et al., 1993; Hill, 1992). de Bruin et al. (1993) empirically found that  $c_{T1} = 4.9$  and  $c_{T2} = 9$  for the stability function describing the  $C_{T^2}$ -flux MOST relationship for unstable conditions, which is written in the form:

$$f\left(\frac{z-d}{L_{Ob}}\right) = c_{T1} \left(1 - c_{T2} \frac{z-d}{L_{Ob}}\right)^{\frac{-2}{3}}, \quad \text{for} \quad \left(\frac{z-d}{L_{Ob}}\right) < 0$$

**Eq 2-36**

with  $d$  the zero-plane displacement height. There remains uncertainty as to the most appropriate values for these constants, thus there remains a choice of which  $C_{T^2}$ -flux MOST relationship to apply, which can have a significant impact on the calculated flux (of the order of 10 to 15 %). The de Bruin et al. (1993) function was fitted to the La Crau dataset and was selected here because the measurement conditions herein (refer to later experimental chapters) were more similar to those of La Crau than those of the Kansas dataset, as there are local inhomogeneities. Moreover, the relatively neutral conditions reported at La Crau occur in the datasets presented here, requiring that the  $C_{T^2}$ -flux MOST relationship extends to high values of  $-\left(\frac{z-d}{L_{Ob}}\right)$ , which are absent from the Kansas dataset as presented by Wyngaard et al. (1971).

In the equations presented above,  $H$  is derived by iteration.  $u_*$  can be estimated from the mean wind speed ( $u$ ) measured at height  $z_u$  and a value for the roughness length for momentum ( $z_0$ ):

$$u_* = \frac{k_v u}{\ln\left(\frac{z_u - d}{z_0}\right) - \Psi_m\left(\frac{z_u - d}{L_{Ob}}\right) + \Psi_m\left(\frac{z_0}{L_{Ob}}\right)}$$

**Eq 2-37**

Here  $\Psi_m$  is the integrated Businger-Dyer relationship (Panofsky and Dutton, 1984):

$$\Psi_m\left(\frac{z}{L_{Ob}}\right) = \ln\left[\left(\frac{1+x^2}{2}\right)\left(\frac{1+x}{2}\right)^2\right] - 2\arctan(x) + \frac{\pi}{2} \quad \left(\frac{z-d}{L_{Ob}}\right) < 0$$

**Eq 2-38**

with  $x = \left(1 + 16\left|\frac{z-d}{L_{Ob}}\right|\right)^{1/4}$ .

## **2.6 Theoretical Turbulence Spectra Measured by Scintillometers**

### **2.6.1 The Theoretical Spectrum of the MWS**

The MWS measures the rapidly varying signal amplitude of the transmitted wave detected at the receiver (instrumental details are described later). The fluctuations are caused by changes in the scattering of the wavefront as large-scale inhomogeneities of the turbulent air move through the illuminated volume, with the prevailing wind, and, to a lesser extent, the intrinsic dynamics of the turbulence itself, due to the decay of turbulence, cascading down the length scale and turbulent mixing. The time-series of this signal is a random fluctuation about a mean value and is not particularly useful analytically; however, there are two analysis techniques that reveal the characteristic behaviour of these signals by representing them in the frequency domain – they are the autocorrelation function and the power spectrum.

The assumption of Taylor's hypothesis has already been mentioned – here it is emphasised with respect to frequency analysis. It is postulated that (a) the observed turbulence is entirely frozen for the time taken for it to transect the

illuminated measurement volume; and (b) that the wind speed is both constant in time, with no variable component, and constant along the path-length – such that the air moving through the illuminated volume is transported with constant velocity and without deformation.

When these assumptions are valid, there is an equivalence of spatially and temporally separated observations. This is particularly advantageous for the single detector systems presented here, which do not otherwise directly provide spatial information. A single detector measures the time series of log amplitude fluctuations  $\chi(t)$  for a propagation path along the  $x$  axis. Exactly the same time series is observed at a later time  $(t + \tau)$  at a position separated by  $r = v\tau$ , with both  $r$  and  $v$  (the crosswind speed) normal to  $x$ . Hence, the amplitude temporal covariance is related to the spatial covariance by (Wheelon, 2006):

$$\langle \chi(r, t) \chi(r, t + \tau) \rangle = \langle \chi(r, t) \chi(r + v\tau, t) \rangle \quad 2-39$$

Here the  $\langle \rangle$  represents the ensemble mean.

Using the Wiener-Khinchine theorem, the random amplitude time series is transformed into its power spectrum  $W_\chi(\omega)$ :

$$W_\chi(\omega) = \int_{-\infty}^{\infty} e^{i\omega\tau} \langle \chi(t) \chi(t + \tau) \rangle d\tau$$

**Eq 2-40**

$\omega = 2\pi / \lambda$  is the wavenumber of the propagating electromagnetic radiation. The Fourier transform is shown above in its symmetrical form, most

convenient for the application of the Fast Fourier Transform (FFT), whereas most of the literature in this field show the asymmetric form (Wheelon, 2006):

$$W_{\chi}(\omega) = \int_0^{\infty} \cos(\omega\tau) \langle \chi(t)\chi(t+\tau) \rangle d\tau$$

**Eq 2-41**

For consistency with the literature, the asymmetric form is adopted here.

The power spectrum and temporal covariance provide equivalent information and both can be calculated from the times series  $\chi(t)$ .

Next, in order to numerically compute the theoretical spectra, a theoretical form of the covariance is required (Clifford, 1971):

$$\langle \chi_R(t)\chi_R(t+\tau) \rangle = 2\pi^2\omega^2 \int_0^L \int_0^{\infty} K\Phi_n(K)J_0(K, \nu, \tau) \sin^2 \left[ \frac{K^2x(L-x)}{2\omega L} \right] dKdx$$

**Eq 2-42**

Here the subscript  $_R$  has been introduced to identify the real part of the covariance function that describes normal scattering (that is without any absorption).

Substituting the covariance function and integrating leads to the real part of the power spectrum  $W_{\chi R}(f)$  of the spherical wave log amplitude ( $\chi$ ), as a function of temporal-frequency ( $f$ ), and is given by Clifford (1971), following the work of Tatarski (1961) and Lawrence and Strohbehn (1970):

$$W_{\chi R}(f) = 16\pi^2 \omega^2 \int_0^L \int_{\frac{2\pi f}{v}}^{\infty} K \Phi_n(K) \frac{1}{\sqrt{(Kv)^2 - (2\pi f)^2}} \sin^2 \left[ \frac{K^2 x(L-x)}{2\omega L} \right] dK dx$$

**Eq 2-43**

where  $(K)$  is the *two-dimensional* spatial wavenumber, in the plane normal to  $x$  (since we are integrating over  $x$ ). The refractivity spectrum  $(\Phi_n(K))$  follows the turbulence spectrum discussed in the last section, and for the inertial subrange of turbulence it is assumed that the Kolmogorov refractivity spectrum is valid. Thus, substituting this spectrum (Eq 2-5) into Eq 2-43, gives:

$$W_{\chi R}(f) = 0.528\pi^2 \omega^2 C_{n^2 R}^2 \int_0^L \int_{\frac{2\pi f}{v}}^{\infty} K^{-8/3} \frac{1}{\sqrt{(Kv)^2 - (2\pi f)^2}} \sin^2 \left[ \frac{K^2 x(L-x)}{2\omega L} \right] dK dx$$

**Eq 2-44**

Here  $C_{n^2 R}$  denotes the real part of the refractive index structure function. A similar expression is found Clifford (1971) for the spherical-wave phase or absorption spectra, which relates to the imaginary part of the refractive index  $C_{n^2 I}$ :

$$W_{\chi I}(f) = 0.528\pi^2 \omega^2 C_{n^2 I}^2 \int_0^L \int_{\frac{2\pi f}{v}}^{\infty} K^{-8/3} \frac{1}{\sqrt{(Kv)^2 - (2\pi f)^2}} \cos^2 \left[ \frac{K^2 x(L-x)}{2\omega L} \right] dK dx$$

**Eq 2-45**

The resultant modulus,  $W_{\chi}(f)$ , is given by:

$$W_z(f) = \sqrt{W_{zR}^2(f) + W_{zI}^2(f)}$$

**Eq 2-46**

The amplitude variance measured by a scintillometer is the modulus of the real and imaginary parts i.e.  $W_z(f)$ .

The above integrals are readily calculated. Specialised software such as Mathcad (Parametric Technology Corporation, MA, USA) is particularly expedient and informative in allowing exploration of the functions. Parameter values for these calculations were taken for the Sheepdrove Organic Farm MWS setup. There is uncertainty in the magnitude of the absorption contribution  $C_{n^2I}$  as it requires the measurement of the phase fluctuation which is seldom done for these applications – no values were found in the literature for the 94 GHz frequency of the MWS. Therefore the typical value measured by Lüdi et al. (2005b) at 212 GHz was used for the calculation of the MWS absorption spectrum – due to increased absorption at this higher frequency, it is expected that this will over-estimate the contribution of absorption fluctuations at 94 GHz. These power spectral densities are plotted in Figure 2-2 on a log-log scale to show the power-law decay.  $W_{zR}(f)$  has a frequency-independent plateau at low frequency with a distinct corner at frequency  $f_c$ . The whole spectrum scales with  $C_{n^2R}$ . The inertial subrange is evident, with its characteristic  $^{-8/3}$  power-law decay with frequency. At the dissipation range the Hill bump (Hill and Clifford, 1978) is included for completeness, though it is not discussed further here, since herein inner-scale scintillometers are not utilised. The corner  $f_c$  is related to the crosswind speed – it is the highest frequency at which large-scale inhomogeneities are

carried through the illuminated volume. Beyond the corner, the inertial subrange is revealed – at these higher frequencies amplitude variance is due to the frozen cascade of length scales, which produces a continually evolving pattern of intensity at the receiver (Lawrence et al., 1972). Note that the inertial subrange often does extend to lower frequencies but the power-law behaviour becomes hidden by the large scale changes, which dominate the spectral intensity at frequencies below the crosswind corner. Figure 2-3 illustrates this behaviour by showing spectra for several different crosswind speeds. Several analysis methods are available for determining the crosswind speed and its variance from scintillometers, based on this dependence of spectra on crosswind speed (Lawrence et al., 1972; Poggio et al., 2000; Wang et al., 1981).

The example absorption spectrum shown ( $W_{z'}(f)$ ) shows that absorption is only important at very low frequencies – again its spectrum is dependent on the crosswind speed. Absorption changes tend to average linearly, with a wide range of phases, so that effectively there is no constructive interference, thus rapid temporal changes always get averaged out along the path. The remaining dominant frequency contribution is the large-scale inhomogeneities, and the crosswind speed controls the frequency at which these are observed. However, there is no low frequency plateau (or frequency independent part of the absorption spectrum); instead, inertial subrange decay is evident at even the lowest frequencies.

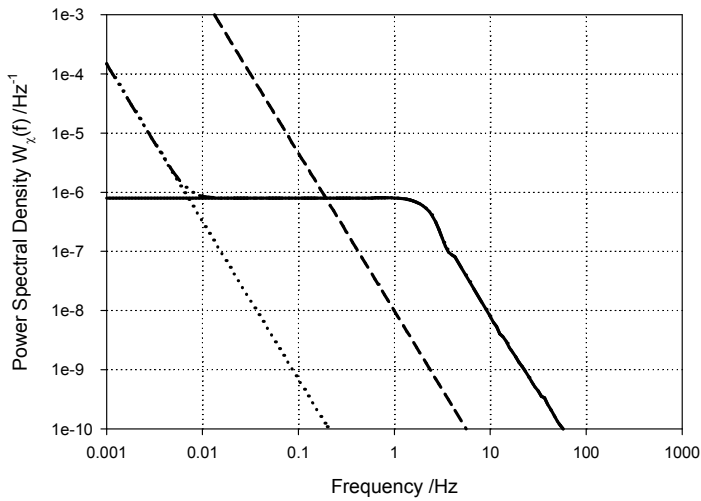


Figure 2-2 Calculated theoretical temporal power spectral density of the MWS: solid line is the refraction contribution (without absorption); the dotted line is the absorption contribution; the dot-dash line shows the resultant of absorption and refraction (where this deviates from the solid line below 0.01 Hz); the dashed line is a reference line of slope  $-8/3$ ; crosswind speed =  $5 \text{ m s}^{-1}$ , pathlength =  $2.43 \text{ km}$ ,  $C_{n^2R} = 5 \times 10^{-14} \text{ m}^{-2/3}$ ,

$$\text{and } C_{n^2I} = 1 \times 10^{-20} \text{ m}^{-2/3}.$$

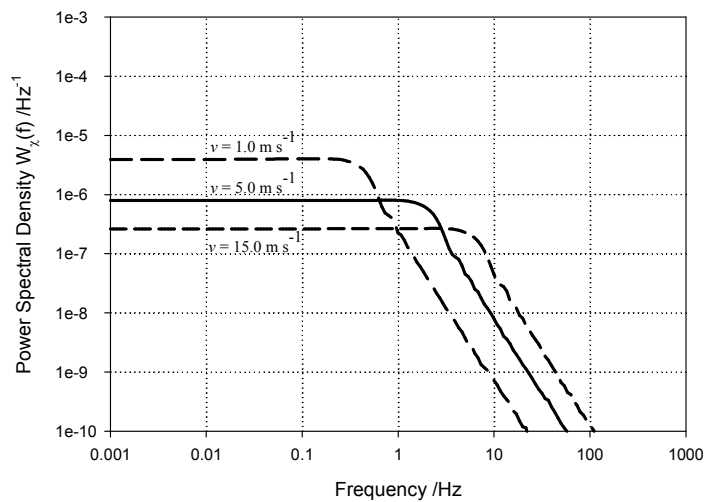
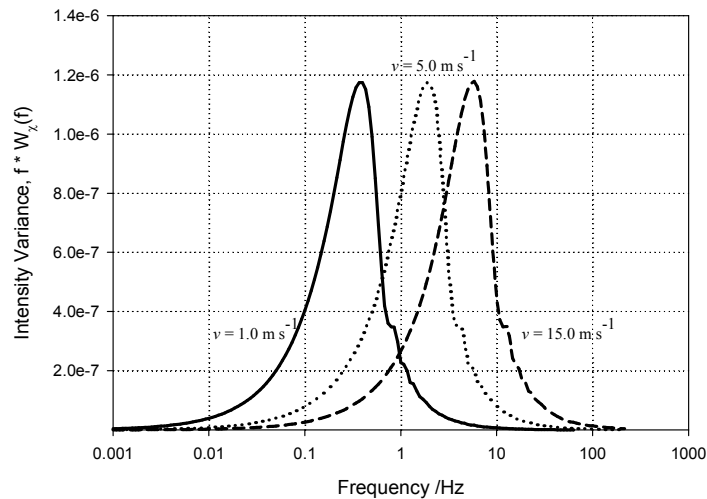


Figure 2-3 Calculated theoretical temporal power spectral density of the MWS for different crosswind speeds, without absorption. (Pathlength =  $2.43 \text{ km}$ ,  $C_{n^2R} = 5 \times 10^{-14} \text{ m}^{-2/3}$ ).



**Figure 2-4** Calculated theoretical intensity variance spectra of the MWS for different crosswind speeds, without absorption. (Pathlength = 2.43 km,  $C_{n^2R} = 5 \times 10^{-14} \text{ m}^{-2/3}$ ).

The scintillometer measures the integrated signal variance over time, and by plotting with semi-log axes, the area under the  $f \times W_x(f)$  curve is equal to the total variance in a time averaging period,  $\tau > f_{\min}$ , where  $f_{\min}$  is the lowest frequency of significant contribution (Figure 2-4). The plots show the frequency spectrum, which shows a pronounced peak at the predominant frequency in the spectrum ( $f_c$ ), this is directly related to the crosswind speed.

In practice  $f_{\min}$  is usually set by bandpass filtering the detected raw signal. Note that at low wind speeds  $f_{\min}$  may become very low indeed e.g. 0.01 Hz for a crosswind of  $1.0 \text{ m s}^{-1}$  (Figure 2-4), and by reference to Figure 2-2 it may become difficult, if not impossible, to separate spectrally (i.e. by bandpass filtering) the refractive scintillations from the absorption scintillations. Without an additional measurement of the absorption contribution, or some other means of discriminating between the refraction and absorption scintillations, the contamination of the signal variance at very low wind speeds becomes a

fundamental limitation of the method. Moreover this limitation has not been recognised or at least not stated clearly in the literature – probably because of the lack of data for the magnitude of  $C_{n^2_I}$  and therefore the difficulty in estimating the absorption contribution. The relative contribution of absorption must be considered, since in the wintertime  $C_{n^2_R}$  may be much smaller, without necessarily such a large decrease in  $C_{n^2_I}$ . Finally, the refractive index scintillations are enhanced more by long paths than are absorption scintillations, so the limitation, if any, of absorption is lessened with longer paths.

## 2.6.2 The Theoretical Spectrum of the LAS

The LAS aperture-averages at both the transmitter and receiver (in contrast to the MWS, which does not aperture-average because it is a SAS, as previously discussed). Following the work of Clifford (1971) described in 2.6.1, the expressions for the theoretical spectra of the MWS have been extended to the LAS by Nieveen et al. (1998), by including the effect of aperture averaging. Thus Eq 2-44 and Eq 2-45 become:

$$W_{zR\_LAS}(f) = 0.528\pi^2 \omega_{LAS}^2 C_{n^2R\_LAS} \int_0^L \int_{\frac{2\pi f}{v}}^{\infty} K^{-8/3} \frac{1}{\sqrt{(Kv)^2 - (2\pi f)^2}} \sin^2 \left[ \frac{K^2 x(L-x)}{2\omega_{LAS}L} \right] \\ \times \left[ \left( \frac{2J_1(0.5KD_{LAS} \frac{x}{L})}{0.5\kappa D_{LAS} \frac{x}{L}} \right) \left( \frac{2J_1(0.5\kappa D_{LAS} \frac{(L-x)}{L})}{0.5\kappa D_{LAS} \frac{(L-x)}{L}} \right) \right] dK dx$$

Eq 2-47

$$W_{\chi I\_LAS}(f) = 0.528\pi^2 \omega_{LAS}^2 C_{n^2 I\_LAS} \int_0^L \int_{\frac{2\pi f}{v}}^{\infty} K^{-8/3} \frac{1}{\sqrt{(Kv)^2 - (2\pi f)^2}} \cos^2 \left[ \frac{K^2 x(L-x)}{2\omega_{LAS}L} \right] \\ \times \left[ \left( \frac{2J_1(0.5KD_{LAS} \frac{x}{L})}{0.5\kappa D_{LAS} \frac{x}{L}} \right) \left( \frac{2J_1(0.5\kappa D_{LAS} \frac{(L-x)}{L})}{0.5\kappa D_{LAS} \frac{(L-x)}{L}} \right) \right] dK dx$$

**Eq 2-48**

These power spectral densities for the LAS were computed for the Sheepdrove Organic Farm scintillometer path, using the  $C_{n^2 I\_LAS}$  value estimated by Nieveen et al. (1998) – this is *not* applicable to the Kipp & Zonen LAS150 used herein since the wavelength is considerably different (880 nm instead of the 945 nm used to estimate  $C_{n^2 I\_LAS}$ ). However the application of the theory is the demonstrated here, even if the magnitude differs somewhat. Nieveen et al. (1998) used an optical filter to select a spectral region of the LED with the strongest water vapour absorption within the LED spectral envelope; thus for a more typical (wider) LED wavelength envelope, the absorption effect is expected to be weaker. Ideally the strength of water vapour absorption should be verified or estimated for the LAS150.

The resulting spectra are shown in Figure 2-5. The characteristics are broadly similar to the spectra for the MWS, except that the total absorption is stronger (with the above noted uncertainty), and therefore only noticeably contributes to  $W_{\chi}(f)$  at very low frequencies ( $<10^{-1}$  Hz). As will be discussed later, this absorption does not actually contribute to the measured output of the LAS because it is rejected by the bandpass filtering of the raw intensity signal.

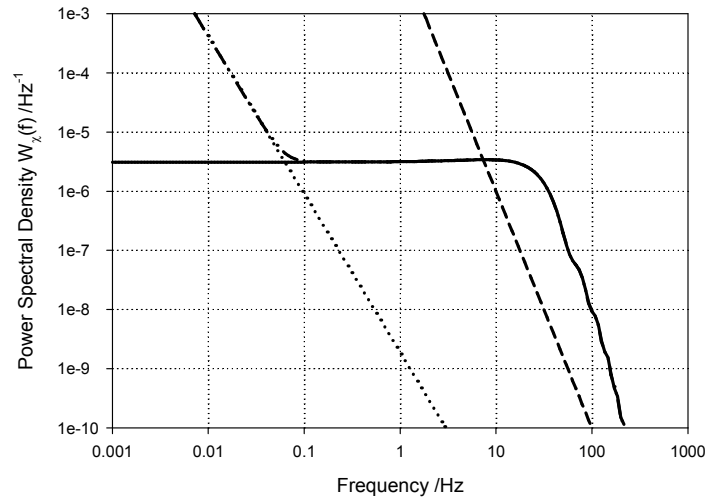


**Figure 2-5** Calculated theoretical temporal power spectral density of the LAS: solid line is the refraction contribution; the dotted line is the absorption contribution; the dot-dash line is absorption and refraction (where this deviates from the solid line below 0.1 Hz); the dashed reference line has slope = -12/3; crosswind speed = 5 m s<sup>-1</sup>, pathlength

$$= 2.43 \text{ km}, C_{n^2R\_LAS} = 1 \times 10^{-14} \text{ m}^{-2/3}, \text{ and } C_{n^2I\_LAS} = 1 \times 10^{-24} \text{ m}^{-2/3}.$$

It is clear that the whole spectrum is shifted to higher frequencies and the decay is steeper, compared with that of the MWS. The shift to higher frequencies is due to the much shorter wavelength of the infra-red light, making the LAS more sensitive to higher wavenumbers (and equivalently higher frequencies). The steeper power law decay with frequency of -12/3 is due to the damping effect of the apertures combined with the Kolomogorov roll-off (Kesteren, 2008; Nieveen et al., 1998). The issue of scintillometer sensitivity to different eddy sizes is not immediately obvious but it is important to take into account. It is dealt with in Section 2.6.3.

### 2.6.3 Sensitivity of Scintillometers to Eddy Size

A valuable technique to investigate the spectral behaviour of a scintillometer with respect to eddy wavenumber (as distinct to the temporal frequency spectra of the preceding sections) is to evaluate the integrand contained in the equation for the log amplitude variance (i.e. Eq 2-43) for a certain set of fixed conditions. Such an analysis has been presented by several authors (e.g. Kesteren, 2008; Meijninger, 2003). The latter is particularly useful here as the same models of scintillometers (the LAS 150 and the MWS) were used, as well as for the depth of analysis. However, this type of work has not before included absorption effects – this new analysis is presented here for the first time. The analysis of the integrand with wavenumber enables insight into the variance contributed to the total signal from a particular wavenumber, under the specified fixed conditions. Without this analysis the wavenumber dependent information is lost in the total sum of the integral – or is at best hard to visualise from the mathematical representation alone. The integrand is straight-forward to evaluate and therefore it is not very time-consuming to compute for many different conditions of interest.

Results for this theoretical analysis for the MWS and LAS, are presented in Figure 2-6, and Figure 2-7 respectively. These show the normalised integrands for the real part, evaluated at the path midpoint and at  $\gamma = 0.25$ , and the imaginary part evaluated at just the midpoint.

It is of particular importance, for the studies presented here, to note that for both the LAS and the MWS, the wavenumber sensitivity depends on the

position along the path – that is particular positions ( $\gamma$ ) along the path are biased to different wavenumber ranges. Furthermore, these wavenumber ranges are not coincident for the LAS and the MWS. The path weighting function is also evident, with diminishing total contributions to the variance as  $\gamma$  moves away from the centre of the path. The contribution of smaller eddies to the signal is less, but the effect of the Kolmogorov spectrum has been included, which in any case leads to lower spectral intensity at higher wavenumbers.

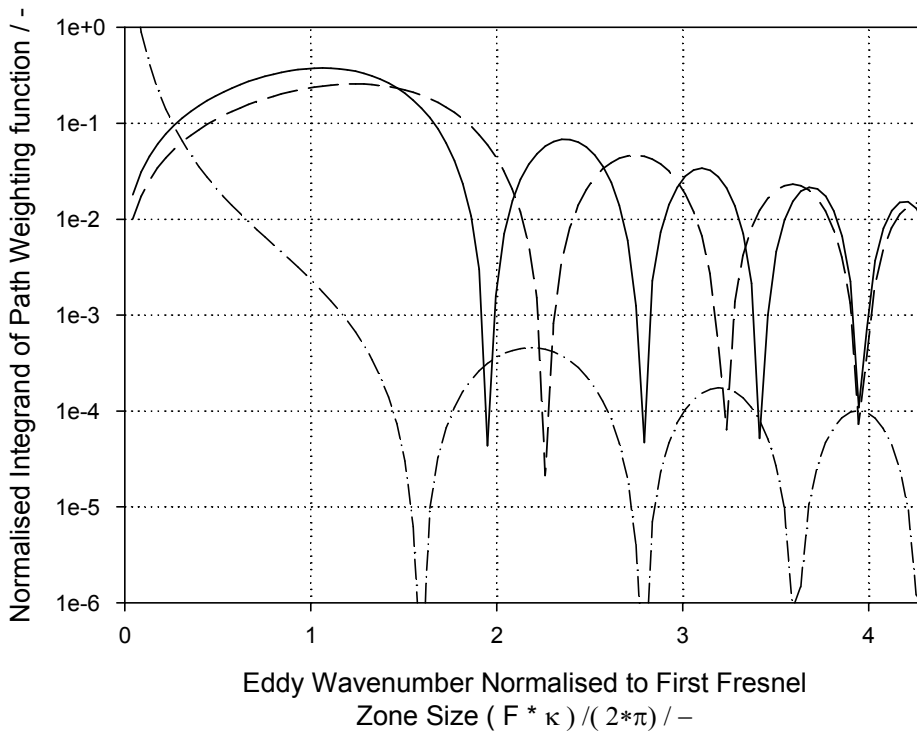


**Figure 2-6 Normalised integrand of the path weighting function for the MWS, evaluated at centre of path ( $\gamma = 0.5$ , solid line) and  $\gamma = 0.25$  (dashed line), both normalised with total integral for  $\gamma = 0.5$ . The dash-dot line shows the absorption contribution ( $\gamma = 0.5$ ), normalised with its integral – Note this does *not* indicate the relative magnitude of absorption with respect to refraction scintillations, only the wavenumber dependence of each.**

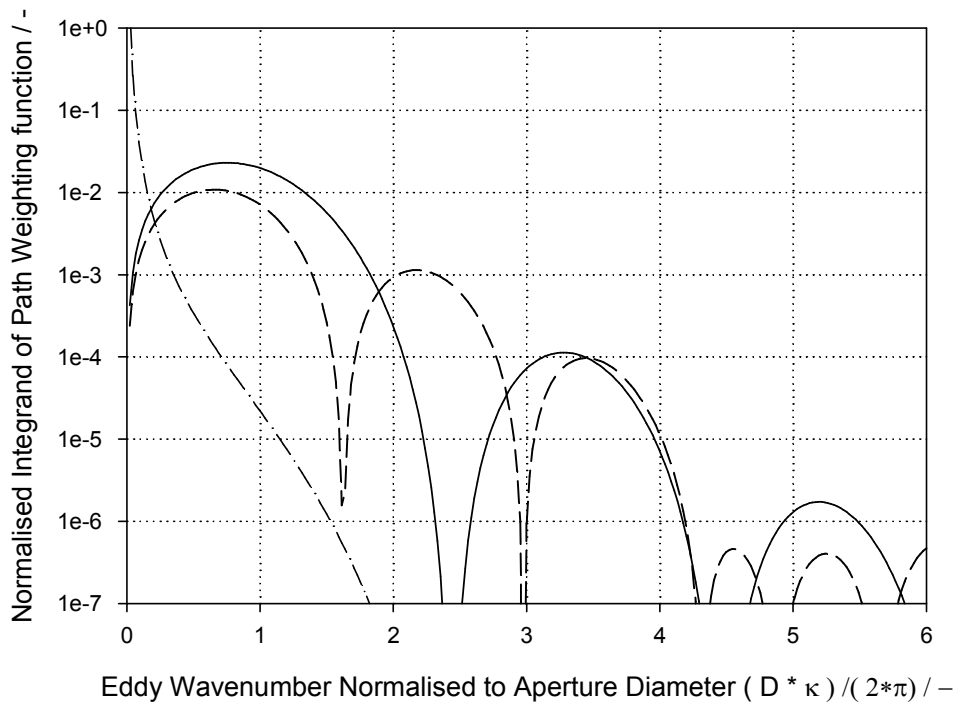


**Figure 2-7 Normalised integrand of the path weighting function for the LAS, evaluated at centre of path ( $\gamma = 0.5$ , solid line) and  $\gamma = 0.25$  (dashed line), both normalised with total integral for  $\gamma = 0.5$ . The dash-dot line shows the absorption contribution ( $\gamma = 0.5$ ), normalised with its integral – Note this does *not* indicate the relative magnitude of absorption with respect to refraction scintillations, only the wavenumber dependence of each.**

# **Chapter 3    Evaporation and Sensible Heat Fluxes Measured with a Large Aperture Scintillometer Over Undulating, Mixed Agricultural Terrain**

## **3.1 Introduction**

Good quality evaporation data – both accurate and representative of large catchments – are critical in assessing the recharge of the chalk aquifers. Recharge may be only a small difference between precipitation and evaporation plus runoff – making hydrological models quite sensitive to errors in the estimated evaporation. Hydrological models use either potential (or reference crop) evaporation or large-area mean estimates like MORECS (Field, 1983) in assessing catchment water balances. However, both fail to account for variation in crop evaporation as soil moisture or leaf area changes reduce evaporation below the potential rate. This creates a need for measurements over different crop types which can be used for validating models of evaporation which include better plant function representation and phenology.

Land surface and catchment models as well as satellite estimates usually operate at large grid scales (at least 2 km<sup>2</sup>). To validate these models requires evaporation measurements which are representative at that scale. Such measurements must average land surface variability, accounting for the wide range and mixture of vegetation types that are typically found in an agricultural landscape (Blyth et al., 2006). Plot scale methods are problematic to apply across the landscape scale, as they require many replications across the different land-surface types. For example, eddy covariance (EC) stations provide representative measurements of homogeneous vegetation that is well-suited to the field scale, but additional EC stations are then required for each field type, to obtain large area-average estimates. These stations are both expensive and relatively demanding in terms of technical expertise and maintenance requirements. A number of experiments (Mauder et al., 2006; Oncley et al., 2007) have reported the shortcomings of the EC method, which often result in a lack of surface energy balance closure. These studies show that great attention must be paid to the selection and the appropriate operation of accurate instrumentation. Additionally, the different application of post-processing algorithms and software can have a large impact on flux uncertainties (Mauder and Foken, 2006; Mauder et al., 2008). Although similar uncertainties are also encountered in the determination of fluxes by scintillometry, it offers an established technique to average turbulent heat fluxes along an extensive measurement line of 1 to 10 km, with flux source areas comparable to model and satellite grids (Beyrich et al., 2002).

There are few published measurements comparing evaporation from different crops made in the same geographical region at the same time, when meteorological and soil conditions are similar (one of the most extensive campaigns was LITFASS-2003, (Beyrich et al., 2006)). The largest contrast in

evaporation rates is expected to occur in the summer growing season, when there is high solar radiation supplying energy for evaporation, and when some crops are beginning to senesce. This provides useful value ranges for model validation. Gash et al. (1997) showed the dependence of evaporation on vegetation type as well as the importance of surface soil moisture conditions. It has only been with the application of scintillometers over the last 20 years that large area measurements have been made. For the measurement of evaporation, Andreas (1989) showed that a combination of millimetre-wave and optical scintillometers is optimal for direct measurement of both  $H$  and  $L_v E$  (this is termed the two-wavelength method). Limited studies (i.e. Green et al., 2000; Green et al., 2001; Meijninger et al., 2002; Meijninger et al., 2006), using the two-wavelength method, show reasonable results, but it is an expensive technique, not commercially available, and few, if any, studies have established its reliability for continuous monitoring.

A simpler, commercially available, and cheaper method is the near-infrared Large Aperture Scintillometer (LAS), which measures  $H$  directly and  $L_v E$  via the surface energy balance. Meijninger et al. (2002b) showed that this approach can provide useful large area evaporation measurements, even over moderately heterogeneous terrain (mixed crops, with flat topography).

Schuttemeyer et al. (2006) successfully used the same approach in Ghana over patchy sparse Sahelian savannah, which was relatively homogeneous at the 100 m scale. Moreover, the LITFASS-2003 experiment (Meijninger et al., 2006) demonstrated the applicability of scintillometry over a 4.7 km long path of mixed crops, grassland, lake and forest, with moderate topography. In these experiments it was considered preferable to operate above the so-called 'blending height', where different fluxes from distinctly characterised

land cover areas within the scintillometer source area are considered to be well mixed, which allows Monin-Obukhov Similarity Theory (MOST) to be applied (this is necessary to calculate fluxes from scintillometer measurements).

The study presented here, part of the UK LOwland CAatchment Research programme (LOCAR), extends scintillometry to the complex undulating terrain of chalk downland that has the steeply varying topography with mixed vegetation types that is typical of many parts of southern England. These are the first experimental results comparing the LAS-derived  $L_vE$  with EC measurements over such complex terrain.  $L_vE$  and  $H$  were measured at four EC stations over contrasting vegetation types, within the source area of a 2.4 km long LAS path. The area-averaged LAS evaporation, calculated from the surface energy balance, using estimates of area-average net radiation and soil heat flux, was compared with aggregated EC  $L_vE$  measurements, weighted according to the proportion of each EC vegetation type in the LAS source area. The spatial variability of these fluxes over this scale is also presented, and aspects of the complex terrain, as they affect flux measurement, are discussed.

## 3.2 Measurements and Methods

### 3.2.1 LAS Measurements

The field experiment was conducted over a period of nearly five weeks during the late summer of 2004 (from 29<sup>th</sup> July to 31<sup>st</sup> August), although all EC measurements are available only until the harvest on 16<sup>th</sup> August. The measurements were made at Sheepdrove Organic Farm, Lambourn, Berkshire, UK (51.5° N, 1.5° W), situated on rolling chalk downland (75 m to 275 m above sea level). The soil is a variable mixture of flints, chalk, and brown rendzinas (Blyth et al., 2006).

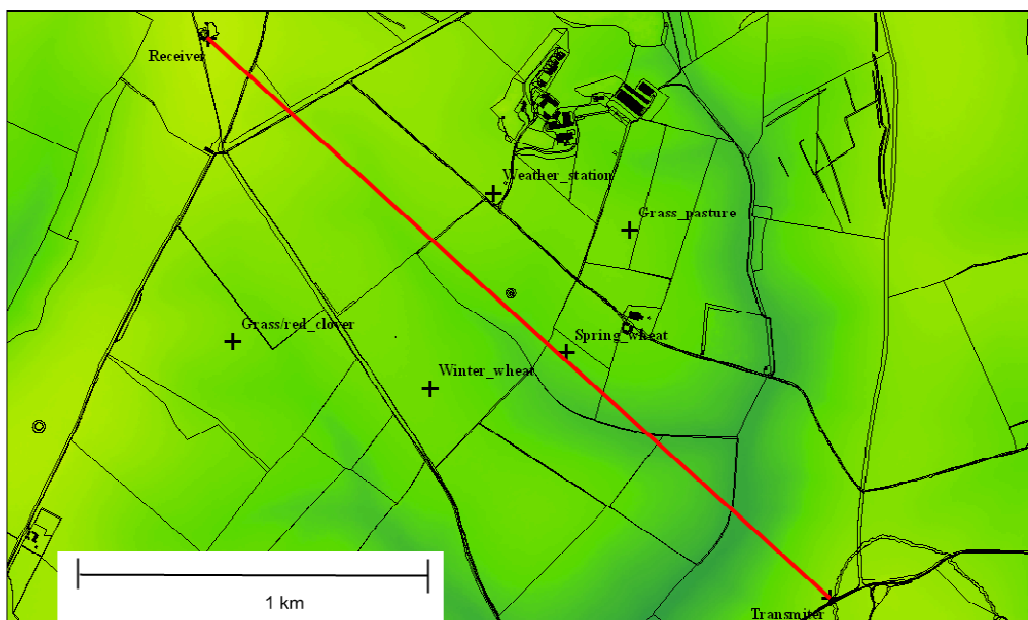
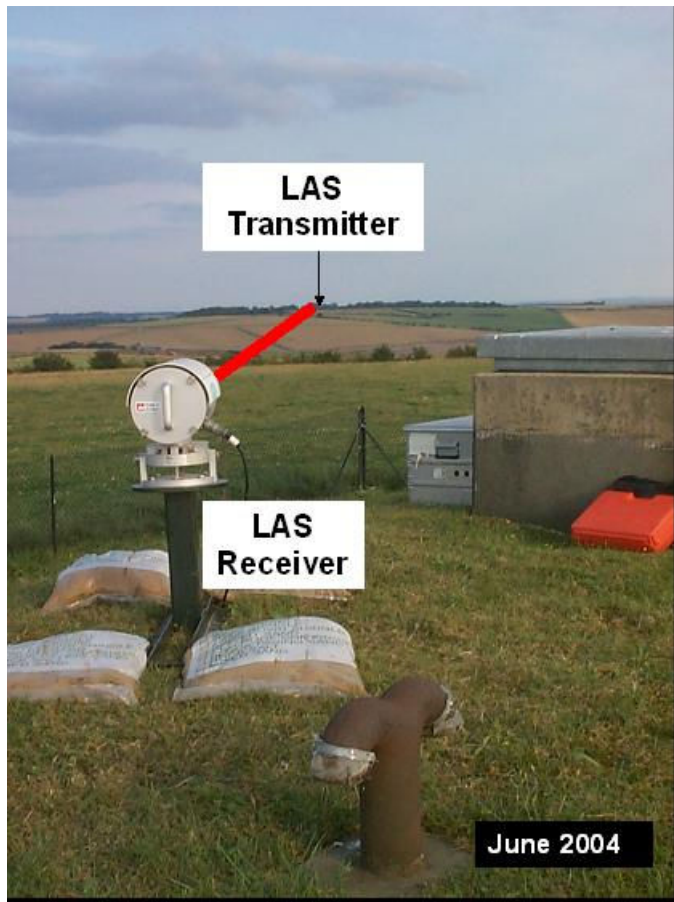


Figure 3-1 Map of Sheepdrove Organic Farm showing field instrument locations and LAS transmitter to receiver path (dark green indicates valleys, light green ridges).

An 880 nm wavelength LAS 150 (Kipp and Zonen B.V., Delft, The Netherlands) was deployed with a propagation path carefully selected with regard to the following criteria: (a) the landscape topography to provide beam height; (b) the beam is as high as possible above the land surface, and over smoothly varying terrain; (c) the height above the surrounding land surface is maximised in the directions normal to and away from the beam centre, i.e. that in these directions the land surface should not be steeply increasing in altitude; (d) the preferred path compass-alignment is NW-SE, being normal to the prevailing wind direction (SW) – to maximise the LAS source area – and avoiding coupling of sunlight into the optical transceivers at low sun angles (i.e. at sunrise and sunset); (e) the path length is greater than 2 km, with a mixed agricultural source area. Tall towers were not used because any mounting or mast vibrations directly contribute unwanted noise to the measured scintillation signal; it was preferable to take advantage of the topography. This also reduced costs and avoided working at height. The selected path passed over a dry valley to the SE (providing most of the beam height), and followed a smaller tributary valley which optimised suitability to criteria (a), (b) and (c), whilst also being NW-SE aligned. The location of the LAS path over-laid on the farm field map is shown in **Figure 3-1**.



**Figure 3-2 View from LAS receiver at Stancombe Reservoir**

A convenient grass-covered water company supply tank at the NW end of the path gave the receiver additional height (2 m) over the surrounding field and a secure enclosure (Figure 3-2). The transmitter was mounted at 1.5 m on a steel post concreted into the chalk (Figure 3-3). The path-length of 2.43 km was measured by a GPS survey, and verified from digital map data.

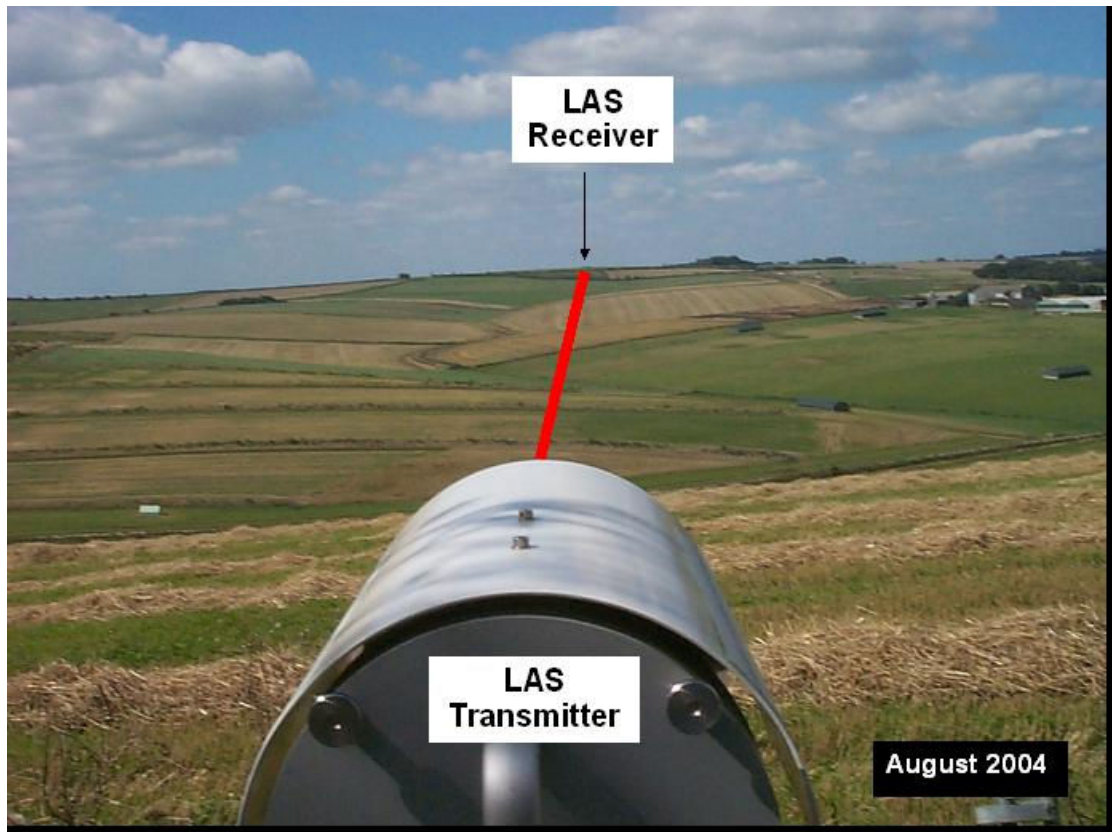


**Figure 3-3 LAS 2.4 km path setup at Sheepdrove Organic Farm**

Ten-minute means of the LAS measured near-infra-red turbulent structure parameter ( $C_{n^2}$ ) and the mean signal intensity were recorded on a CR10 data logger (Campbell Scientific Ltd., Shepshed, UK). These data were combined with the weather station measurements of air temperature, barometric pressure, wind speed and relative humidity (RH). A roughness length of 0.1 m was estimated from the literature (Panofsky and Dutton, 1984).  $H_{LAS}$  was then calculated by iteration with a computer program written in the R language (R, 2008), using the stability function of de Bruin et al. (1993) for unstable conditions.

### 3.2.2 Meteorological and Soil Measurements

A Skye Instruments weather station (denoted WS, Skye Instruments Ltd., Llandridod Wells, UK) with a four-component radiometer (CNR1, Kipp and Zonen) to measure incoming and outgoing shortwave and longwave radiation (as well as net radiation,  $R_n$ ) was located close to the centre of the LAS path (Figure 3-1). The WS was operated by the LOCAR Catchment Services Team and provided hourly data.

Alongside each of the EC stations were additional net radiation measurements (Kipp and Zonen NRLites), and at the grass pasture site (GP) another CNR1. Some stations also had soil heat flux plates just below the soil surface (10 mm depth) – at the grass/red clover ley (GC) site a Thornthwaite Model 610 (C. W. Thornthwaite Associates, New Jersey, USA) and at GP and WS sites the Hukseflux model HFP01 (Hukseflux, Delft, The Netherlands). Near-surface soil moisture was monitored at GC by a Campbell CS616, and a fully equipped LOCAR soil station was adjacent to the GP site. Canopy/soil surface temperatures were measured with Everest InfraRed Thermometers (IRT) model 4000.4 ZL (Everest Interscience Inc., Tucson, AZ, USA). A summary of the instrumentation at each site is shown in Table 3-1.

**Table 3-1 Summary of In-Field Measurements**

	Winter Wheat (WW)	Spring Wheat (SW)	Grass Pasture (GP)	Grass /Red Clover (GC)	Weather Station - Grass (WS)
net radiation, $R_n$	NRLite	NRLite	NRLite & CNR1	NRLite	CNR1
$H$ by EC	R3	R3	R3	R3	none
$L_vE$ by EC	LI7500	LI7500	energy balance	energy balance	none
soil heat flux, $G$	none	none	HFP01 at 10 mm	Model 610 at 10 mm	HFP01  At 300 mm
soil moisture	none	none	LOCAR soil station	CS616	none
soil temperature	Several depths	Several depths	Several depths	50 mm depth	300 mm depth
surface temperature	IRT	IRT	IRT	IRT	none

### 3.2.3 EC Measurements

The four EC flux station sites were located over winter wheat (WW), spring wheat (SW), GP and GC; these locations are shown in **Figure 3-1** and **Figure 3-6**. The maximum distance between these sites is about 1.3 km, and the maximum difference in altitude is about 30 m. The vegetation types were selected to be representative of types across the wider landscape, and within fields that contributed significantly to the source area of the LAS path. Care was taken to locate the EC measurements within the fields where the topography was smoothly varying (i.e. without abrupt local features), and where possible near to a ridge or plateau in order that measurements should be representative of well-developed turbulence (when such conditions existed), and with mean streamlines close to horizontal. For the EC source area to be representative of a single field type, required that the EC stations were located away from field boundaries (which often follow ridges); thus the selected EC locations had to compromise these two factors – mostly being on gently sloping terrain, towards ridge-tops but not atop them. It was assumed that for unstable conditions each EC station was representative of the field in which it was measuring and in all cases the within-field fetch was at least 180 m, with a measurement height resulting in at least 80 % of the source area being within-field, for typical unstable conditions.

There were some differences in the instrumentation of the EC stations deployed, due to the high equipment demand of this experiment. All EC stations deployed Omnidirectional (R3) Research Ultrasonic Anemometers (Gill Instruments Ltd., Lymington, UK) sampling at 100 Hz and output as 20 Hz means. For each site an improved linear sonic temperature calibration was applied (calibrated against a precision thermometer in an environmental

chamber, using dry air). The R3 was combined at WW and SW with LI7500s (LiCor Inc., Lincoln, NE, USA) open-path CO<sub>2</sub>/H<sub>2</sub>O fast response infrared gas analysers (IRGAs); the WW site is shown in Figure 3-4. Except at the GP station, all data were recorded at 20 Hz from the digital serial output of the sonic, to purpose-built loggers, and where present, the LI7500 was logged via the Gill Sensor Input Unit (SIU). The GP station used the analogue outputs from the sonic from which hourly EC statistics were calculated (using an autoregressive moving average (ARMA) to detrend with a time constant of 10 minutes) and logged using a Campbell 23X data logger.



**Figure 3-4 Winter Wheat (WW) Radiometers (left) and EC Flux Station (right).**

Raw 20 Hz data were processed using CEH's FluxView software (except for GP). The sonic anemometer data were recalibrated for the full range (0 to 90°) of angle-of-attack (AoA) of the instantaneous wind vector, since the Gill sonic anemometers used are supplied with a calibration only valid between +/- 20° AoA, following Gash and Dolman (2003) and the calibration algorithms of Nakai et al. (2006). It was found that this gave a linear increase in  $H$  of

6.0%, and this same flux correction was then applied to the hourly mean flux data from GP – these fluxes were also interpolated to give 30 minute data.

The EC method is discussed and fully referenced by Lee et al. (2004), and further details and analysis of this method is given in Appendix 1. FluxView was configured consistently for these sites to: (a) apply the AoA correction; (b) apply an auto-regressive moving average (ARMA) detrend with a 10 minute time constant; (b) seek maximum temperature-humidity correlation to determine gas analyser time lag for each 30 minute period; (c) apply two-axis rotations – to align the horizontal wind vector to the 30 minute mean wind direction, and to force the vertical wind component to zero; (d) humidity correct the heat flux; (e) apply the Webb-Pearman-Leuning (WPL) density corrections; (f) apply low and high frequency flux loss corrections.

### 3.2.4 LAS Effective Height and Source Area Analysis

For a given sensible heat flux,  $C_{T^2}$  is strongly dependent on the measurement height ( $z^{-4/3}$ , Eq. 2-34). As the LAS beam passes over varying topography, the measurement height varies along the pathlength. Furthermore, the sensitivity of the LAS also varies along the pathlength – according to the path weighting function (Eq. 2-18). These two influences must be combined in deducing an *effective height* ( $z_{eff}$ ) for the LAS (Hartogensis et al., 2003), in order to calculate  $H_{LAS}$  from the path-averaged ensemble mean,  $\langle C_{T^2} \rangle$ , measured by the LAS. The methods and theory developed and applied are shown in Chapter 4 and Evans and de Bruin (2009).

$z_{eff}$  was found to be 32 m, using the estimation method described by Hartogensis et al. (2003), and the same value of  $z_{eff}$  was produced by the exact solution of Evans and de Bruin (2009) – both using the same map topographic data. The complex topographic profile below the LAS beam is shown in Figure 3-5.



**Figure 3-5 The vertical profile of the land surface (black line) directly beneath the LAS path (red line)**

Calculation of the source area was required to compare the LAS flux measurements with the EC results. The source area calculation also depends on the measurement height along the path, with greater heights having a larger source area, for the same atmospheric stability conditions. As with the effective height, it is also necessary to consider the path weighting function of the LAS, to calculate the total source area for the LAS pathlength.

The calculation of the source area is a complex procedure, and uses a footprint model (Schuepp et al., 1990) developed for homogeneous flat terrain. The application of the footprint model may be justified by the measurement height being relatively high, above the blending height, so that the turbulence is expected to be smooth and the fluxes from different sources well-mixed. In a manner similar to Meijninger et al. (2002a), the LAS beam

was treated as a line of point measurements, with the footprint calculated at 20 discrete points, using five different values of the beam height (38.0, 41.4, 36.0, 30.0 and 16.6 m), for typical unstable conditions, and for the case of a south-west wind direction (perpendicular to the LAS path). Each of the 20 footprints was then multiplied by the LAS path weighting function (Eq. 2-18) evaluated at the corresponding point along the path, to produce the source area weighting map for these typical conditions.

The source area was then overlaid on the land cover map data to identify the percentage of each land cover class in the source area (a visual representation of this analysis scheme is shown in Figure 3-6). The land cover types were then binned into the closest vegetation type that was represented by an EC station, thereby determining the percentage contribution of each EC station to the LAS areal average measurement, under typical conditions.

The result of the source area mapping for typical conditions is shown in Figure 3-6. It is important to note the effect of the varying measurement height on the calculation of the footprint – which leads to an asymmetric and complex source area intensity pattern. Changes in  $z_{LAS}$  are not symmetrical about the path centre, so lead to a spatial bias in the footprint.

Using this simplified analysis, for typical conditions and south-west wind direction, the estimated contribution to  $H_{LAS}$  was calculated for each measured vegetation type (

Table 3-2). Where no EC measurement was available for the actual land cover type of a particular field, then the nearest measured land cover type was selected to represent the contribution from that field, e.g. borage was approximated by spring wheat (SW).

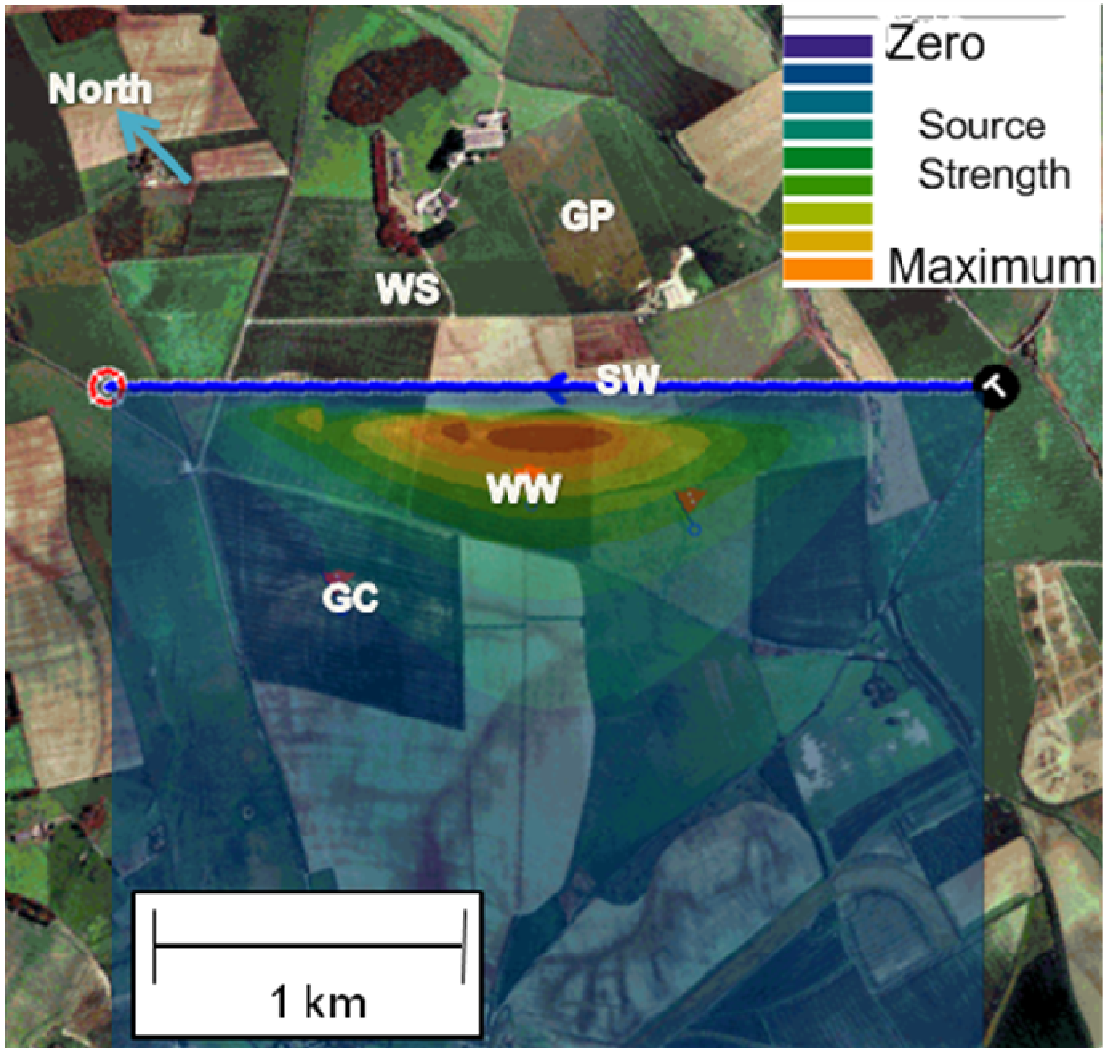


Figure 3-6 Typical LAS source area strength contour map overlaid on the field instrument map. The instrument locations are denoted: GC - grass/red clover; GP – grass pasture; SW – spring wheat; WW – winter wheat; WS – weather station. The LAS path is shown as the solid blue line. The aerial photograph is earlier than 2004 with different land cover. Typical conditions are south-westerley wind direction and  $L_{ob} = -67$ .

**Table 3-2 Contribution to LAS source area by EC vegetation type.**

EC Vegetation Type	Contribution to LAS source area /%
Grass/clover (GC)	38
Winter wheat (WW)	33
Spring wheat (SW)	15
Grass pasture (GP)	14

### **3.2.5 Data Quality Control**

The open-path IRGA data were quality controlled (QC) for the presence of rain or dew on the analyser window, which may render the data invalid. In such cases, the evaporation data were set to missing, and the weather station RH data was used to correct the sonic heat flux for humidity.  $L_vE$  data were rejected when: a) the rain-gauge recorded rainfall; or b) liquid water was otherwise assumed to be present in the open-path of the IRGA (either because of rainfall below the rain-gauge threshold or more often due to rainwater or condensation on the IRGA windows. Condition b) was declared when the variance of the IRGA-measured water vapour density was greater than a set multiple of the sonic temperature variance, or the water vapour density was outside of its expected range. For this analysis, the QC for  $L_vE$  data was also effectively applied to all other data including the LAS and radiometers, since the analysed subset only included records with acceptable

$L_vE$  data. The sonic temperature (and sensible heat flux) is normally unaffected by rain, except at very high rain rates, or if the transducers are particularly dirty; these data were rejected by detecting when the variance of sonic temperature was above a set limit. A maximum value was set for the LAS  $C_{T^2}$  of  $0.03 \text{ K}^2 \text{ m}^{-2/3}$ , above which data were rejected, these few very high values were probably caused by sporadic beam interruptions e.g. by farm vehicles or personnel operating close to the transceivers. Finally, values of  $H_{LAS}$  greater than five times the net radiation ( $R_n$ ) were rejected as physically implausible (< 1% of unstable data) – this very large multiplier was used to allow for large differences when the absolute values are quite small (<  $50 \text{ W m}^{-2}$ ) and when there may be a lag between  $H_{LAS}$  and  $R_n$  at the timescale of 30 minutes.

### **3.3 Results**

#### **3.3.1 EC Performance**

Quality controlled fluxes ( $H_{EC} + L_vE_{EC}$ ) were plotted against the available energy ( $R_n - G$ ) for individual flux stations, to test the EC energy balance closure.  $L_vE_{EC}$  measurements were not made at GP, and therefore the energy balance closure cannot be calculated. The results are summarised in Table 3-3.

**Table 3-3 EC Flux Station Energy Balance Closures**

<i>Flux Station Land Cover</i>	<i>Slope</i>  $(H_{EC} + L_v E_{EC})$ versus $(R_n - G)$	<i>Offset</i>  $W m^{-2}$	$r^2$
<i>Grass/clover (GC)</i>	<i>0.95</i>  <i>(measured during pre- experiment period with LI7500 installed)</i>	<i>6.7</i>	<i>0.95</i>
<i>Winter wheat (WW)</i>	<i>0.91</i>	<i>23.0</i>	<i>0.88</i>
<i>Spring wheat (SW)</i>	<i>0.92</i>	<i>3.9</i>	<i>0.96</i>

The energy balance closures for all sites, represented by the slope in column 2 of Table 3-3, are fairly close to unity, indicating reliable measurements. The slopes are 5 to 9% less than 1.0 (the expected slope if the energy balance is fully closed). This is better than most published results, probably because of the short and relatively smooth vegetation; however there is increased uncertainty here in  $R_n$ , compared to some studies, because lower-cost NRLite radiometers were used. The winter wheat EC station has the largest offset and smallest  $r^2$  value, which is probably due to poorly represented soil heat flux; the grass/clover soil heat flux ( $G_{GC}$ ) data were used to approximate the winter wheat and spring wheat soil heat fluxes ( $G_{WW}$  and  $G_{SW}$ ), as there were no soil heat flux plates installed below these crops. During this study the

mature winter wheat had a low LAI of 2.0 to 2.3 (as measured by a SunScan ceptometer, Delta-T Devices Ltd., Cambridge, UK) and a large proportion of the soil surface exchanges radiation with the atmosphere. Thus use of  $G_{GC}$  increases scatter in the data, on short (30-minute) timescales, and the soil thermal lag is probably responsible for the larger regression offset. Nevertheless, the averaged energy balance closure for WW is more closed than typical published results. The spring wheat energy balance closure regression has the highest  $r^2$  value and smallest offset, showing that the approximation of  $G_{GC}$  is reasonable, even on short timescales, as the spring wheat remained green with an average LAI of 4.1. The magnitude of the winter wheat (and to some extent spring wheat) crop  $G$  values is expected to be higher than that of  $G_{GC}$  which would slightly improve the energy balance closure; however, since  $G$  is a relatively small component of the energy balance, no attempt has been made to recalibrate these data for the crop fields.

### 3.3.2 Field EC Measurements Compared with the LAS Sensible Heat Fluxes

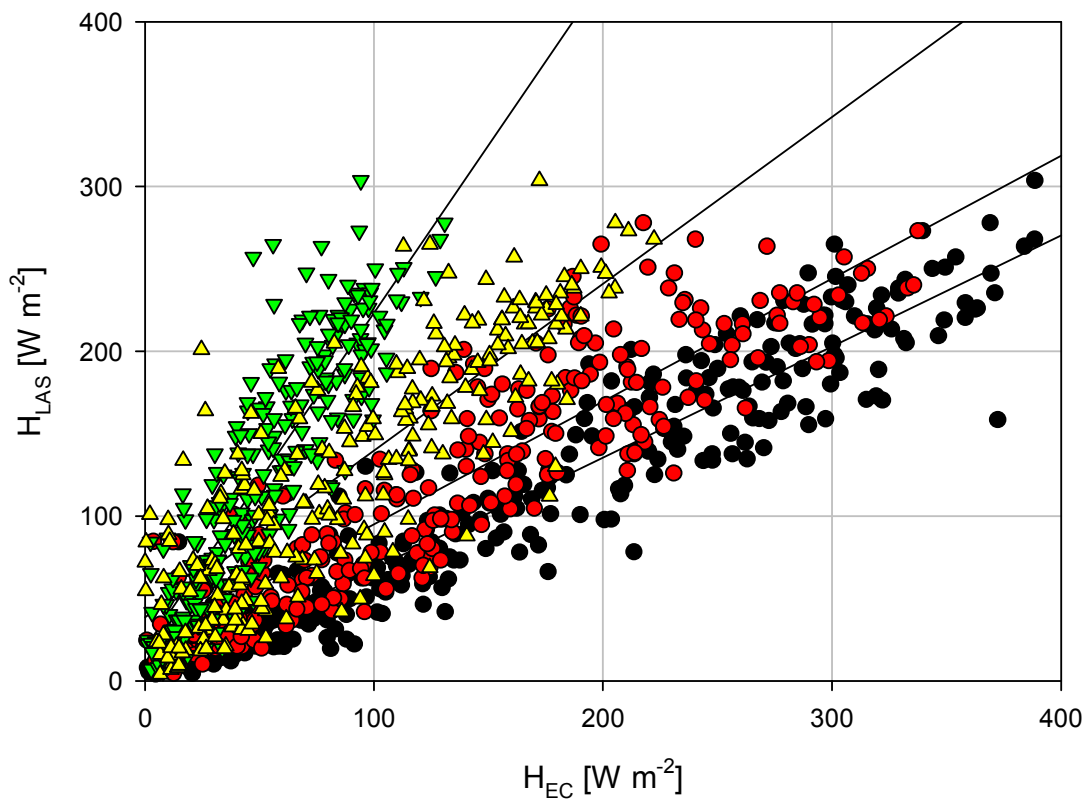


**Figure 3-7**  $H_{LAS}$  regressions for each  $H_{EC}$ : grass pasture (GP, green), grass/red clover (GC, yellow), spring wheat (SW, red), and winter wheat (WW, black); from 30<sup>th</sup> July to 16<sup>th</sup> August 2004.

Figure 3-7 shows each EC measurement of sensible heat flux compared to  $H_{LAS}$ , which is expected to be representative of a spatial average which includes a significant contribution from each of these land surface types.

There is a range of regression slopes of  $H_{LAS}$  versus  $H_{EC}$  from 0.67 (senesced WW) to 2.03 (GP), these are summarised in **Table 3-4**.

**Table 3-4 Linear regression coefficients by land cover type.**

$$H_{LAS} = Slope \times H_{EC} + Offset$$

Regression Coefficients	Slope	Offset	$r^2$
Grass/Clover (GC)	1.01	39	0.75
Winter Wheat (WW)	0.67	0.8	0.91
Spring Wheat (SW)	0.75	21	0.84
Grass Pasture (GP)	2.03	20	0.81

There is the strong dependence of evaporation on plant transpiration, which controls the residual energy available as sensible heat flux. The senescent winter wheat is not transpiring, and when the surface soil moisture dries out, hence causing soil evaporation to be very low, the total evaporation is quite small, with most of the available energy being transported to the atmosphere as sensible heat. Spring Wheat shows some similarly large  $H_{EC}$  values, but with a much larger spread of data (with respect to  $H_{LAS}$ ), as the crop is later senescing, and is still partially transpiring, with the rate of transpiration declining steadily during this period up to the harvest (16<sup>th</sup> August 2004). The grass/red clover field has modest  $H_{EC}$  values, indicating substantial transpiration, whilst the grazed grass has the lowest  $H_{EC}$  and highest

evaporation, due to strong transpiration, as the grass rapidly grows in response to grazing.

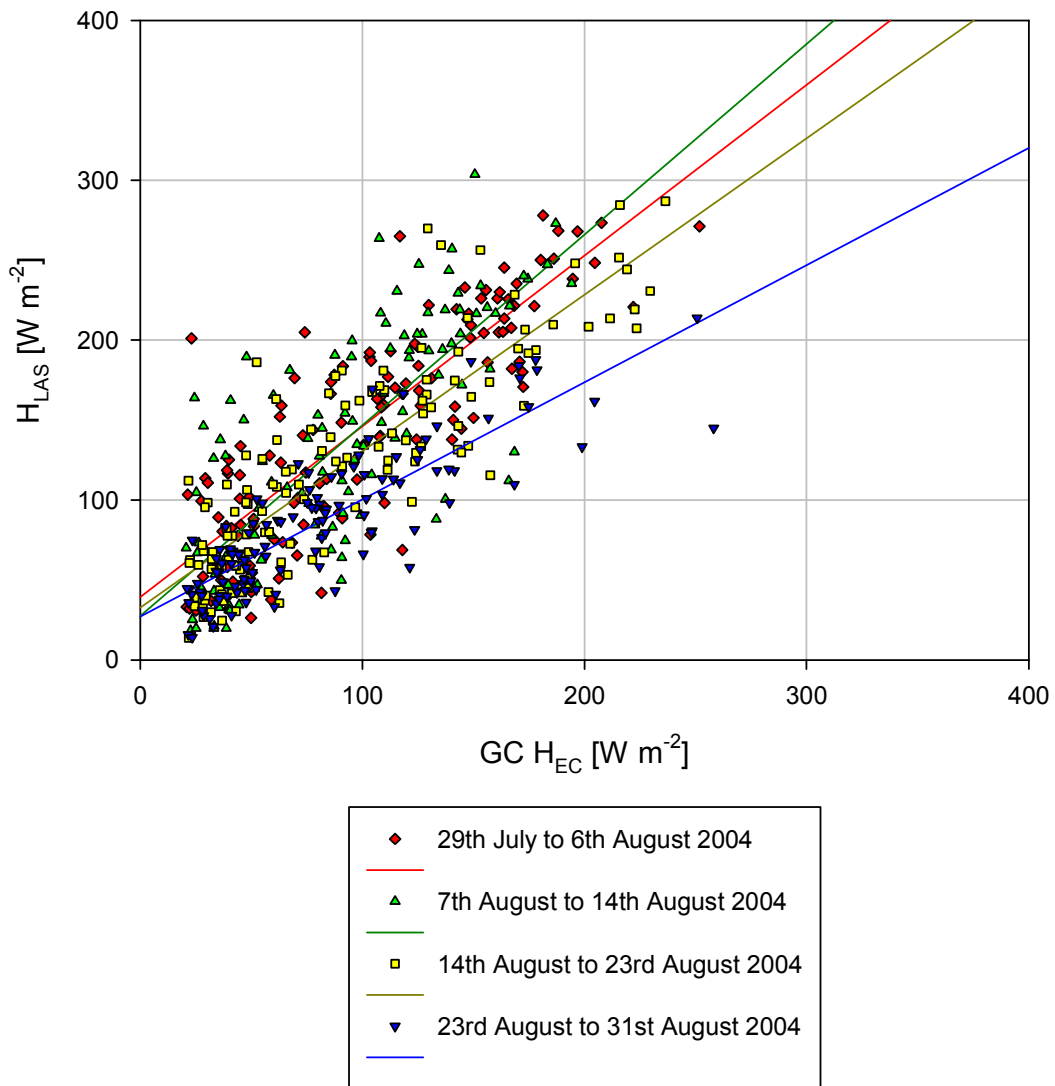


**Figure 3-8 Short chronological periods of  $H_{LAS}$  compared with grass/red clover (GC)  $H_{EC}$ , showing the change in the regression slope over time. Note data with  $H_{EC} > 20$  W m<sup>-2</sup> were selected to avoid the sign ambiguity in the determined  $H_{LAS}$  values.**

Regression Coefficients	Slope	Offset	r <sup>2</sup>
29th July to 6th August 2004	1.07	39	0.66
7th August to 14th August 2004	1.19	27	0.60
14th August to 23rd August 2004	0.98	33	0.74
23rd August to 31st August 2004	0.73	27	0.72

**Table 3-5 Linear regression coefficients by time period for grass/read clover (GC).**

$$H_{LAS} = Slope \times H_{EC} + Offset$$

In Figure 3-8  $H_{LAS}$  is compared directly to GC  $H_{EC}$ , with the data separated into chronological blocks (nominally weeks), as the relationship of these measurements changes over time during August. The slope of the relationship of  $H_{LAS}$  is reduced to 73% of  $H_{EC}$ , by the last week of August, whilst peak  $H_{EC}$  values are not particularly reduced.

### 3.3.3 LAS Sensible Heat Fluxes Compared with Aggregated EC Sensible Heat Fluxes

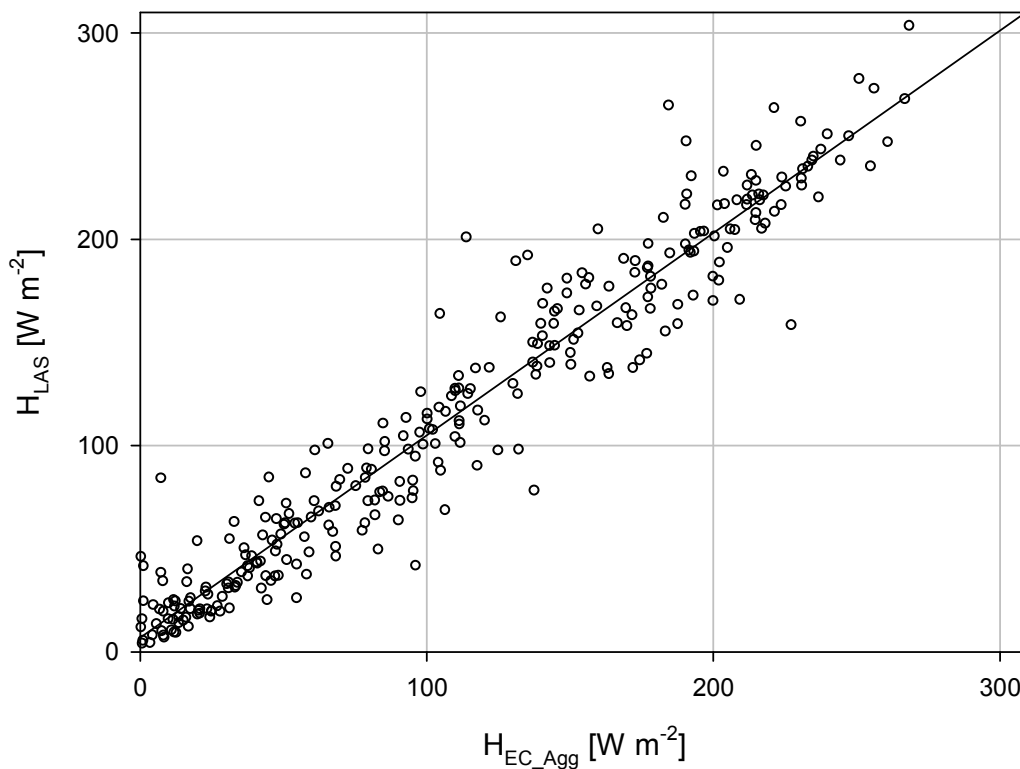


**Figure 3-9**  $H_{LAS}$  compared with  $H_{EC\_Agg}$  (31<sup>st</sup> July to 16<sup>th</sup> August 2004);

$$H_{LAS} = 0.98 \times H_{EC\_Agg} + 7.0, r^2 = 0.93.$$

Using the percentage contributions of land cover types to the LAS source area (Table 3-2), an aggregated EC sensible heat flux ( $H_{EC\_Agg}$ ) was calculated, which is the best estimate with which to compare  $H_{LAS}$ , given the simplified assumptions above; this is shown in Figure 3-9. The slope of the regression is 0.98, which is not significantly different from unity, as the

estimated experimental error is 5 % for the EC measurements. There is a small bias error which is significant at lower flux values, due to the offset of the regression. The  $r^2$  of the regression is 0.93.

### 3.3.4 Latent Heat Fluxes Estimated from the LAS Compared with Aggregated EC Measurements

The same aggregation weights as in Table 3-2 were used to calculate an areal-averaged net radiation ( $R_{n\_Agg}$ ), and using an aggregated-average soil heat flux ( $G_{Agg}$  - measured in the grass/red clover and grass pasture fields only), the evaporation from the LAS ( $L_v E_{LAS}$ ) was calculated as the residual of the land surface energy balance:

$$L_v E_{LAS} = R_{n\_Agg} - G_{Agg} - H_{LAS}$$

#### Eq 3-1

The resulting  $L_v E_{LAS}$  is compared with  $L_v E_{EC\_Agg}$  in Figure 3-10. The calculated evaporation from the LAS agrees very well with the aggregated EC evaporation, with a regression slope of 0.96. The  $r^2$  value of 0.90 is not as high as that for the aggregated sensible heat flux regression because the additional uncertainties of  $R_n$  and  $G$  have been introduced.

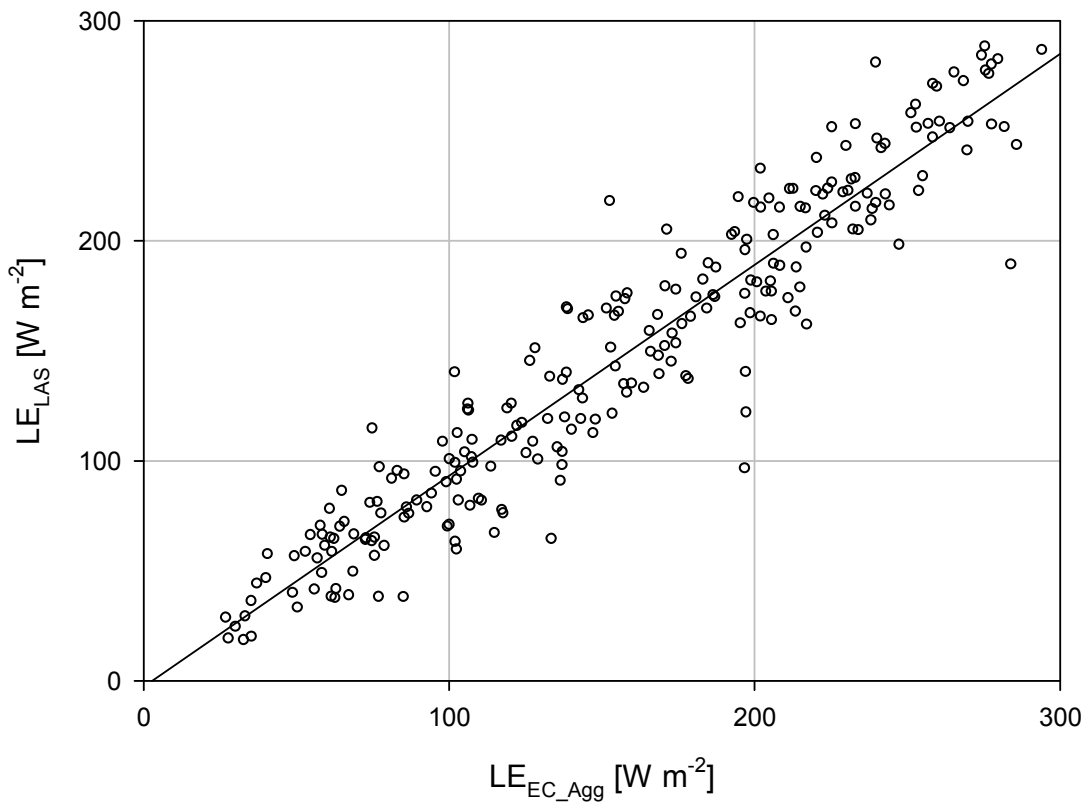


**Figure 3-10**  $LE_{LAS}$  compared with  $LE_{EC\_Agg}$ ;  $LE_{LAS} = 0.96 \times LE_{EC\_Agg} - 2.7$ ,  $r^2 = 0.90$

### 3.3.5 Diurnal Variations

Figure 3-11 shows the course of the sensible and latent heat fluxes at both the field scale and at the scale of the LAS source area. Firstly, as has been shown in Figure 3-7, there is very high inter-field variability of these fluxes. The top panel of Figure 3-11 shows that  $H_{LAS}$  and  $H_{EC\_Agg}$  are almost the same for much of the time.

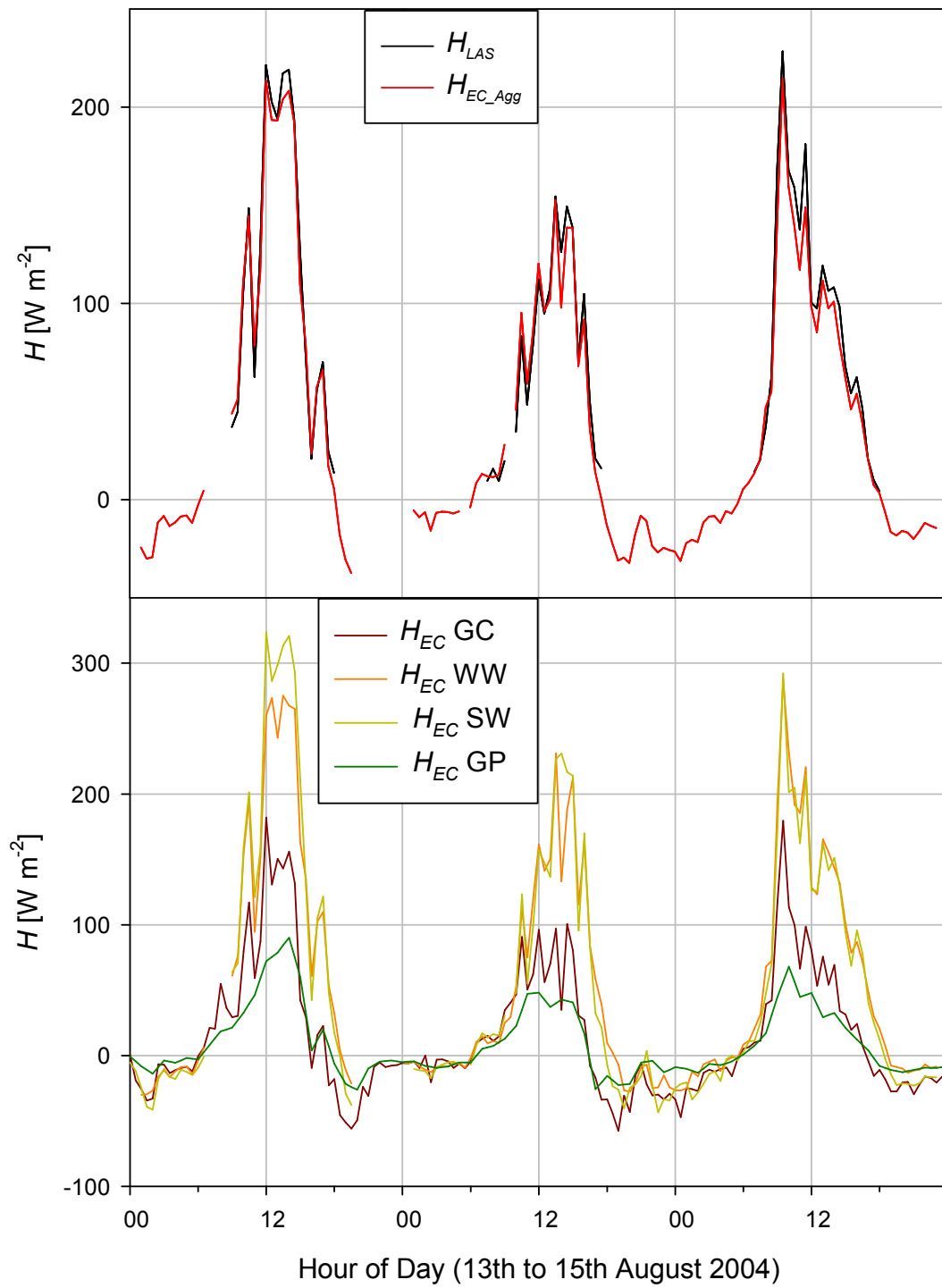


**Figure 3-11 Diurnal course of sensible heat fluxes, showing high inter-field variability and close agreement of LAS with aggregated EC sensible heat flux.**

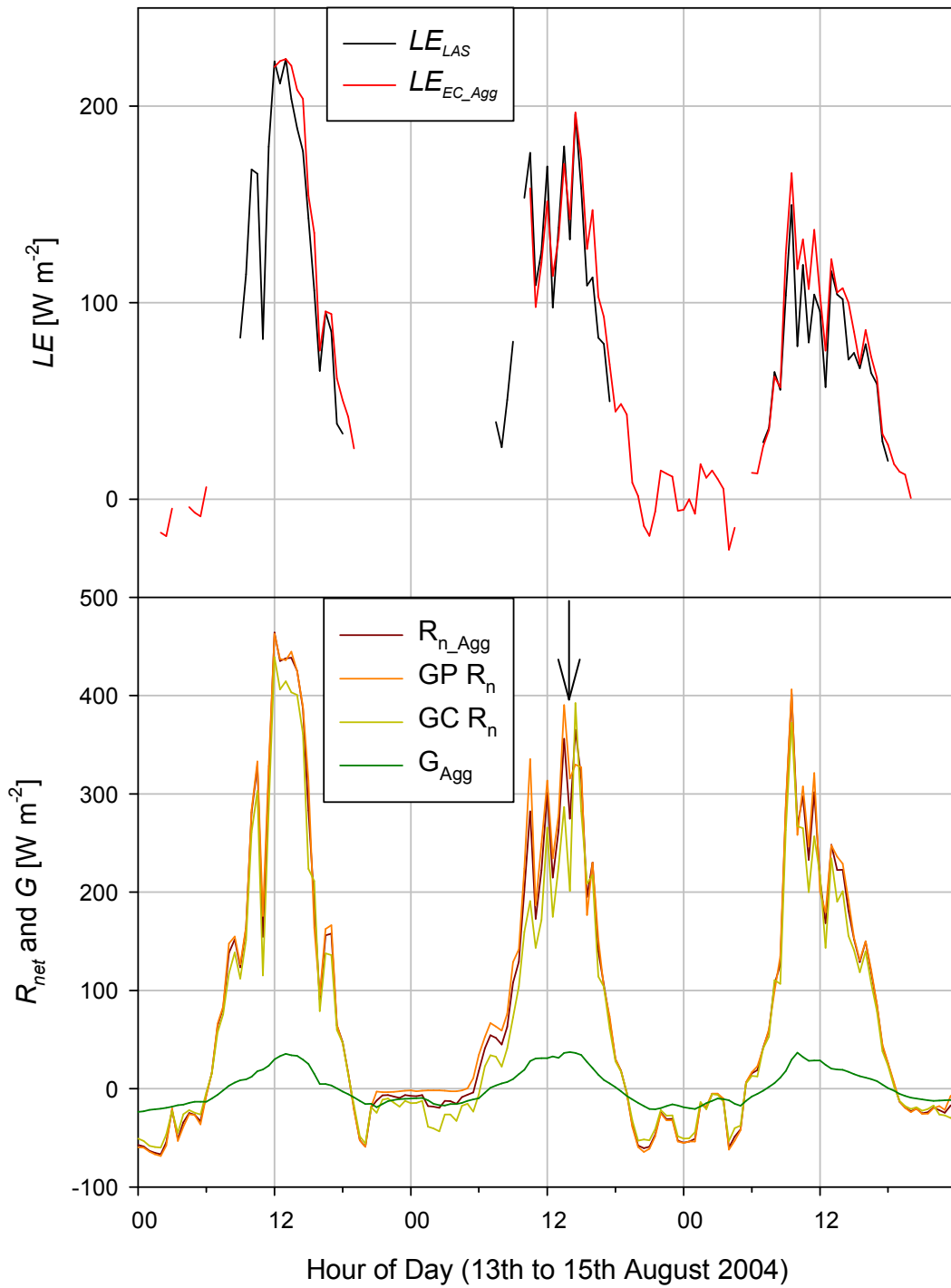


**Figure 3-12 Diurnal  $LE_{LAS}$  compared with  $LE_{EC\_Agg}$  (top panel). Net radiation and ground heat flux (bottom panel).**

### **3.4 Discussion**

The measured fluxes at the field scale (Figure 3-7) are very different from one another, depending on the vegetation type, phenological development, and soil moisture content. These strongly contrasting fluxes provide a good test of whether the LAS measured a representative spatially averaged sensible heat flux at the landscape scale, over the varying topography of the chalk downland. Firstly, these conditions provide a wide range of  $H$  in the source area of the LAS at any given time of day, testing the accuracy of the LAS areal average. Secondly, these varying fluxes along the path, provide theoretical challenges to the calculation of  $H_{LAS}$ , and even the measurement of  $C_{n^2}$  - these challenges are addressed by the concept of the blending height, and the validity of the blending height is therefore tested here. Thirdly these tests are conducted over complex topography, which gives rise to further theoretical challenges, and tests the concept of the effective height.

There are several uncertainties that affect the calculated magnitude of  $H_{LAS}$ : the estimated  $z_0$ , the calculated  $z_{eff}$ , and the assumed MOST stability function for  $C_{T^2}$ . The latter has the strongest overall effect, and the selection of the de Bruin et al. (1993) stability function over the Wyngaard et al. (1971) function leads to an increase in  $H_{LAS}$  of 12 %. The De Bruin stability function is commonly applied in scintillometry and the original data to which it has been fitted may be more appropriate than those of the Wyngaard et al. (1971).

In Figure 3-7 and Table 3-4 there are high correlations between the  $H_{LAS}$  and  $H_{EC}$  measurements (with  $r^2$  between 0.75 and 0.91), as would be expected for an areal-average measurement. These highly correlated linear relationships suggest that an aggregated mean of the EC measurements by land cover type,  $H_{EC\_Agg}$ , can be used to test the representativity of the areal-average  $H_{LAS}$ .

Where  $H_{EC}$  against  $H_{LAS}$  has higher scatter (particularly for SW), it was found that the phenology changes the relationship with  $H_{LAS}$  i.e. that the lower  $r^2$  value probably partly results from the phenology of a particular vegetation that was atypical of the average land cover phenology in the source area of the LAS. Hence a lower  $r^2$  does not necessarily indicate poorer performance of the LAS but probably that a particular land cover type is not typical of the LAS source area (e.g. SW only accounts for 15 % of the LAS source area land cover type).

The dependence on the state of the vegetation of a particular field, relative to the whole LAS source area has been further investigated in Figure 3-8. It was found that the large scatter for  $H_{LAS}$  versus  $H_{EC}$ , could be best explained by the chronological analysis of this data – which accounts for the changing relationship between  $H_{LAS}$  and  $H_{EC}$  of a particular field. This is likely to be due to changes in the mean diurnal transpiration rate of a particular land cover compared to that of the whole LAS source area. However, soil evaporation may also play a role, where bare soil is exposed to the atmosphere beneath the relatively low density organic crops.

The contribution to  $H_{LAS}$  from fields other than GC, is reduced relative to GC, in the latter half of August (Figure 3-8), when there was moist bare soil post harvest (with above-average rainfall for August). After harvest, surface soil moisture availability in these fields plays a critical role in controlling  $H$  via increased  $L_vE$ . It is important to note that although the  $H_{EC}$  for the GC field changes from having a regression of slope 1.07 with  $H_{LAS}$  to 0.73 (Table 3-2), the  $r^2$  values and the quality of linear relationship with  $H_{LAS}$  remain fairly much of a similar order - provided that consideration is given to the land cover and soil moisture changes in the LAS source area, in this case by applying this chronological analysis.

$H_{LAS}$  compared to  $H_{EC\_Agg}$  (Figure 3-9) shows that the LAS accurately represents (with no significant bias, within the experimental error) the areal average of its source area, as measured by the EC stations. The small regression offset ( $8.4 \text{ W m}^{-2}$ ) may be due to LAS instrumental noise, which is currently being investigated (this is thought to contribute a small but fairly constant scintillation signal). The  $r^2$  of the regression is 0.93, significantly higher than the highest value of  $r^2$  of the regression with any individual EC station, confirming that  $H_{LAS}$  better represents  $H_{EC\_Agg}$  than it does any single contributing field. The high quality of this relationship is especially good considering that all wind directions have been included – detailed analysis did not show a significant bias with wind direction, suggesting that the land cover percentage contributions did not vary significantly as the LAS source area changed with wind direction. Land cover mapping showed that this was a reasonable assumption.

The regression of  $LE_{LAS}$  with  $LE_{EC\_Agg}$  is remarkably close to one-to-one and shows that this is an accurate method for the landscape-scale measurement of evaporation, even over complex topography. Accuracy then is probably limited by the availability of areally representative  $R_n$  and  $G$ , and the relatively high errors of these measurements (of the order of 10%) even when only considering single point samples.

The time series plots of Figure 3-11 reveal more clearly under what conditions the  $H_{LAS}$  differs significantly from  $H_{EC\_Agg}$ . There are specific times when these measurements suddenly diverge, and that such divergences do not always occur for the same value of  $H$ , nor for the same stability conditions, nor wind speed. These differences are most strongly correlated with high net radiation variance due to rapidly changing cloud cover, which produces a large spatial variance of  $R_n$  in the LAS source area. They may be explained in terms of the LAS source area no longer being represented adequately by the EC aggregation. For example, on 14<sup>th</sup> August 2004 in the mid-afternoon, the net radiation for GC (shown on the bottom panel of Figure 3-12) increases by nearly 50% (after a large dip), whereas that of GP is only increased by less than 25% (albeit from a larger starting value) and – at a low wind speed of 2 m s<sup>-1</sup> – this difference may be expected due to spatio-temporal differences in cloud cover, and longer averaging times are required to smooth out these differences. The spatial-temporal difference seen in the net radiation is reflected in the sensible heat fluxes, where  $H_{EC}$  (GC) and  $H_{EC}$  (WW) dip by 40-50 %, in contrast to  $H_{EC}$  (SW) and  $H_{EC}$  (GP) which stay fairly constant at that time. Under these conditions, it is not expected that the EC aggregation scheme will provide data representative of the LAS source area, because the

aggregation is only based on vegetation types and not spatial representation of the source area, therefore there is no account of net radiation spatial effects. Conversely, there is no significant difference between  $LE_{EC\_Agg}$  and  $LE_{LAS}$  at this time; the  $R_n$  used to calculate  $LE_{LAS}$  is reduced, such that agreement happens to be maintained, despite the differences in sensible heat.  $R_n$  is more spatially representative of the EC source areas than of the LAS source area. Improved representativity of  $R_n$  over the LAS source area would increase the accuracy of  $LE_{LAS}$ , although not necessarily provide better agreement of  $LE_{LAS}$  with  $LE_{EC\_Agg}$ , because of the latter's limited spatial representation of the LAS source area.

### **3.5 Conclusion**

It has been shown here, for the first time, that the LAS is a powerful and accurate technique to derive the areal-average flux from a mixed agricultural landscape with complex topography; this could otherwise only be obtained by aggregation of individual measurements made over each crop. Within the experimental uncertainties, a good agreement was found between sensible and latent heat fluxes as measured with the LAS (and the surface energy balance for  $LE_{LAS}$ ), compared to the EC fluxes aggregated for the different land surface types in the footprint; regression slopes were close to unity. Under the late-summer conditions of this experiment, with well-developed turbulence, the results validate the application of MOST to determine  $H_{LAS}$  from  $C_{T^2}$ , under these conditions of reasonably high  $z_{eff}$  (32 m) and strong

turbulent mixing, which keeps the blending height sufficiently low. The DeBruin stability function gives good results in this experiment.

The greater scatter of  $LE_{LAS}$  versus  $LE_{EC\_Agg}$  (compared with that of the respective sensible heat fluxes), is to be expected for two reasons: firstly additional errors are introduced as net radiation and soil heat flux data are required to calculate  $LE_{LAS}$  using Eq 3-1 – perhaps the largest errors relating to spatial representation of  $R_n$  for the LAS source area under non-stationary conditions; secondly the comparison made here, assumes that the EC fluxes for each vegetation type do not vary spatially in the source area, whereas the data shows lack of spatial stationarity for  $R_n$  and  $H_{EC}$ , and thus by inference, also for  $L_vE$ . The problem can be alleviated somewhat by using longer averaging periods for comparison.

Future applications of the LAS for large-area evaporation monitoring, using the surface energy balance, should focus effort into improved net radiation networks, which sample the LAS source area spatially as well as representative vegetation classes. In practice, such a large array of radiometers at many different locations, often interfering with normal farming operations, is not an attractive proposition. Other methods such as satellite remote sensing may prove more convenient, if such pixel averages can be aligned with the LAS source area, and the effect of cloud cover accurately retrieved. It is likely that in the near-future some combination of ground-based point measurements and remote-sensing will provide the most accurate net radiation data, with remote-sensing providing a large area average to account for spatial variability.

Methods to obtain area-average estimates of  $G$ , and required estimates of thermal properties, from surface temperature and soil moisture content such as the one presented in Murray and Verhoef (2007a) and Murray and Verhoef (2007b), will also improve LAS-based evaporation estimates, in particular if these estimates could be obtained from remote sensing data (e.g. a combination of *Meteosat Second Generation* (MSG) and *Soil Moisture and Ocean Salinity* (SMOS) satellite data). Some combinations of scintillometer and MSG data for flux measurement have been suggested by de Bruin et al. (2004).

## **Chapter 4 The Effective Height for the Calculation of Heat Fluxes from Scintillometry over Complex Topography**

### **4.1 Introduction**

Only limited systematic studies have been devoted to the application of scintillometry over heterogeneous terrain: the Flevoland Experiment, in which the scintillometer paths were parallel to the surface (Meijninger et al., 2002; Meijninger et al., 2002) and LITFASS-2003 (Beyrich et al., 2006; Meijninger et al., 2006). These results show that the method has to be applied above or just below the blending height, in order that MOST can be applied to calculate the fluxes, as MOST is still applicable in the ‘blended’ surface layer<sup>1</sup>. The implication of this work is that scintillometer measurements over heterogeneous terrain should be made at a height of several tens of meters above the land surface, where the fluxes are well-blended. This requires either tall towers or masts, but this is costly and inconvenient, so in practice tall buildings or other prominent land surface features (e.g. hills) may be used

---

<sup>1</sup> Meijninger et al.(2006) and Meijninger et al.(2002) considered the aggregation of fluxes when measuring just below the blending height. Here, only well-blended fluxes above the blending height are discussed.

to mount the transceivers at sufficient height. For example, across a wide valley, a path may be found that conveniently uses the topography to provide sufficient height for the scintillometer beam, with the transceivers themselves being mounted relatively close to the ground (de Bruin et al., 1995; Green et al., 2000; Poggio et al., 2000). The beam is then often slanted with respect to the underlying land-surface.

Hartogensis et al. (2003) considered a slanted LAS path over predominantly flat savannah landscape, introducing the concept of the *effective height* ( $z_{ef}$ ) for the calculation of  $H$  using MOST. Note that although Hartogensis et al. (2003) only investigated  $z_{ef}$  for the LAS, Meijninger et al. (2006) used the same method to find  $z_{ef}$  which was then applied to the MWS, without justification. In this LITFASS-2003 experiment, the two-wavelength method was applied over moderately varying topography, with slanted beams. Hartogensis et al. (2003) found that  $z_{ef}$  for the LAS depends on the atmospheric stability (Obukhov Length), and that the scintillometer's path-weighting function plays an important role. This is due to the fact that scintillometers measure path ensemble means of structure parameters and that in the constant flux layer these vary with height. There have been no studies to determine  $z_{ef}$  for the LAS-MWS system.

It is the objective of the work presented here, to provide the methodology on how to determine  $z_{ef}$  for a LAS-MWS system, for varying topography as well as for slanted beams. An important contrast between the LAS and MWS is that they have different path weighting functions, by which it might be expected that they have different effective heights, under given environmental conditions. The resulting methodology is applied, as a case study, to the

experimental setup used in a field experiment at Sheepdrove Organic Farm, Lambourn, Berkshire, UK, where a LAS-MWS system was installed.

This analysis provides guidelines for the selection of suitable LAS-MWS paths for future work over complex topography. For this purpose, analytical approximations for LAS and MWS path weighting functions were used, as well as a simple mathematical solution to calculate  $z_{ef}$ . Due to the complexity of the problem, the analysis is confined to idealised conditions, i.e. it assumed that the fluxes at the surface are constant over the footprint of the LAS-MWS. Moreover, a further simplification is introduced, that the LAS measures  $C_{T^2}$ , and that  $C_{Q^2}$  is determined solely by the MWS. The analysis is also limited to unstable conditions.

## **4.2 Structure Parameter Dependency on Height**

De Bruin found that Eq 2-34 can be rewritten as (Evans and de Bruin, 2009):

$$|H| = A(C_T^2)^{\frac{3}{4}} \sqrt{z(-L_{Ob} + c_{T^2}z)}$$

**Eq 4-1**

The constants  $\rho, c_p, k_v, g, c_{T1}$  and  $\bar{T}$  have been grouped together:

$$A = \rho c_p \left( \frac{k_v g}{c_{T1}^{3/2} \overline{T}} \right)^{1/2}$$

**Eq 4-2**

Assuming that the LAS measures the path-averaged ensemble mean of the temperature structure parameter,  $\langle C_{T^2} \rangle$ , defined as:

$$\langle C_{T^2} \rangle = \int_0^1 C_T^2(\gamma) G_{LAS}(\gamma) d\gamma$$

**Eq 4-3**

Recall that  $G_{LAS}(\gamma)$  (Eq 2-18) is the path weighting function for the LAS, and  $\gamma$  is the normalised position along the path. The scintillometer beam height at a point above the land surface is  $z(\gamma)$  (for simplicity the zero-plane displacement height is neglected).  $z_{eff}$  is the representative height of the LAS beam over the land surface, required to relate the LAS measured  $\langle C_{T^2} \rangle$  to  $H$ , and can be defined by:

$$|H| = A \langle C_{T^2} \rangle^{3/4} \sqrt{z_{eff} (-L_{Ob} + c_{T2} z_{eff})}$$

**Eq 4-4**

Normalising the path-averaged flux with the flux at the midpoint of the path given by Eq 4-1, and substituting Eq 4-4, yields the following expression for

$$z_{eff},$$

$$z_{efH}(-L_{Ob} + c_{T2}z_{efH}) = \left[ \frac{1}{\int_0^1 (z(\gamma)(-L_{Ob} + c_{T2}z(\gamma))^{-\frac{2}{3}} G_{LAS}(\gamma) d\gamma)} \right]^{\frac{3}{2}} = I_H(L_{Ob})$$

**Eq 4-5**

which has the quadratic solution,

$$z_{efH} = \frac{L_{Ob} - \sqrt{L_{Ob}^2 + 4c_{T2}I_H(L_{Ob})}}{2c_{T2}}$$

**Eq 4-6**

Following similar algebra,  $z_{efLE}$ , the effective height required to calculate  $L_vE$ , from the LAS-MWS, was derived using Eq 2-35. Recalling that  $G_{MWS}(\gamma)$  is the MWS path weighting function (Eq 2-17), then the quadratic solution is:

$$z_{efLE} = \frac{L_{Ob} - \sqrt{L_{Ob}^2 + 4c_{T2}I_{LE}(L_{Ob})}}{2c_{T2}}$$

**Eq 4-7**

$$I_{LE}(L_{Ob}) = \frac{1}{\int_0^1 (z(\gamma)(-L_{Ob} + c_{T2}z(\gamma))^{-\frac{2}{3}} G_{MWS}(\gamma) d\gamma)} \sqrt{\frac{1}{\int_0^1 (z(\gamma)(-L_{Ob} + c_{T2}z(\gamma))^{-\frac{2}{3}} G_{LAS}(\gamma) d\gamma)}}$$

**Eq 4-8**

These provide new, elegant and exact analytical solutions for  $z_{efH}$  and  $z_{efLE}$  which can be directly computed, thus the method is simpler to apply than the earlier work of Hartogensis et al. (2003), which required iteration to reach a

full solution, and in any case only considered  $z_{efH}$ . It is recognised here that the  $z_{efH}$  and  $z_{efLE}$  have different forms.

### **4.3 Approximate Path Weighting Functions for the LAS and MWS**

The following approximations were found by De Bruin, and are computationally more convenient than the exact forms (Evans and de Bruin, 2009):

$$G_{LAS}(\gamma) \approx 2.163 \left( \frac{2J_1(2.283\pi(\gamma-0.5))}{2.283\pi(\gamma-0.5)} \right)^2$$

**Eq 4-9**

$$G_{MWS}(\gamma) \approx \frac{[\gamma(1-\gamma)]^{\frac{5}{6}}}{\int_0^1 [\gamma(1-\gamma)]^{\frac{5}{6}} d\gamma}$$

**Eq 4-10**

These close approximations are used in the next section, where these findings are applied to various cases of scintillometer installation, both for simple and complex topography.

## 4.4 Results of the Effective Height Calculations

### 4.4.1 Flat Topography and Slanted Paths

First, the new formulas were tested with flat topography, and the scintillometer beams parallel to the land surface, i.e.  $z(\gamma) = 20 \text{ m}$  for all  $\gamma$ . It was found that, for this parallel case,  $z_{efH} = z_{efLE} = 20 \text{ m}$ , as expected.

Secondly, a slanted path over flat topography was tested, with  $z(1) - z(0) = 24 \text{ m}$  and mean height  $\langle z \rangle = 20 \text{ m}$ . It was found that  $z_{efH}$  ranged from  $19.66 \text{ m}$  to  $19.76 \text{ m}$ , and  $z_{efLE}$  from  $19.47 \text{ m}$  to  $19.62 \text{ m}$ , as  $L_{Ob}$  went from  $-0.1 \text{ m}$  to  $-10000 \text{ m}$ .

### 4.4.2 A Case Study over Complex Topography at Sheepdrove Organic Farm

Figure 4-1 shows the simplified land surface vertical profile (topography) for the 2.4 km LAS-MWS path installed at Sheepdrove Organic Farm from November 2005 to May 2007, with  $\langle z \rangle = 27.76 \text{ m}$ . Sheepdrove has mixed topography, with some large gradients, and the transceivers are mounted very close to the ground (at a height of about  $1.5 \text{ m}$ ). The sensitivities plotted are the path weighting functions multiplied by the structure parameter height dependency for free convection conditions (i.e.  $G(\gamma).z(\gamma)^{-4/3}$ , for both LAS and

MWS), thus indicating the contribution of each point along the path to the measured  $C_{n^2}$ . It was found that  $z_{eff}$  varied from 31.51 m to 32.61 m, and  $z_{effLE}$  varied from 27.20 m to 29.41 m, whilst  $L_{Ob}$  went from -0.1 m to -10000 m.

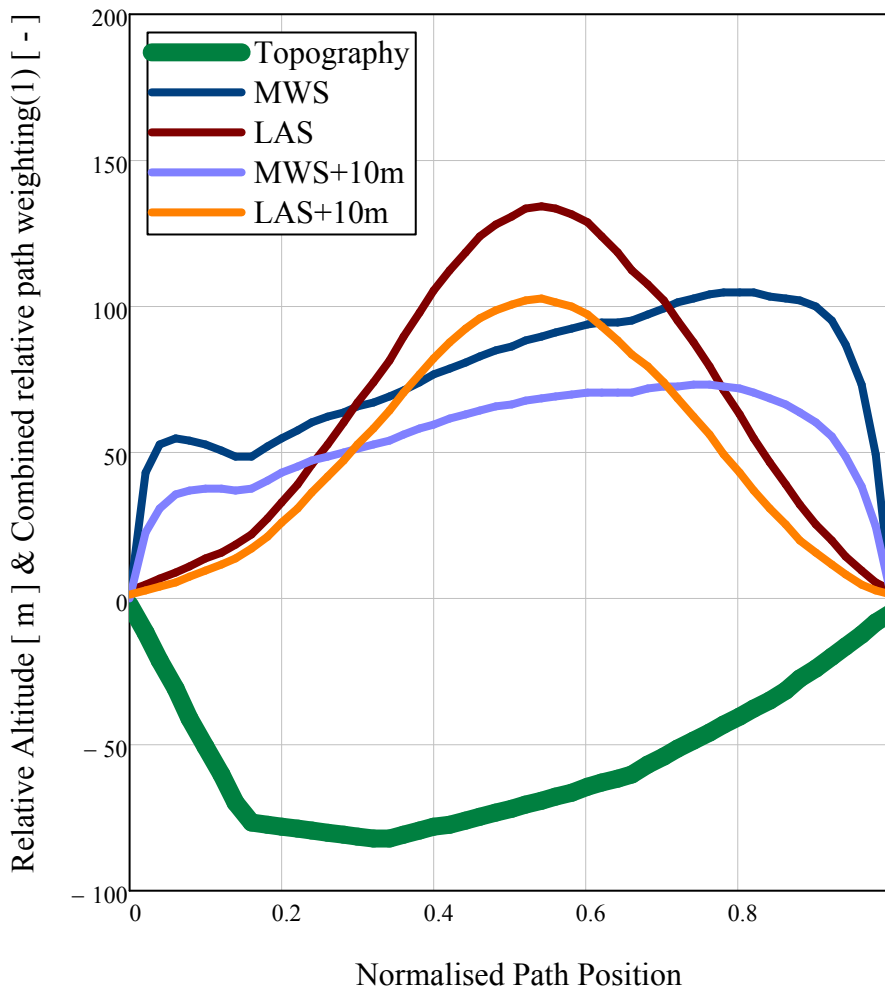


**Figure 4-1 Sensitivities to structure parameters for the Sheepdrove Organic Farm scintillometer path (refer to text for full explanation). (1) The ‘Combined relative path weighting’ is defined here as  $G(\gamma).z(\gamma)^{-4/3}$  i.e. the path weighting function multiplied by the dependence of  $C_{n^2}$  on  $z$ , for free convection conditions.**

## **4.5 The Effective Height Scaling of $C_{n^2\_LAS}$ for the**

### **Calculation of $C_{Q^2}$**

The analysis of section 4.2, showed the dependence of  $C_{T^2}$  on height. In order to derive  $z_{eLE}$ , the simplification was made that  $C_{Q^2}$  could be calculated directly from the MWS measurement. That simplification is now addressed, since it may introduce a significant error into the calculation of  $L_vE$ . There is no wavelength at which  $C_{n^2\_MWS}$  is independent of  $C_{T^2}$ , therefore we employ Eq 2-28 to calculate  $C_{Q^2}$ . This calculation requires  $C_{n^2\_LAS}$ , and implies that  $C_{n^2\_MWS}$  and  $C_{n^2\_LAS}$  are both measured at exactly the same height, as they are each strongly dependent on the measurement height. As was found in the previous sections, due to the different path weighting functions of the scintillometers,  $C_{n^2\_MWS}$  and  $C_{n^2\_LAS}$  are not measured at the same height over complex terrain or with slanted paths.

To analyse the effect on the calculation of  $C_{Q^2}$ , we first note that the dependence of  $C_{T^2}$  on  $C_{Q^2}$  may be circumvented by using Eq. 2-27, where the Bowen ratio is used instead of  $C_{Q^2}$ . It is then clear that with the Bowen ratio approximation:

$$C_{T^2} \propto C_{n^2\_LAS}$$

and therefore the same  $z_{efH}$  given by Eq 4-6 is also the effective height of the measurement of  $C_{n^2\_LAS}$ . Similarly, it is assumed as a first approximation, that  $C_{n^2\_MWS}$  is measured at  $z_{efLE}$ .

$C_{n^2\_LAS}$  must be scaled from its spatial mean measured value,  $\langle C_{n^2\_LAS} \rangle_{z_{efH}}$ , to the expected value at  $z_{efLE}$ ,  $\langle C_{n^2\_LAS} \rangle_{z_{efLE}}$ , using the appropriate scaling factor. This has been derived here, for the first time, by substituting Eq 2.27 into Eq 4-4, at each height, and dividing the two expressions to define the stability dependent height scaling factor:

$$J_{LAS} = \frac{\langle C_{n^2\_LAS} \rangle_{z_{LE}}}{\langle C_{n^2\_LAS} \rangle_{z_H}} = \left[ \frac{\sqrt{z_{efLE}(-L_{Ob} + c_{T2}z_{efLE})}}{\sqrt{z_{efH}(-L_{Ob} + c_{T2}z_{efH})}} \right]^{-4/3}$$

**Eq 4-11**

#### 4.5.1 The Calculated Values of $C_{n^2\_LAS}$ Scaling Factor ( $J_{LAS}$ )

It was found that  $J_{LAS}$  ranged between 1.217 to 1.073, as  $z_{efH}$  varied from 31.51 m to 32.61 m, and correspondingly  $z_{efLE}$  varied from 27.20 m to 29.41 m, for  $L_{Ob}$  from  $-0.1$  m to  $-10000$  m, respectively.

This shows that it is crucial to account for the difference in  $z_{efH}$  and  $z_{efLE}$ , by correctly scaling  $C_{n^2\_LAS}$  before using it to calculate  $C_{Q^2}$ ; failure to do so will lead to over-estimates of  $C_{Q^2}$  of the order of 4 to 11 % (assuming that  $C_{n^2\_LAS}$  accounts for around 50 % of the measured  $C_{n^2\_MWS}$ ). It is thought that  $J_{LAS}$

has not been applied before in the calculation of  $L_v E$ , using two-wavelength scintillometry with slanted paths and/or complex terrain. Furthermore, it appears to have been overlooked in all theoretical descriptions of the method. Here the magnitude of  $J_{LAS}$  may be over-estimated by the approximation that  $C_{n^2\_MWS}$  is measured at  $z_{efLE}$ , because of the different dependencies of these quantities on  $C_{T^2}$ ; this requires further analysis.

#### **4.6 Discussion of $z_{efH}$ and $z_{efLE}$**

The new effective height equations presented, and the simplified path weighting functions give the expected constant beam height over flat topography that is invariant with  $L_{Ob}$ , which is consistent with earlier work. The example slanted path shows a very small dependence on  $L_{Ob}$  of about 0.5 %, which can be neglected in most practical applications. For the same path however, it was found that  $z_{efLE}$  is about 1 % lower than  $z_{efH}$ . As has been shown in Figure 4-1, this is due to the MWS having a greater path weighting, relative to that of the LAS, for the two end quarters of the path, combined with the dependency on  $z(\gamma)$  (which tends to  $z^{-4/3}$  for the free convection limit). This height dependency is crucial in understanding the effective heights: as shown here, even slanted paths (which have linearly varying  $z(\gamma)$ ) can lead to disparity in  $z_{efH}$  and  $z_{efLE}$ , due to the non-linear dependency on the absolute value of  $z(\gamma)$ . With correctly calculated effective heights, the fluxes can be accurately determined. However, the effective height disparity is indicative of the mis-match of the path weighting functions, and it must be recognised that

the LAS and MWS do not sample entirely the same turbulence structures along the same path, even with ideal parallel scintillometer beams.

The results of the properly determined  $z_{efH}$  and  $z_{efLE}$ , for the Sheepdrove case show that large differences (10 %) can occur in these values, over complex topography. Whilst the relative topographic changes are important, it is the interplay of path sections with very low  $Z$  and the path weighting functions which critically determine (a) the difference in effective height for each flux, and (b) the degree of variation with  $L_{Ob}$ . Note that by increasing the absolute height of the beams by employing small masts at the transceivers (e.g. 10 m high), the relative difference in the effective heights would be reduced, and there would be much better spatial coincidence of the contributions to the structure parameters along the path i.e. the scintillometers would be more closely sampling the same turbulence structures. The effect of this is shown in Figure 4-1.

The idealised cases presented here demonstrate the need to carefully calculate the respective effective heights. In real applications, the two-wavelength method should also apply the appropriate scaling with height of  $C_{T^2}$  measured by the LAS to the relevant height of the MWS, as required to calculate  $C_{Q^2}$ . The analysis presented here shows that the scaling factor  $J_{LAS}$  could be quite large (of the order of 10 % for Sheepdrove) – and that its omission would lead to an over-estimation of  $L_v E$ . It has been observed that temperature and humidity fluctuations are often not perfectly correlated (Lüdi et al., 2005), as has been assumed here.

This new analysis leads to a comment on the results of the two-wavelength method used in LITFASS-2003. The published path topography is moderately varying and the transceiver mounting heights form a slanted path (Meijninger et al., 2006). Although some account of topography and the different path weighting functions of the LAS and MWS was made (*pers. comm.*), it may not have been fully considered in the manner presented, possibly resulting in a small over-calculation of  $L_v E$  (perhaps up to about 5 %). If this were the case, then this would to some degree reduce the reported systematic bias towards higher  $L_v E$  compared with eddy covariance measurements.

New formulae for the effective heights that are required to calculate sensible and latent heat fluxes from the LAS and the LAS-MWS combination have been derived. It has been shown, for the first time, that these effective heights ( $z_{efH}$  and  $z_{efLE}$ ) have different derivations and formulations, based on MOST scaling of the structure parameters and the inclusion of the different path weighting functions of the two scintillometers. For typical LAS-MWS measurement paths which are often slanted with respect to the land surface, and may also be over complex topography, we find significant differences in  $z_{efH}$  and  $z_{efLE}$ . In such cases, the equations given here for  $z_{efH}$  and  $z_{efLE}$  must be used to correctly compute  $L_v E$ .

The solutions shown here for the effective heights are complete and exact, compared to earlier work which required either approximation or iteration.

It is suggested that when applying the LAS-MWS system over complex topography that sufficient absolute height of the scintillometer beams is established for the whole path length to reduce the significance of the non-

linear scintillation contributions when the beam is closer to the ground. This has the dual effects of reducing the relative difference in  $z_{eff}$  and  $z_{effLE}$ , and also better matching the sampled turbulence along the path for the two scintillometers.

# Chapter 5    Sensible and Latent Heat Flux Measurements over Complex Terrain by Two- wavelength Scintillometry

## 5.1 Introduction

The sensible heat flux ( $H$ ) from path lengths of up to 5 km can be averaged by the LAS, representing, for typical atmospheric stability and moderate beam height, a source area of up to about 4 km<sup>2</sup> (Kohsiek et al., 2002; Meijninger et al., 2002b). This application, over complex terrain, has been tested in Chapter 3. The wavelength of the LAS is in the near-infrared and is primarily sensitive to refractive index changes caused by temperature; it measures the path-averaged temperature structure parameter ( $C_{T^2}$ ). A second scintillometer, termed a Millimetre-Wave Scintillometer (MWS) can be combined with the LAS to measure the humidity structure parameter ( $C_{Q^2}$ ) (Kohsiek and Herben, 1983), for which optimal wavelength combinations were given by Andreas (1989). Combined LAS-MWS systems measuring both  $C_{T^2}$  and  $C_{Q^2}$  have occasionally been used to measure large area averages of  $H_{LAS}$  and  $L_v E_{MWS}$  over flat landscapes, sometimes with mixed vegetation (Green et al., 2000; Green et al., 2001; Kohsiek and Herben, 1983; Meijninger et al., 2002b). The

technique was extended to moderately heterogeneous terrain – with mixed vegetation and gently changing topography – in the LITFASS-2003 experiment (Meijninger et al., 2006), which showed reasonable agreement with EC fluxes.

In terms of experimental setup and logistics, the addition of the MWS to the LAS is straight-forward, as the transceivers are installed alongside one-another. The direct measurement of areal-averaged  $L_v E_{MWS}$  as well as  $H_{LAS}$  is an important goal, which would avoid the potentially large errors of indirect methods. For example, the standalone operation of the LAS to measure  $H_{LAS}$  requires both  $R_n$  and  $G$  to calculate  $L_v E$  as the residual of the surface energy balance; apart from the errors in these measurements, there is no practical method to upscale these measurements to represent the LAS source area (SA), without installing many in-field replicates, which is both expensive and inconvenient. The few experiments conducted with LAS-MWS systems reflect the high cost and specialised millimetre-wave electronics technical expertise required to build and repair the MWS. In comparison, the LAS is about half the cost of the MWS, and in recent years has become commercially available. As a precursor to the experimental work presented here, a suitable MWS had to be specified and built – this is described in the next section.

The LAS-MWS system was deployed at Sheepdrove Organic Farm, in order to investigate the application of two-wavelength scintillometry over complex terrain. The Sheepdrove 2004 Experiment (Chapter 3 of this thesis) had already validated the LAS measurements over the same scintillometer path (albeit with different agricultural land use at that time). The aim of the experiment described in this chapter (hereafter referred to as Sheepdrove 2006) was to apply two-wavelength scintillometry over complex terrain, to

measure area-averaged  $H_{LAS}$  and  $L_v E_{MWS}$ , and to compare them with the available land surface energy ( $R_n - G$ ), with the assumption that good energy balance closure of 30-minute mean data indicates accurate scintillometer fluxes. Comparison with aggregated EC measurements, or any other independent ground-truth data, is not made. This simplified approach greatly reduces the experimental resource requirements.

The performance of the new MWS built for this experiment is investigated by spectral analysis of its raw high frequency scintillation measurement, in order to test its measurement of the inertial sub-range of the turbulence spectrum (Clifford, 1971). Spectral analysis of the MWS also reveals the appropriate frequencies for filter cut-offs to apply to the scintillation signal, in particular, to avoid (as far as possible) water vapour absorption contributing to the scintillation intensity.

The theory presented in Chapter 2 is applied to calculate  $H_{LAS}$  and  $L_v E_{MWS}$  for the first time from the new LAS-MWS combination. Furthermore, the important developments in recognising the different effective heights of the LAS and the MWS, over complex topography, are applied in the data processing, according to the new derivations developed in Chapter 4. The results are presented, with notes of observed current limitations and some guidance for future operation of LAS-MWS systems.

## 5.2 Design Specification of the MWS

The most defining characteristic of the MWS is the choice of  $\lambda_{MWS}$ . There are at least three critical criteria that this specification must satisfy: (a) it should have high sensitivity to the humidity structure parameter ( $C_{Q^2}$ ) and relatively low sensitivity to the temperature structure parameter ( $C_{T^2}$ ); (b) it should have low water vapour absorption; and (c) it should have length scale sensitivity appropriate to the turbulent spectrum being measured. The other main considerations are: (d) the cost of components for a particular  $\lambda_{MWS}$ ; and (e) that  $\lambda_{MWS}$  must be permitted for operation by licence or otherwise, by the relevant radio communications authority.

Research into criterion (a) has been reported in the literature (Andreas, 1989), and since successful experimental work has been conducted at  $\lambda_{MWS} = 11$  mm (Green et al., 2001) and at  $\lambda_{MWS} = 3.2$  mm (Lüdi, 2002; Sarma and Hill, 1988) these wavelengths were the primary choices for the new design specification. The former has less sensitivity to scintillation ( $\propto \lambda_{MWS}^{7/6}$ ), and higher water vapour absorption, but lower cost. At  $\lambda_{MWS} = 3.2$  mm there is much less general demand for electronic sub-systems and components used in this system, therefore these are consequently much more expensive – they also tend to be less robust with shorter operating lifetimes.

According to the theory presented in Chapter 2, for a pathlength of, say, 2 km, the Fresnel zone ( $F$ ) is 2 - 5 m (depending on the wavelength) which is much

larger than the aperture size of the transmitter and receiver (that employ practical antenna diameters ( $D$ ) of the order of 0.2 - 0.30 m). Consequently,  $F > D$ , and therefore the MWS transmitter can be considered as a point source, and thus the MWS is treated in the theory as a Small Aperture Scintillometer (SAS – not to be confused with the commonly used short-path optical laser scintillometer, which is also classed as a SAS).

The SAS is most sensitive to turbulence of length scale of the order of the first Fresnel zone ( $F = \sqrt{\lambda_{MWS} L}$ , where  $L$  is the scintillometer pathlength). Scintillation measurements must be made in the inertial sub-range of turbulence, where Kolmogorov's Law holds, to allow calculation of heat fluxes, i.e.  $l_0 \ll F \ll L_0$  (where  $l_0$  and  $L_0$  are respectively the inner and outer length scales of the turbulence). Under certain application conditions,  $F$  may be fairly close to  $L_0$ , leading to invalid and erroneous measurements. Mainly for reasons of cost, it is preferred to work at longer wavelengths, but this increases  $F$ , towards  $L_0$ . For example at  $\lambda_{MWS} = 11$  mm and  $L = 2.43$  km,  $F = 5.2$  m. A crude estimate of  $L_0$  is to equate it to the measurement height. This implies that for this example, to maintain  $l_0 \ll F \ll L_0$ , a measurement height of approximately 20 m might be appropriate. By comparison, at  $\lambda_{MWS} = 3.2$  mm,  $F$  is nearly halved and this places a less restrictive condition on the measurement height.

Contamination of the scintillation signal by water vapour absorption is highly undesirable, but may be unavoidable to some degree. It is important that there is a method employed to separate absorption effects from scintillation. The simplest technique is separation in the frequency domain – very slow trends in water vapour concentration (of the order of minutes) can be easily

filtered out, but there will remain absorption variations at the turbulent frequencies that the scintillometer measures. Path-averaging of the absorption fluctuations at higher frequencies is expected to reduce them to a negligible level. It is also noted that for longer pathlengths any residual effect of absorption is reduced relative to the scintillation signal, because the absorption strength is proportional to  $L$ , whilst scintillation strength increases with  $L^{11/6}$ .

To best meet the above criteria,  $\lambda_{MWS} = 3.2$  mm (94 GHz frequency) was selected. To ensure a very high signal-to-noise-ratio (SNR) of the MWS receiver, it was phase-locked with the transmitter, using a Global Positioning System (GPS), reference signal, with standard GPS receivers fitted to both the transmitter and receiver. This achieved high accuracy, whilst having very low power consumption compared with older technologies (e.g. temperature stabilisation of reference oscillators). Overall the system SNR had a design budget of  $> 95$  dB. The power consumption was around 12 W for the receiver and 8 W for the transmitter – this was sufficiently low to operate the instrument from solar power, with automatic shutdown at night-time. Both the transmitter and receiver antennas had diameters of 300 mm. The detailed design and build of the MWS was carried out by the Radio Communications Research Unit of the Rutherford Appleton Laboratory.

The MWS was logged on a purpose-built datalogger using a low-power computer module (model TDS2020, Triangle Digital Services, Thirsk, UK) programmed using the Forth language. The datalogger was programmed to sample and log both the LAS and MWS at 80 Hz – to enable both spectral analyses and the cross-correlation of the two signals (i.e. the application of Bichromatic Scintillometry).

### **5.3 Measurements and Methods**

The Sheepdrove 2006 experiment utilised the same field site as described in Chapter 3 (see 3.2.1 *et. seq.*) – and the same LAS path. The MWS transmitter and receiver were installed, immediately adjacent to the LAS transmitter and receiver respectively, with a separation of approximately 0.5 m between centres (Figure 5-1). The mountings were close to the ground to reduce the wind loading, which may cause vibrations that will contribute noise to the scintillation signals; to minimise the magnitude of any vibrations, the mountings were made very stiff and rigid, using square section steel posts. The aim of this experiment was to test the performance of the LAS-MWS scintillometer combination, using the two-wavelength method (2.4.2) to measure the landscape-scale latent heat flux.

With the same setup that had been operating continuously since 2004, ten-minute means of the LAS measured near-infra-red turbulent structure parameter ( $C_n^2$ ) and the mean signal intensity were recorded on a CR10 data logger (Campbell Scientific Ltd.). The MWS was sampled at 80 Hz, and all samples stored on the MWS logger (refer to Section 5.2) as well the mean value and diagnostic data (battery voltage, instrument temperature and phase-locked-loop alarm). It was intended that the LAS would also be logged in the same way, to enable calculation of the temperature-humidity correlation coefficient ( $r_{TQ}$ , refer to 2.4.3) but this was prevented by a technical failure.



**Figure 5-1 The Kipp and Zonen LAS 150 (left) and the CEH-RAL MWS (right) – the LAS-MWS two-wavelength scintillometer system. Shown is the receiver site at Stancombe Reservoir.**

The number of in-field measurements for the Sheepdrove 2006 experiment was reduced compared with 2004. Figure 5-2 shows the weather station (WS) and Grass Pasture (GP), which measured the surface energy balance components with the exception of the latent heat, which was calculated as the residual of the energy balance for GP. Additionally a sonic anemometer (model R3, Gill Instruments Ltd.), an NRLite net radiometer (Kipp and Zonen B.V.) and a soil heat flux plate at 10 mm depth (Model 610, C. W. Thornthwaite Associates) were installed in a field with sparse small trees (around 3.5 m high) and conservation grassland/shrub under-storey; this site is named Melville's Trees (MT). The sensible heat flux measurements ( $H_{EC}$ ) were made at MT by eddy covariance from raw data stored on the CEH logger, at a height of 4.5 m above the ground.

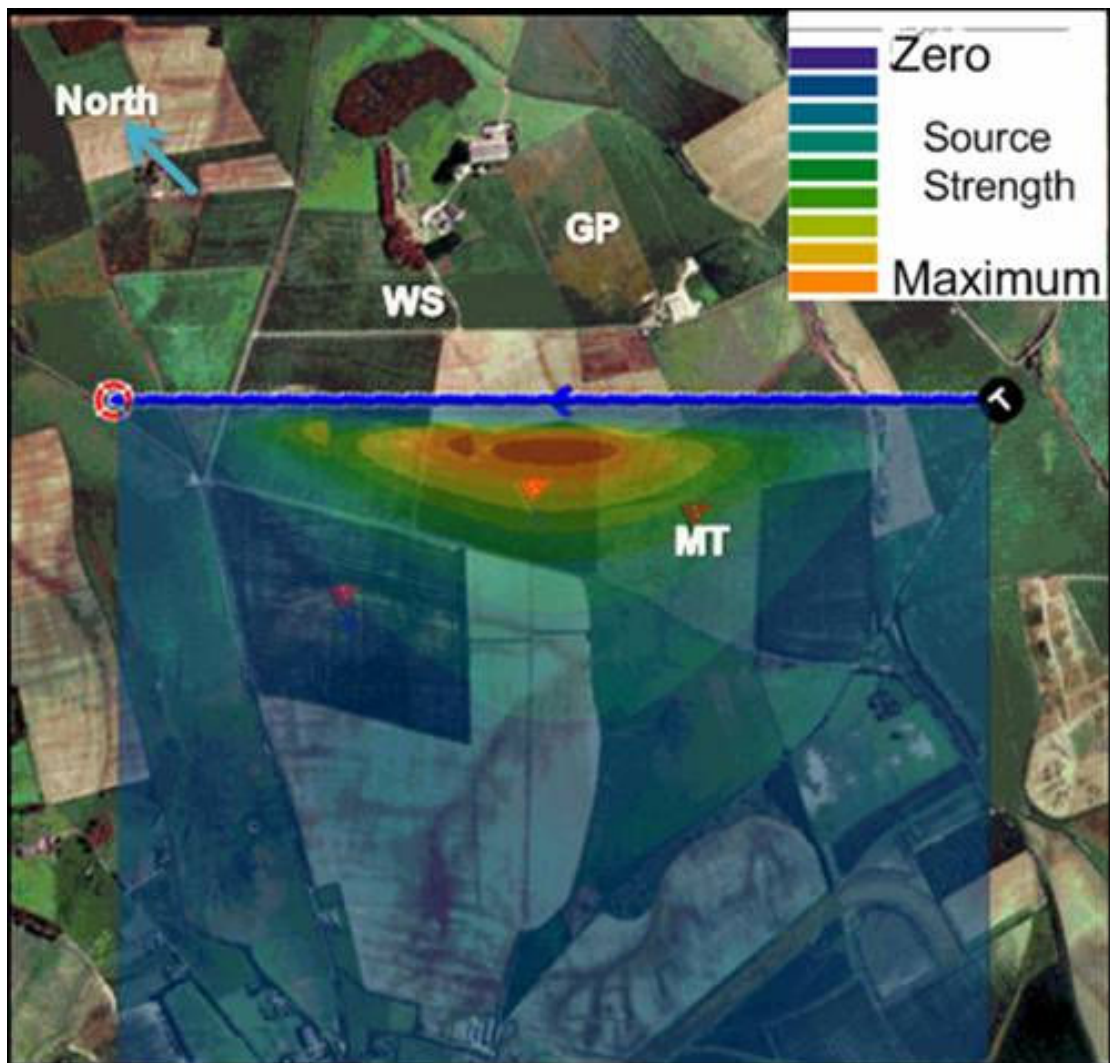


**Figure 5-2 Photograph (pre-2003), with overlay of typical LAS source area to SW of path (blue line), weather station (WS), grass pasture (GP) and Melville's Trees (MT) EC stations.**

The MWS raw data were band-pass filtered (BPF) with a pass-band between 0.05 and 10 Hz. The low-frequency cut-off was selected to remove signal variations due to changes in water vapour absorption, whilst the high-frequency cut-off rejected a small noise spike in the MWS spectrum above about 15 Hz. A very sharp cut-off Chebyshev type two (flat in the pass-band) digital filter was designed for this purpose, using Matlab software (The

MathWorks Inc.). After the BPF, 10-minute linear block means were calculated which were used to normalise the signal over each 10-minute period. Values of  $\sigma_{\chi}^2$  were then calculated as the variance of the logarithm of the normalised signal intensity (Eq. 2-9). A calibration for the MWS detector was applied to scale the output signal to intensity. Finally,  $C_{n^2\_MWS}$  was obtained using Eq. 2-12.

Sample spectra from the MWS were computed using an ARMASA smoothing spectral analysis routine (Broersen and de Waele, 2006) running in the Octave programming environment (<http://www.octave.org>).

$C_{n^2\_MWS}$  and  $C_{n^2\_LAS}$  were combined with the weather station measurements of air temperature, barometric pressure, wind speed and relative humidity (RH).  $u_*$  was calculated iteratively using an estimated roughness length ( $z_0$ ) of 0.02 m, much shorter than was used in the 2004 experiment, reflecting the lack of tall crops in the source area during the 2006 experiment.  $H_{LAS}$  and  $L_v E_{MWS}$  were then calculated by iteration using 'ScinPro' written in the R language (R, 2008). The theory of these calculations is presented in Sections 2.4.2 and 2.5. The stability function of de Bruin et al. (1993) for unstable conditions was used (in keeping with the Sheepdrove 2004 experiment). Since no measurements of  $r_{TQ}$  were available from either scintillometry or EC, the data were processed with  $r_{TQ} = 0.8$ , the typical unstable value measured by Beyrich et al. (2005), for similar conditions.

The new formulae for the effective heights were applied using Eqs 4-6, 4-7 and 4-11. The required integral (Eq 4-8) for these equations makes it slow and cumbersome to re-compute the effective heights for each 10-minute data

point. Instead, sets of effective heights for the Sheepdrove topography and for a range of values of  $L_{Ob}$  were calculated using Mathcad and stored as look-up table file that was read by ScinPro.

Scintillometer fluxes were quality controlled by removing data if (a) there was precipitation or (b)  $(H_{LAS} + L_v E_{MWS}) > 3 * R_n$ . Test (b) was a convenient means of detecting unusual events when the scintillometer signal had been disturbed in some way, usually by farming activity. Data were restricted to unstable conditions between 06:00 UTC and 18:30 UTC. The EC data were processed as described in Appendix 1.

Figure 5-3 gives a visual impression of the typical topography below the scintillometers' path (the topographic profile is shown in Figure 3-5), and the mixture of bare soil and short vegetation that dominated the typical SA to the SW. It was estimated that, for SW winds, the typical SA comprised of 50% grass pasture, 35% spring wheat and 15% pig rearing.

## **5.4 Results**

The recorded data is first used to test the basic performance of the MWS in measuring scintillation spectra. The prevailing weather conditions during the experiment are presented and discussed. Next the surface energy balance closure is tested, comparing the scintillometer measured fluxes  $(H_{LAS} + L_v E_{MWS})$ , and available energy  $(R_n - G)$ , as measured by the point sensors; by this means the performance of the scintillometer flux

measurements are investigated in detail, with the analysis time-series of the energy balance components.



**Figure 5-3** The Sheepdrove Organic Farm scintillometer source area looking SW with the red line indicating the approximate path of the scintillometers' beams, on 02/06/2006. Pig houses ('arcs') are visible at top centre.

### **5.4.1 MWS Spectra**

The theoretical spectrum of the MWS was presented in Section 2.6.1, based on the theoretical derivation by Clifford (1971). In the absence of the effects of water vapour, the power spectral density (PSD) is expected to be constant with frequency up to some corner frequency ( $f_c$ ), and the PSD of this flat region of the spectrum scales with the measured  $C_n^2$ . The value of  $f_c$  is

proportional to the crosswind speed, but is not discussed further here. The decreasing part of the spectrum is expected to follow the Kolmogorov decay, with a power-law slope of  $-8/3$ .

Note that the first spectral analysis of these MWS data was done by Oscar Hartogensis and Arnould Moene, who discovered that there was an unexplained noise peak in the spectra at just above 10 Hz, with sometimes a second peak around 4-5 Hz.

Figure 5-4 to Figure 5-7 show the spectra measured by the MWS. The power spectral density plots obey the expected Clifford spectrum at both low and high wind speeds. The frequency spectrum reveals how well the digital filtering will reject the MWS noise, without affecting the desired turbulence scintillations. At high crosswind speeds the filter is well matched to the measured spectrum, and 9 to 10 Hz is the optimal high-frequency filter cut-off (Figure 5-5), in order to maximise the signal due to turbulence and minimise the noise contribution. At lower crosswind speeds the turbulence spectrum is shifted to lower frequencies as expected, and the MWS noise is also shifted to lower frequencies. The noise spike in Figure 5-7 is centred well below 10 Hz, so that it will not be rejected by the BPF and will instead contribute erroneously to the MWS signal; from the area under the noise spike at 4 to 5 Hz in the frequency spectrum (Figure 5-7), it can be seen that this noise spike contributes about 5 % to the total signal variance.

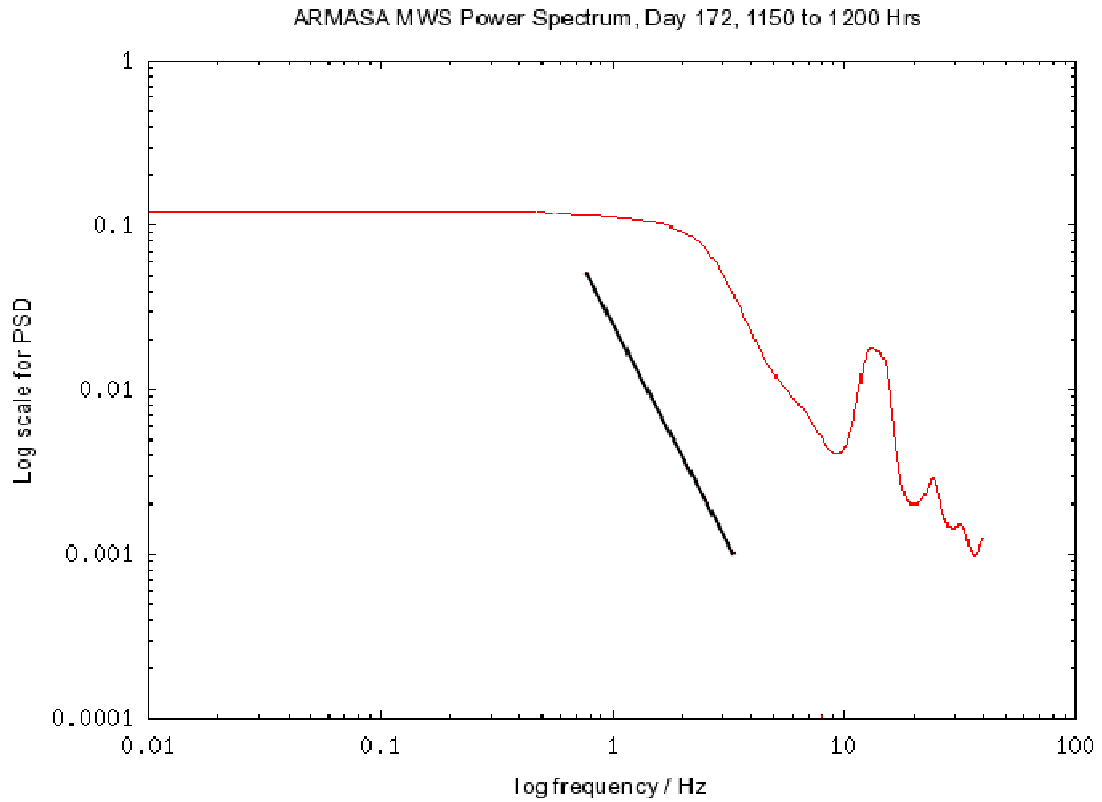


**Figure 5-4 Power spectral density (PSD) versus frequency for the unfiltered MWS receiver signal, compared with the expected Kolmogorov slope of  $-8/3$  (black line), with high crosswind speed ( $7.3 \text{ m s}^{-1}$ ).**

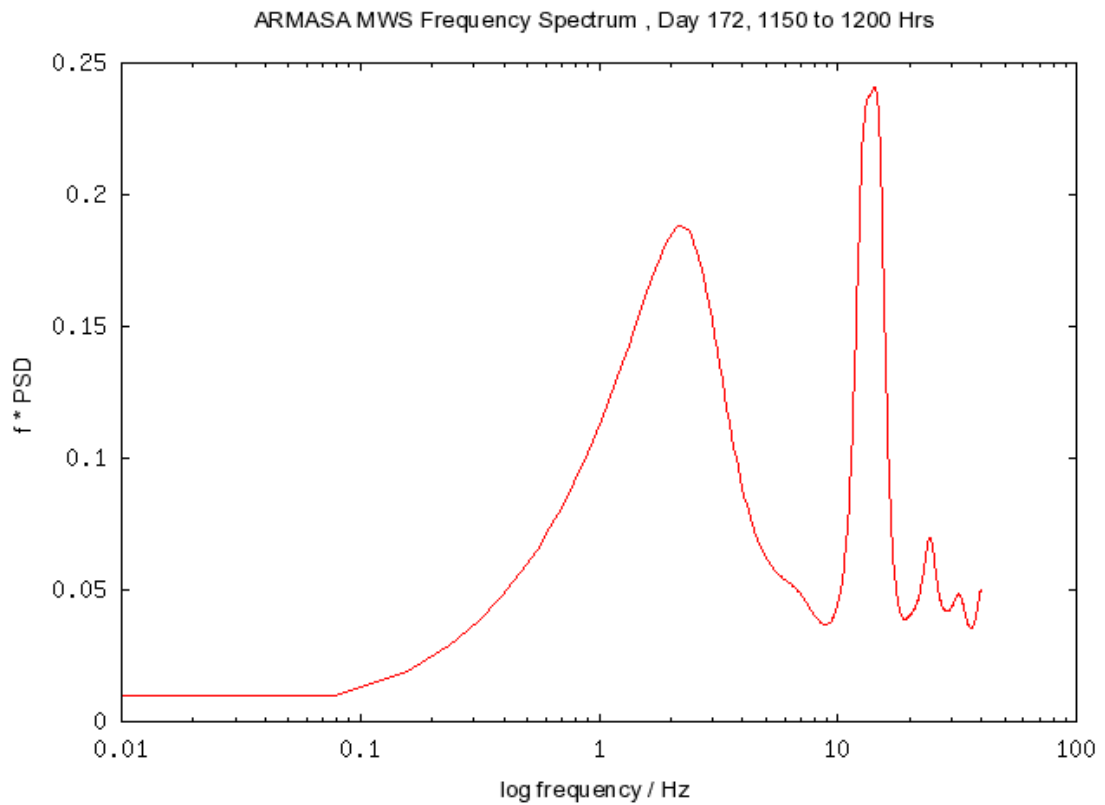


**Figure 5-5 MWS frequency ( $f$ ) spectrum for high crosswind speed ( $7.3 \text{ m s}^{-1}$ ), showing that most of the signal variance due to turbulence is between 0.1 and 10 Hz, with MWS noise evident between 10 and 20 Hz.**

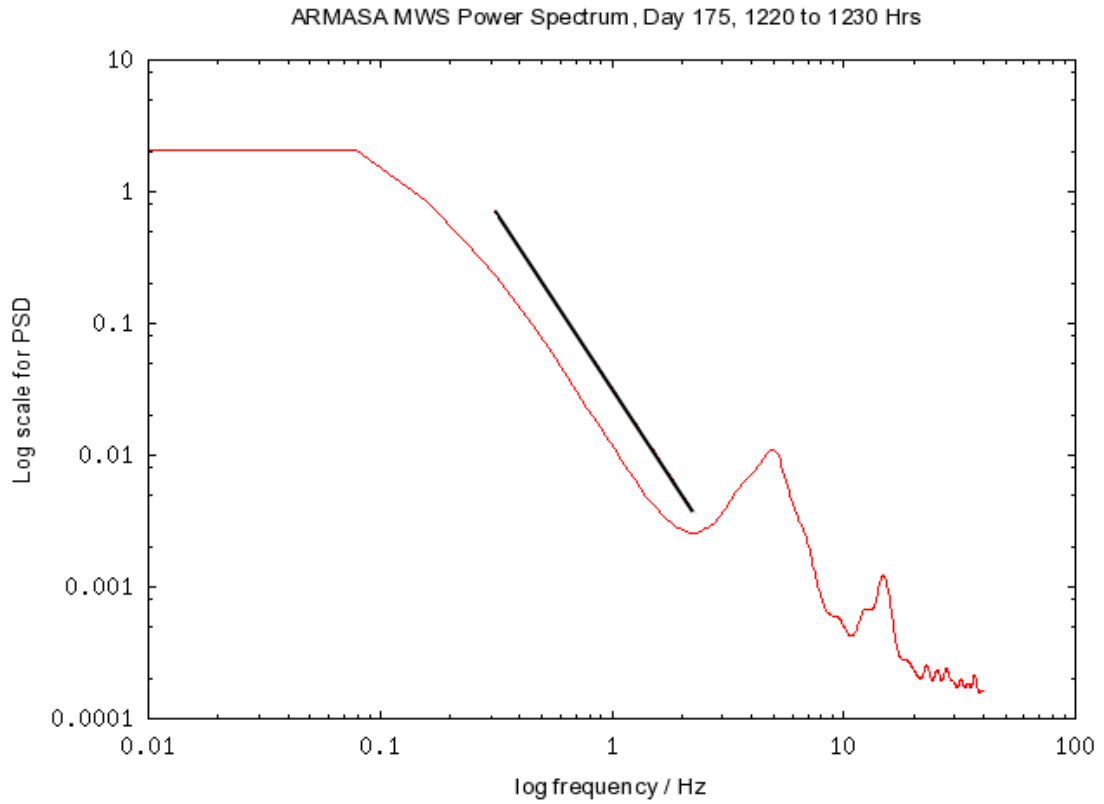


**Figure 5-6 Power spectral density versus frequency for the unfiltered MWS receiver signal, compared with the expected Kolmogorov slope of  $-8/3$  (black line), with low crosswind speed ( $1.1 \text{ m s}^{-1}$ ).**

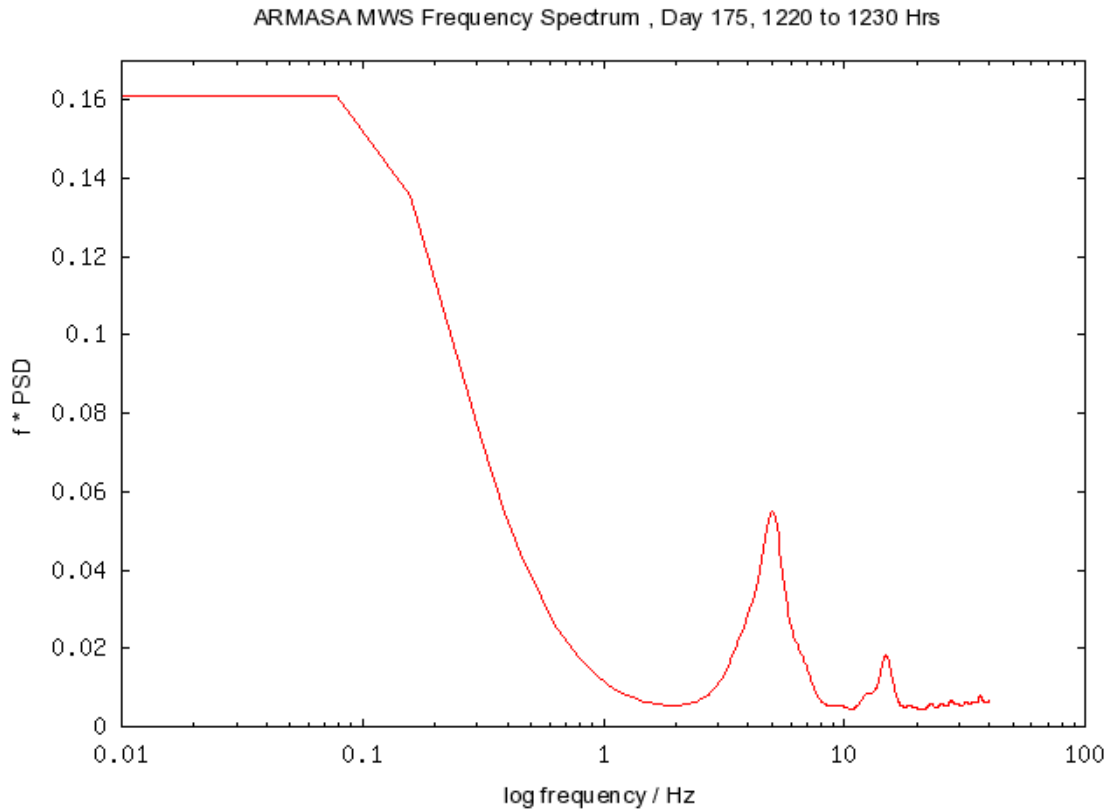


**Figure 5-7 The MWS frequency ( $f$ ) spectrum for low crosswind speed ( $1.1 \text{ m s}^{-1}$ ), showing that most of the signal variance which is due to turbulence is below 2 Hz. The MWS noise is evident between 2 - 10 Hz.**

### 5.4.2 Weather Conditions

Figure 5-8 shows the weather conditions during this experiment. There were two distinct sub-periods, with different prevailing weather: the first ten days were relatively cool, with low pressure, 12.6 mm of rain and moderate wind speeds ( $6 \text{ to } 8 \text{ m s}^{-1}$ ); the last week is dry and dominated by high pressure, with daytime temperatures steadily rising to maxima between  $25 \text{ and } 30 \text{ }^\circ\text{C}$  on the last three days, whilst wind speeds are low (mostly below  $3 \text{ m s}^{-1}$ ). For the first week the wind is from the south-west, thereafter the wind direction is more variable with periods of north-easterly and southerly winds. The diurnal variations in relative humidity are at high values (60 to 100 %) for the cool-wet

period, and the relative humidity does not drop much below 50 % until the last three days which were relatively hot and dry for the UK.

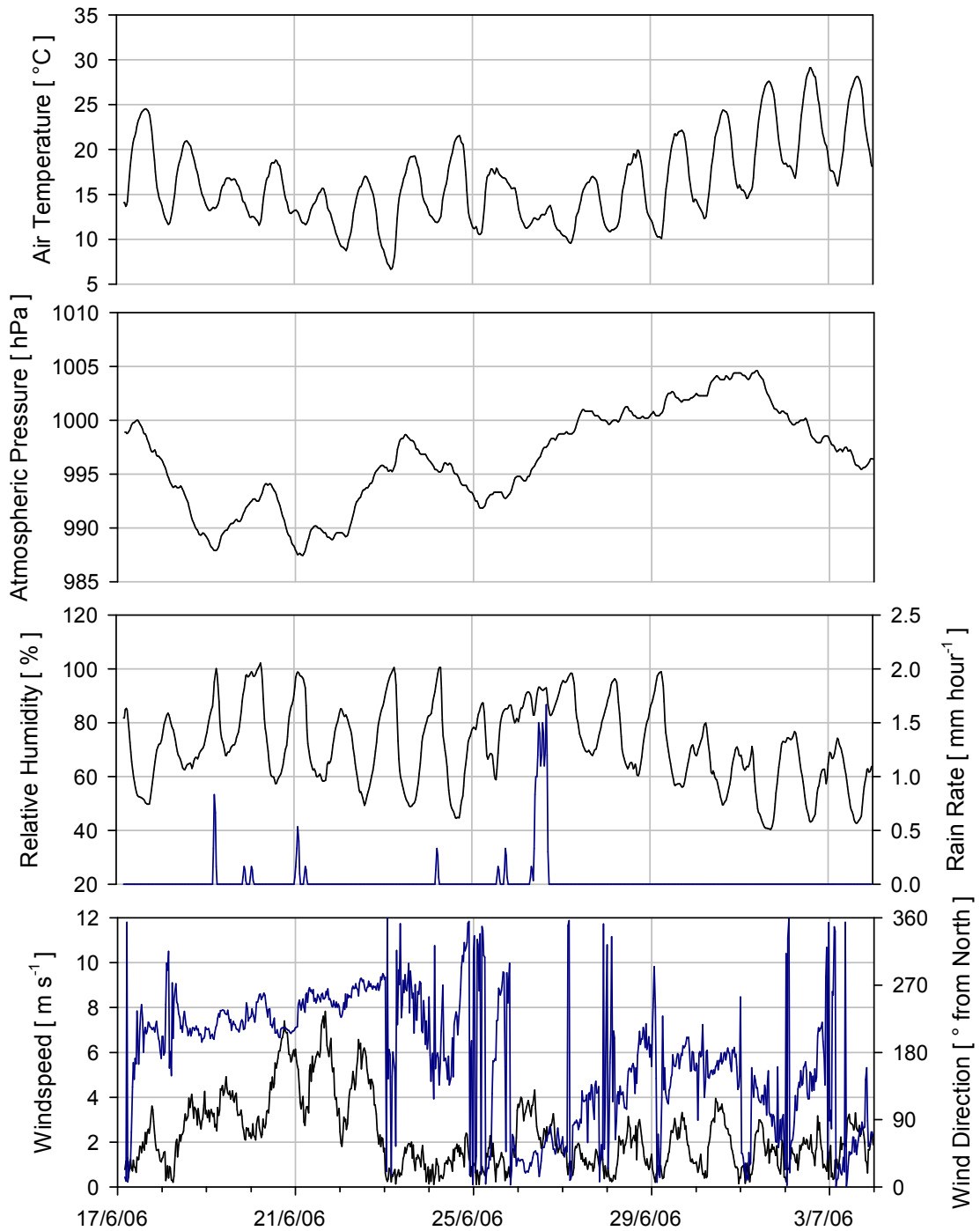


**Figure 5-8** The weather conditions during the Sheepdrove 2006 Two-wavelength Scintillometer Experiment. Rain rate and wind direction are indicated by blue lines.

### 5.4.3 Measured $C_{n^2\_LAS}$ and $C_{n^2\_MWS}$

$C_{n^2\_LAS}$  and  $C_{n^2\_MWS}$  and the mean LAS and MWS demodulated receiver signals are shown in Figure 5-10. All four plots show strong diurnal variation, as is expected, especially of the structure parameters. Immediately following the switch-on of the system at 04:00 UTC,  $C_{n^2\_MWS}$  drops to the lowest daily value (around  $5 \times 10^{-14} \text{ m}^{-2/3}$ ), then increases sharply to maxima around midday or early afternoon. The late afternoon decrease in  $C_{n^2\_MWS}$  is not fully captured before the MWS system powered-down at 20:00 UTC.

Measurements of  $C_{n^2\_LAS}$  range typically between  $4 \times 10^{-17}$  and  $2.5 \times 10^{-14} \text{ m}^{-2/3}$ . The mean daytime value of  $C_{n^2\_LAS}$ , used to calculate quality-controlled (QC) fluxes, was  $8.3 \times 10^{-15} \text{ m}^{-2/3}$ , and the maximum  $3.1 \times 10^{-14} \text{ m}^{-2/3}$  (higher values shown are due to precipitation). The corresponding mean  $C_{n^2\_MWS}$  was  $3.3 \times 10^{-13} \text{ m}^{-2/3}$ , with a maximum of  $4.1 \times 10^{-11} \text{ m}^{-2/3}$  and minimum of  $3.2 \times 10^{-14} \text{ m}^{-2/3}$ . Higher  $C_{n^2\_MWS}$  values, like  $C_{n^2\_LAS}$ , are also observed during rainfall events, and clearly, in both cases, these are invalid measurements, due to scattering by raindrops.

The typical diurnal cycles of the mean signals provides valuable quality control of the data – especially for the case of precipitation, mist or fog etc. This is clearly seen on 26<sup>th</sup> June when the LAS mean signal hardly increases from its night-time value. Note that there is relatively less attenuation of the mean MWS signal due to rain, compared with the LAS, so that it is simpler to

provide robust quality control by range-checking the LAS mean signal. The diurnal variation of the LAS mean signal shown here is very large indeed and may indicate an instrumental problem, such as moisture ingress.

Figure 5-9 shows the time series of the calculated  $C_{T^2}$  and  $C_{Q^2}$  values, which are of interest in their own right, but also provide quality-control information, as an intermediate step in determining the heat fluxes.

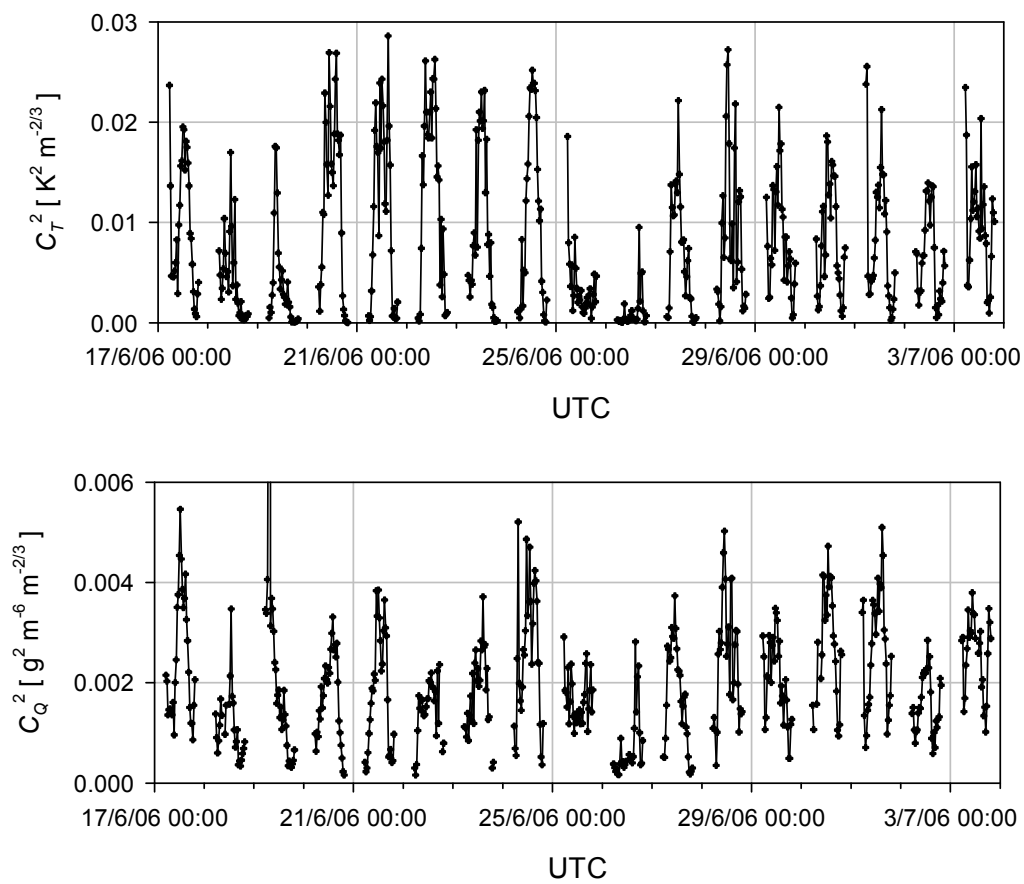


**Figure 5-9**  $C_{T^2}$  and  $C_{Q^2}$  measured by the LAS and LAS-MWS combination respectively.

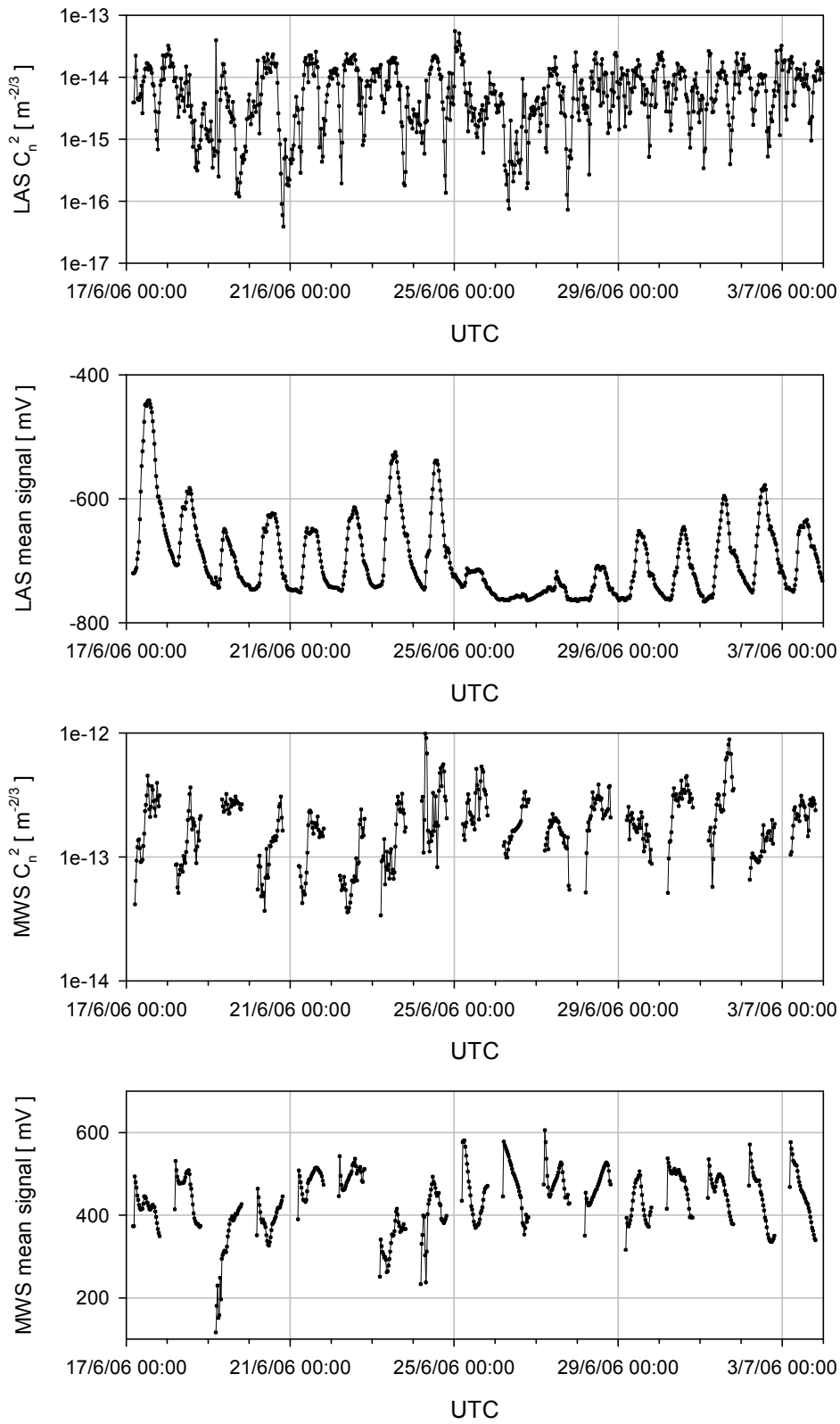


**Figure 5-10 Mean transmission and  $C_n^2$  time-series for the LAS and the MWS.**

#### 5.4.4 Sensible and Latent Heat Fluxes

The relative performance of the LAS can be checked by regression with the EC stations at GP and MT (Figure 5-11). Although the flux source areas are quite different, and contain different land cover types, there are strong correlations between the landscape scale LAS measurement and the field-scale EC measurements ( $r^2 = 0.79$  and  $0.82$  for GP and MP respectively), particularly for this short period of time, during which the vegetation has not changed greatly. The regression of  $H_{LAS}$  with  $H_{EC}$  for GP, shows that on average  $H_{LAS}$  is 65 % higher, which is reasonable and consistent with the results of the Sheepdrove 2004 experiment (Table 3-4), which showed that later in the year (when more of the crops in the LAS source area had senesced and were therefore transpiring less),  $H_{LAS}$  was over 100 % more than  $H_{EC}$  for GP. The MT site is not grazed, it is set aside as a conservation area, and the average latent heat flux is much smaller than that of GP, due to reduced transpiration; the regression for MT shows that  $H_{LAS}$  is on average 14 % higher than  $H_{EC}$  for MT.

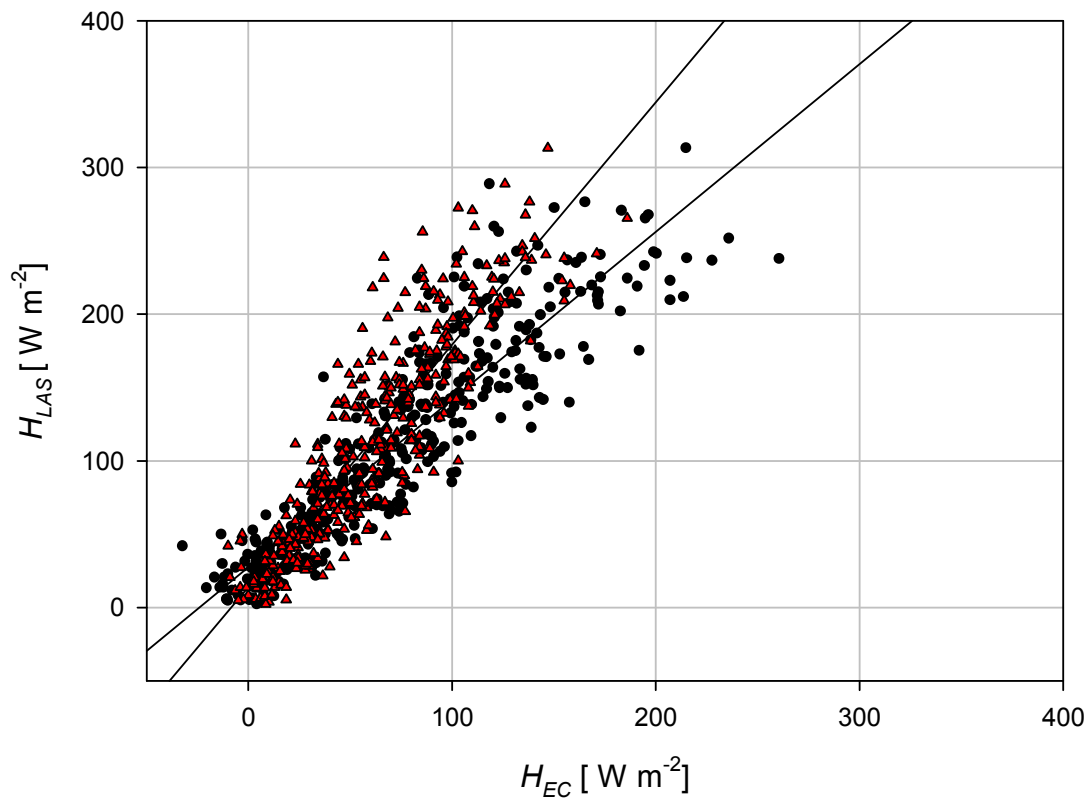


**Figure 5-11 Comparison of LAS with EC measured sensible heat flux, for Melville's Trees (black circles) and Grass Pasture (red triangles). There is a high correlation ( $r^2 = 0.82$ ), with a slope of 1.14 and offset of  $28 \text{ W m}^{-2}$  for Melville's Trees. For GP,  $r^2 = 0.79$  with a slope of 1.65 and offset of  $14 \text{ W m}^{-2}$ .**

The overall energy balance closure of  $(H_{LAS} + L_v E_{MWS})$  against  $(R_n - G)$  is shown in Figure 5-12, using  $R_n$  measured by the NRLite at GP and  $G$  also measured at GP. The data have been split into two chronological periods. The first period was cool, windy and sometimes wet, whilst the second was dry, hot and strongly convective. The  $r^2$  values are very close, but the energy balance closure is much less for the second period, with slope = 0.91, compared with on average perfect energy balance closure, slope = 1.00, for the first period.

The energy balance closure is shown as a time series in Figure 5-13 and Figure 5-14, where it is clearer that under some conditions the energy balance is almost exactly closed, whilst at other times, there are large under- or over-closures. The largest over-closures, when  $(H_{LAS} + L_v E_{MWS}) > 1.5 \times (R_n - G)$ , occur between 19<sup>th</sup> and 21<sup>st</sup> June 2006, following light rainfall, and sometimes at high wind speeds (around  $7 \text{ m s}^{-1}$  on 20<sup>th</sup> and 21<sup>st</sup> June). There are many days when the energy balance closure is consistently good throughout the day. Notable under-closure occurs in the second period, towards the end of the experiment on 1<sup>st</sup> and 2<sup>nd</sup> July 2006, when the weather is hot and dry, wind speeds are low, and from the south-east (along the line of the scintillometer path).

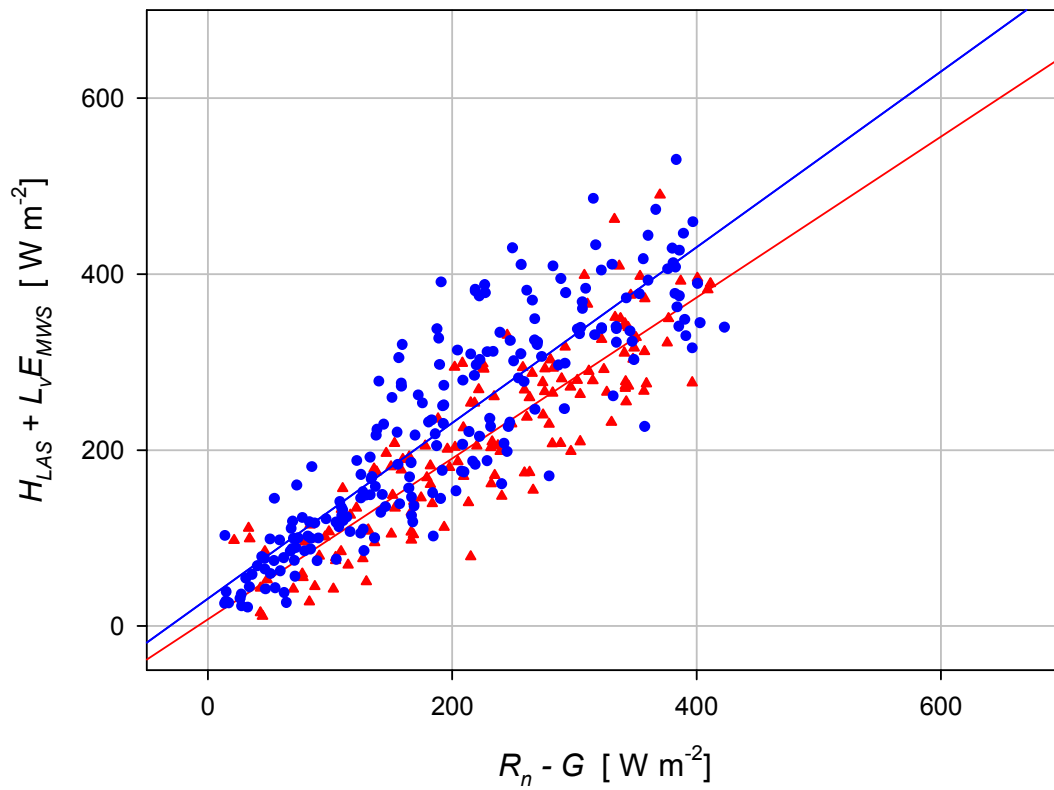
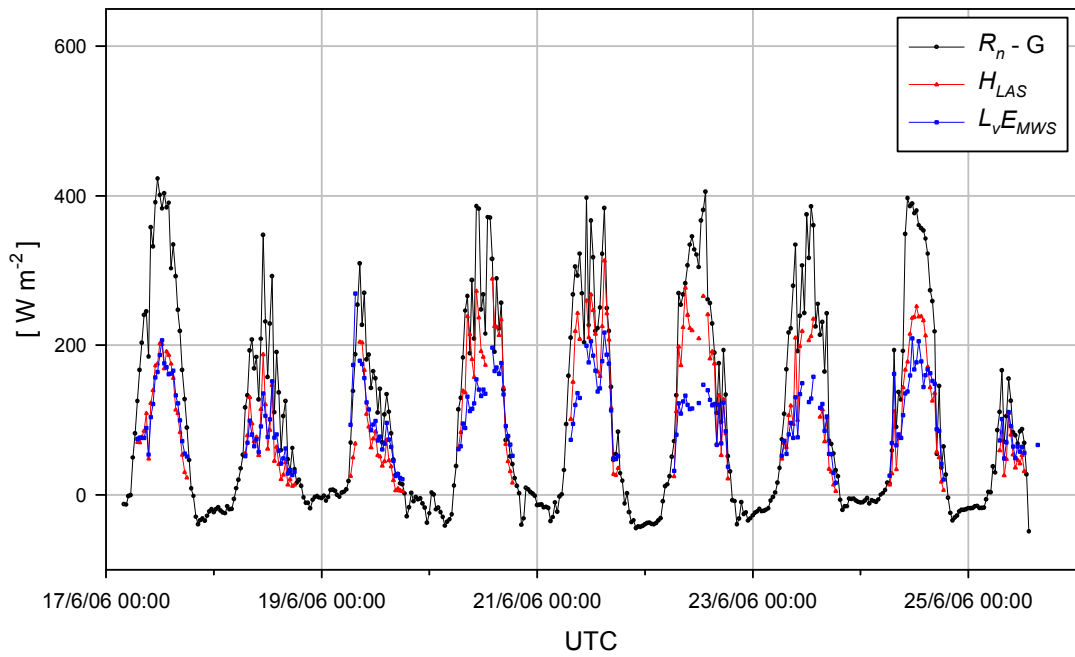
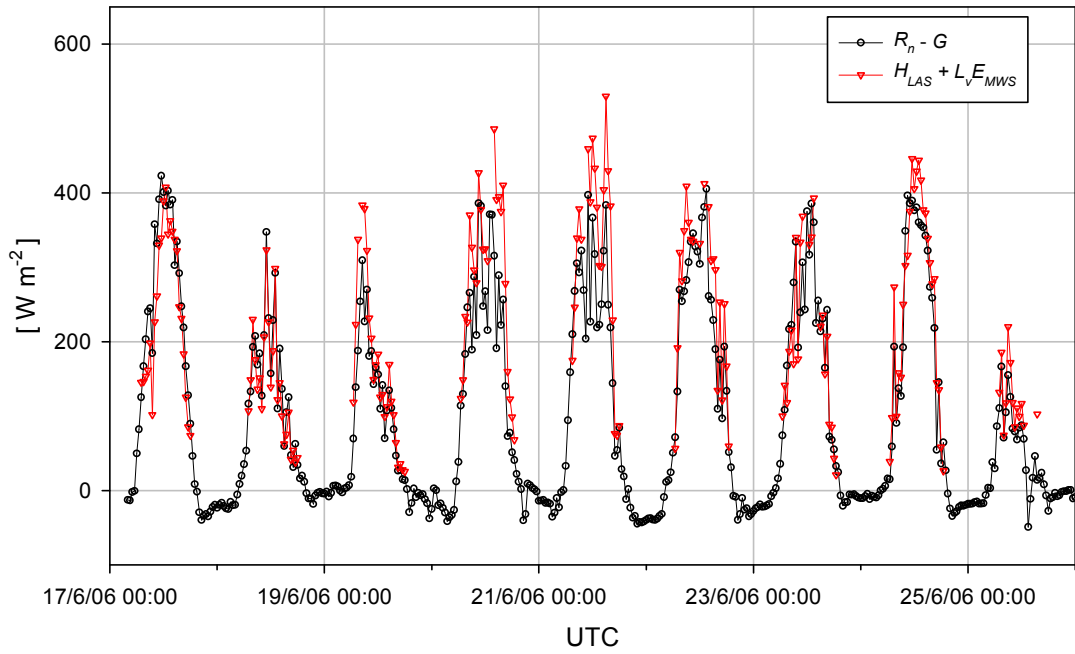
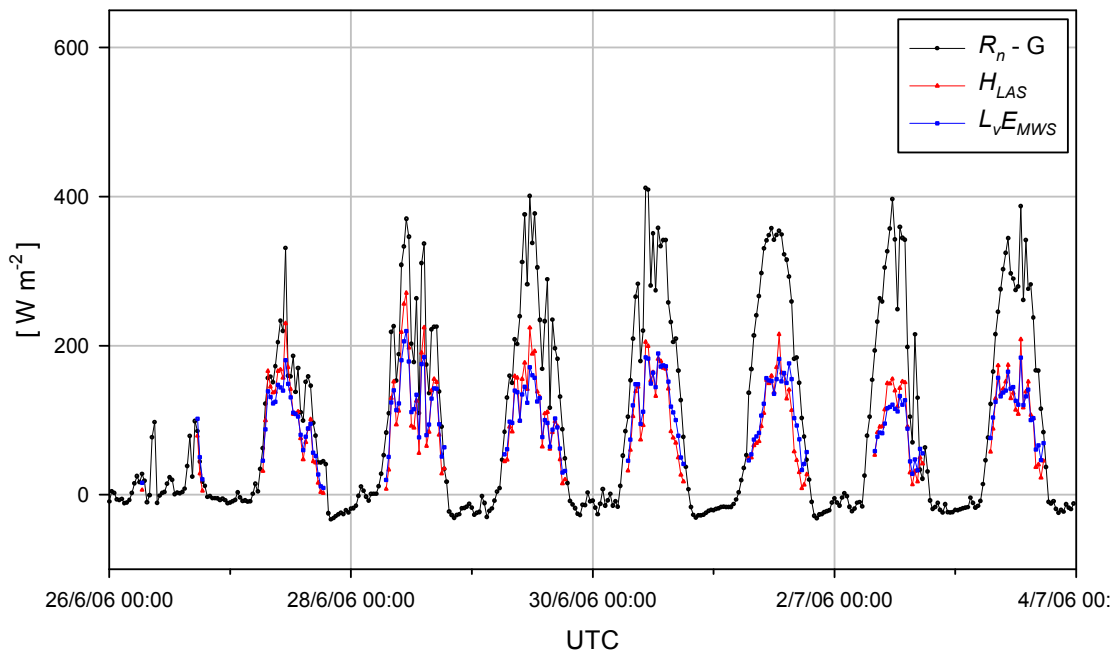
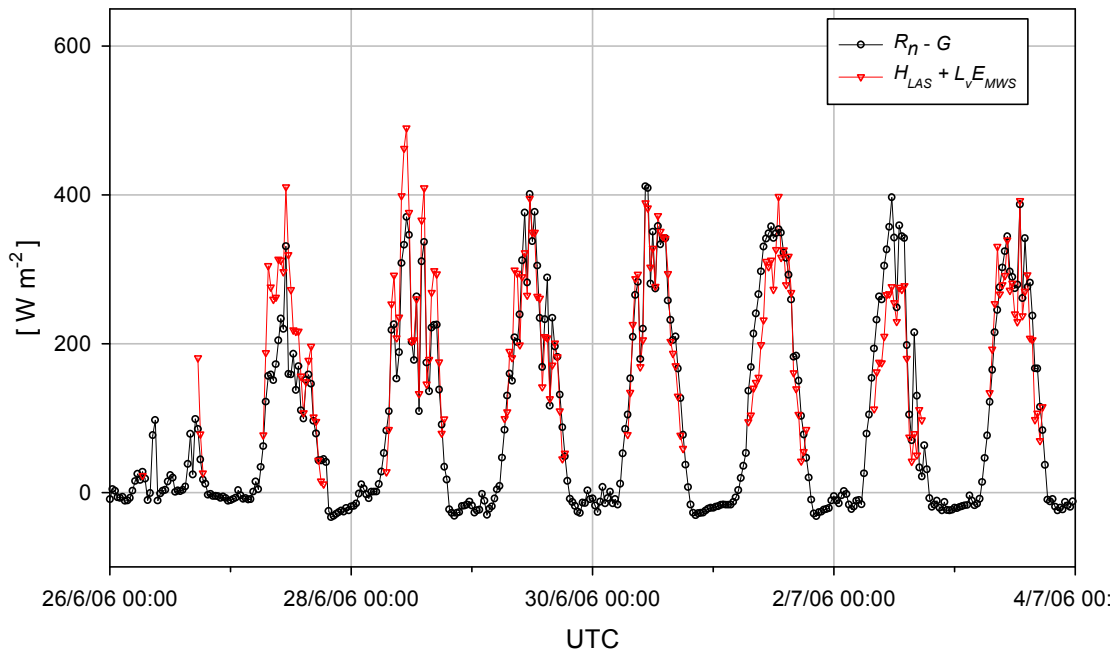


Figure 5-12 The energy balance for the first period (between 17/6/2006 and 25/6/2006, blue points) and the second period (between 26/6/2006 and 3/7/2006, red triangles). The first period energy balance closure has a slope of 1.00, and  $r^2$  of 0.78; for the second period, the slope is 0.91, and  $r^2$  is 0.77; the offsets are  $31 \text{ W m}^{-2}$  and  $7.5 \text{ W m}^{-2}$ , respectively.



**Figure 5-13** Time series of energy balance components:  $H_{LAS}$ ,  $L_v E_{MWS}$  and  $R_n - G$ ; first period.



**Figure 5-14 Time series of energy balance components:  $H_{LAS}$ ,  $L_v E_{MWS}$  and  $R_n - G$ ; second period.**

The time-series of the available energy ( $R_n - G$ ),  $H_{LAS}$  and  $L_v E_{MWS}$  are plotted in Figure 5-13 (first period) and Figure 5-14 (second period). On the whole  $H_{LAS}$  and  $L_v E_{MWS}$  show the expected diurnal variation and the partitioning of the fluxes is reasonable for this type of land cover. The Bowen ratio is often close to one, but is much higher (up to 1.8) between 20<sup>th</sup> and 24<sup>th</sup> June 2006, and some of these days have large over-closure of the energy budget.

In order to understand what causes this observed over-closure of the energy budget, Figure 5-15 shows the time series for  $H_x / (R_n - G)$ , where subscript  $x$  denotes either the LAS, or EC, for each of the sites MT and GP. The assumption here is that  $H_{LAS}$  should broadly follow the trends of both EC sites, which should be partly representative of fluxes from the source area of  $H_{LAS}$ , and therefore show when these measurements are physically reasonable. This approach is taken in the absence of a full aggregated EC measurement that could be completely representative of the LAS's source area.

Figure 5-16 compares  $u_*$  measured by each EC station with the value found by the LAS iteration. The LAS  $u_*$  is close to 1:1 with that measured at GP, whilst  $u_*$  from MT is much higher due to the increased roughness of the trees. At high values of LAS  $u_*$  ( $> 0.5$ ) the linear relationship with EC measurements breaks down and there is no longer a clear relationship. The comparison of MT  $u_*$  with GP  $u_*$  is also shown; this has much less scatter, and maintains a linear relationship at high  $u_*$ .

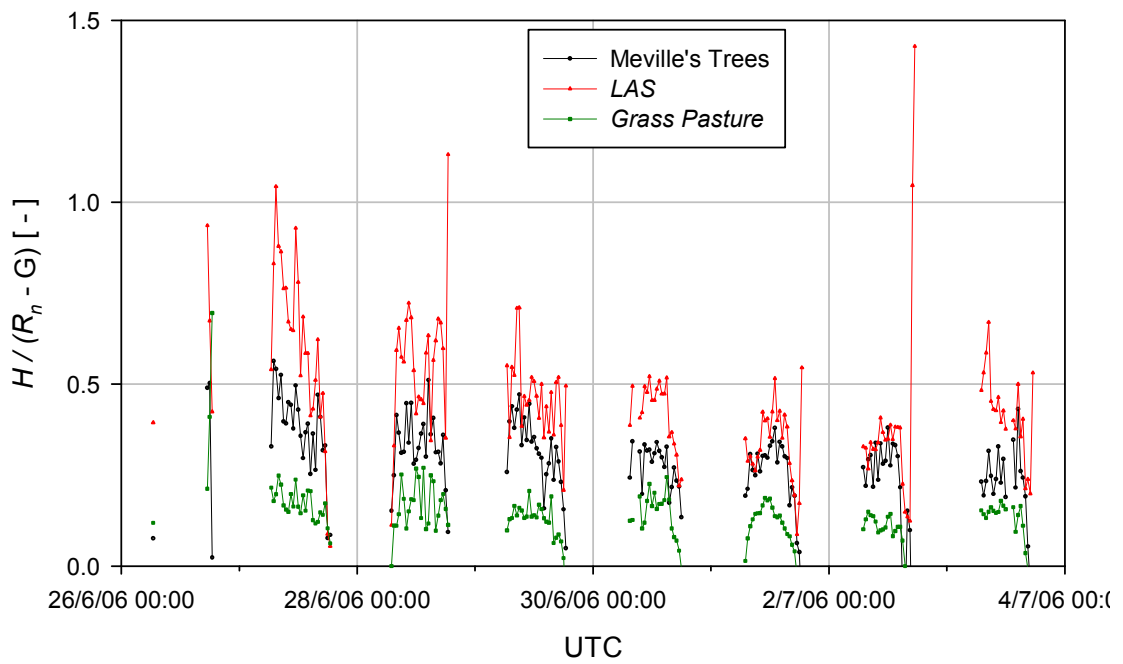
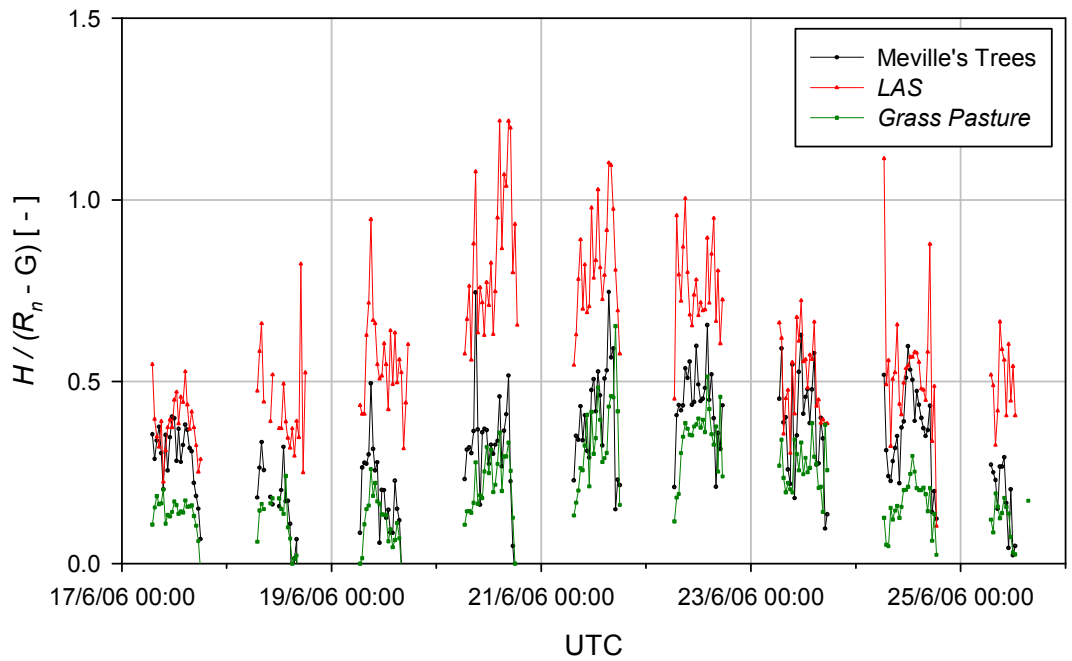


**Figure 5-15 The sensible heat flux fraction of available energy for EC and LAS measurements.**

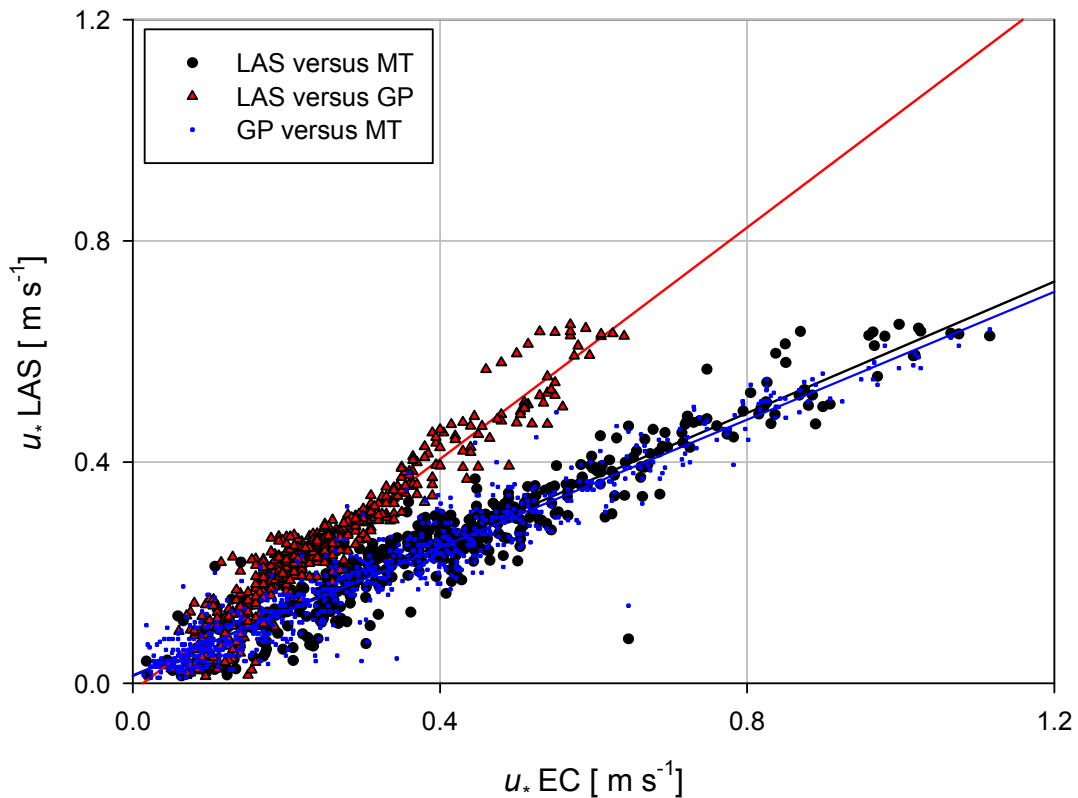


Figure 5-16 Comparison of  $u_*$  from LAS iteration and measured by EC.

## 5.5 Discussion

The energy balance closure provides a test for this application of two wavelength scintillometry over mixed vegetation and complex topography. Consideration is first given to the errors in the measurements of the available energy, and their spatial representativity. The overall accuracy of  $R_n$  measured by the NRLite is not specified by the manufacturer, but by comparison with the CNR1, the accuracy is estimated as better than  $\pm 10\%$ . Using 30-minute averaging times there can be significant difference between the incoming solar radiation of the LAS-MWS source area (SA) and the point

measurement made at GP. This may result in a bias in  $R_n$ , since the prevailing south-westerly wind direction blows the clouds first over the LAS-MWS SA, then over the GP  $R_n$  sensor; therefore, particularly at low wind speed, there could be a lag in  $R_n$ , of 5 to 10 minutes, relative to the area-averaged value for the LAS-MWS SA. In this respect these measurements are not ideally located – they would be better located near the middle of the LAS-MWS SA, for the prevailing wind direction – or better, replicated to sample at more points in the SA for all wind directions. The variation in  $R_n$  with land cover type is much smaller as only the outgoing components are affected by the variation in albedo; the overall accuracy and representativity of  $R_n$  is estimated to be  $\pm 10\%$ .

The error for the single point measurement of  $G$  is large, of the order of  $\pm 20\%$ . However, for  $G$  the variation with land cover type is the most significant factor, for example the bare soil pig field could be expected to have values of  $G$  at least 100% greater than those of the grazed grass field (GP) where  $G$  was measured. Accounting for the different land cover types in the SA, the accuracy of  $G$ , including its representativity of the SA is estimated to be  $\pm 40\%$ .

There are also expected to be time lags in the 30-minute mean  $G$ , with respect to the other components of the energy balance, due to the thermal inertia of the soil and vegetation above the soil heat flux sensors (changes in the energy storage in this soil volume have not been accounted for); due to this measurement lag, the 30-minute means are not expected to exactly close the energy balance. It should also be noted that there is some debate over whether the energy balance should be expected to fully close e.g. Foken

(2008). There are issues (such as stationarity) affecting whether the energy balance should close. However it was found in the Sheepdrove 2004 Experiment that the EC energy balance closures were close to unity, which suggests that for this landscape, under similar conditions, good energy balance closure may be expected.

The  $r^2$  values of 0.77 and 0.78 for the regressions of  $(H_{LAS} + L_v E_{MWS})$  with  $(R_n - G)$  (Figure 5-12) demonstrate that overall there is strong correlation between these quantities, whilst it can also be seen that there is considerable scatter. The first period of data has a root-mean-square deviation (RMSD) of  $63 \text{ W m}^{-2}$ , and for the second period it has a slightly lower value of  $57 \text{ W m}^{-2}$ . The obvious difference in these two periods is the average energy balance closure, which has a slope of 1.0 for the first period but reduces to 0.91 for the second period - there is a bias in energy balance closure which is probably attributable to the prevailing weather conditions. Under predominantly cool and windy conditions the energy balance closure is 9 % higher than under calm and hot conditions. The relationship of these conditions and their influence on the energy balance closure is further discussed, later in this section.

The time-series of the energy balance (Figure 5-13 and Figure 5-14) show that on most days the daily total energy measured by  $H_{LAS} + L_v E_{MWS}$  and  $R_n - G$  are very similar, and mostly follow the same diurnal course. Some of the exceptional behaviour seen in the time series is now examined in order to understand what drives the differences in the energy balance, and to assess the performance of the LAS-MWS system.

$H_{LAS} + L_v E_{MWS}$  are approximately 25 % lower than  $R_n - G$  on 2/7/2006, when conditions are strongly convective ( $L_{Ob} = -10$ ), with wind speeds around 2 m s<sup>-1</sup> and wind from the SSE. Such a large difference may be partly due to the under-estimate of  $G$  for the LAS-MWS SA. In this case there is a large proportion of bare soil (in the pig field and the spring wheat fields) in the LAS-MWS SA. At low wind speeds it is expected that the bare soil surface temperature will become relatively high (because of reduced surface cooling), increasing  $G$  with respect to that measured at GP, which would reduce the available energy from the LAS-MWS SA, and bringing the energy balance closure nearer to unity.

Another consideration is that the wind direction is nearly aligned with the scintillometers' paths, and this, combined with the low wind speeds, reduces the crosswind speed to near zero. At zero crosswind the scintillometer no longer sees any turbulence moving through its beam and although there may still be turbulence moving along the path, there is very little scintillometer sensitivity in this direction. Furthermore, as the wind speed approaches zero, the scintillometers' low frequency cut-off may begin to attenuate the measured turbulence spectrum – as this moves to lower frequencies with lower wind speeds. Future work is required to investigate whether the scintillometers' sensitivities are actually affected by either of these two factors.

Both  $C_{T^2}$  and  $C_{Q^2}$  on this day are, like the fluxes, about 25-30% less than on the following day, when the available energy is similar, but the crosswind is much higher, because the wind direction is more normal to the path. On the preceding day (1/7/2006), there is a similarly large reduction in  $H_{LAS} + L_v E_{MWS}$  compared with  $R_n - G$  in the morning, when the wind direction is again SSE.

The large under closure seen on 27/6/2006 also occurs with approximately the same wind direction. This latter day has much lower  $R_n$ , is cooler and has a correspondingly much lower  $G$ , but remains strongly convective ( $L_{Ob} = -7$ ). This suggests that the wind direction is a key factor. The LAS-MWS SA will change with wind direction but  $H_{LAS} + L_v E_{MWS}$  are expected to maintain reasonable energy balance closure, which they do for example when the wind direction changes from SW to NE. It is possible that under nearly free convection conditions, there is a problem with the application of MOST, but this would seem unlikely, as on other strongly convective days (e.g. 3/7/2006) the energy balance closure is very high. Therefore, it is suggested that the most likely explanation for these under-closures is due to the reduced sensitivity of the scintillometers at near-zero crosswind speeds.

Next, days on which there is over-closure of the energy balance by the LAS-MWS will be investigated. In the first period there is over-closure on 20/6/2006 to 22/06/2006, which coincides with consistently higher wind speeds of 6-8 m s<sup>-1</sup> and  $L_{Ob}$  of -50 to 100 m. The over-closure is of the order of 25% of the available energy, with the highest over-closures correlating with wind speed peaks and the correspondingly decreased  $L_{Ob}$ . The assumptions and processing steps used to calculate  $H_{LAS} + L_v E_{MWS}$  are now examined in order to see whether they are reasonable.

Firstly it should be noted that both  $H_{LAS}$  and  $L_v E_{MWS}$  are higher than would be expected on 20/6/2006 to 22/06/2006. This suggests that rather than an error with either scintillometer, that there might be an error in the MOST flux scaling; however they are not independent because of the convective influence of  $H_{LAS}$  in the calculation of  $L_v E_{MWS}$ . Although the  $C_{T^2}$  values are

amongst the highest recorded in the experiment, they appear to be consistent with the rest of the dataset. Recent work (Kesteren, 2008; Kleissl et al., 2009) has shown that the LAS 150 may over-estimate  $H_{LAS}$ , but the Sheepdrove 2004 Experiment and the majority of the data presented here show no evidence of such a bias.  $C_{Q^2}$  is reduced with these high values of  $C_{T^2}$  as would be expected. There is some uncertainty as to the value of  $r_{TQ}$  but higher values would not reduce  $C_{Q^2}$  enough to give large improvement in closure, and at some instances  $H_{LAS}$  is very close to the available energy, so it appears that both fluxes are too large.

The possible contribution of vibrations to the measured signal variance was considered. It was found that under high wind speed conditions,  $C_{n^2}$  measured by the LAS still recorded very low values during the evening transition through near-neutral conditions, as was expected (e.g. Figure 5-10, on 20/6/2006). This observation implies that there was no significant contribution of vibrations to the LAS signal under these high wind speed conditions. Spectra for the MWS show noise peaks (Figure 5-5) but these do not correlate with wind speed, and have also been seen in tests conducted at the Chilbolton Test Range. In the latter test the MWS was mounted on very highly stable optical benches which were fully enclosed by cabins, so that vibrations could be excluded as an influencing factor (Kesteren, 2008)). In any case, for the MWS these noise peaks do not contribute to the measured  $C_{n^2}$ , as they are rejected by the BPF.

Thus there is confidence in the measurements of  $C_{T^2}$  and  $C_{Q^2}$  but the resultant fluxes are too high, implying that the over-estimation of these fluxes

lies in the MOST scaling. The value of  $u_*$  and  $L_{Ob}$  are both calculated in the iteration of  $H_{LAS}$ , assuming  $z_0 = 0.02$ . The calculated  $u_*$  is compared to the measured  $u_*$  from the EC stations in Figure 5-16. The highest LAS  $u_*$  values correlate poorly with the EC measured  $u_*$ , whilst these latter measurements correlate well with one another even at high values. This suggests that the EC measurements of  $u_*$  are no longer representative of the LAS SA, or that there is some other error in the LAS calculation of  $u_*$ , such that it is no longer representative of its expected SA. The former may result from the different LAS SA for these values of  $L_{Ob}$ . There is higher scatter in the LAS-EC  $u_*$  regressions compared with the EC-EC  $u_*$  regression, partly because of this variable SA of the LAS. There is high uncertainty for  $z_0$  of the order of  $\pm 0.01$ .  $z_0$  was estimated for the land cover in the typical SA of the LAS, and was checked by the regression of  $u_*$  with the EC stations. By assuming that  $z_0 = 0.01$  (which is rather unrealistically low – a value expected for bare soil), the over-estimation of  $H_{LAS}$  and  $L_v E_{MWS}$  is reduced significantly, since  $u_*$  is decreased, as expected. However, these values of  $u_*$  are physically rather small compared to those expected from the EC measurements. It is important to note that  $z_0$  is dependent on the dynamic SA of the LAS and perhaps needs to be treated as a dynamic parameter that should be calculated for the SA corresponding to a particular stability.  $L_{Ob}$  is calculated using this value of  $u_*$ , hence, it is important to have a good parameterisation.

$H_{LAS}$  is determined by MOST assuming a particular stability function. There is uncertainty over the form of this function and several functions are available in the literature. The stability functions published have the usual constraints of

MOST - i.e. they have been fitted to data measured over relatively homogeneous and extensive terrain. Such functions may not fit the MOST relationship for the complex topography of Sheepdrove Farm. However, it may be the case that even for homogeneous terrain the stability functions tend to have been poorly fitted to the experimental data and that they require some modification. With the limited resources of this experiment, neither the stability function, nor the application of MOST at high wind speeds can be fully tested, because there is no independent measurement of  $H$  for the SA of the LAS. Finally, it may be the case that the MOST relationship breaks down at high values of  $u_*$ , however the very high correlation of the scintillometer fluxes seen under these conditions suggests that a MOST scaling relationship is applicable but that the magnitude of that relationship is incorrect. An independent measurement of either  $H$  or  $u_*$  for the LAS SA is required to investigate this further. This may be possible from the datasets of the Sheepdrove 2004 Experiment.

$H_{LAS}$  and  $L_v E_{MWS}$  are found to be of similar magnitude for most days of the experiment, and show no sign of water stress on the hot convective days at the end of the experiment. Although there is greater uncertainty in the magnitude of scintillometer fluxes at high wind speed, it is found that  $H_{LAS}$  is higher than  $L_v E_{MWS}$  for the high  $u_*$  days, and the same trend is seen in the EC data.

Future work should verify the calibration of the LAS and the MWS, particularly for the ranges of  $C_{n^2}$  measured here. Further investigation is required of the under-estimate for periods of near-zero crosswind speed, using high frequency time-series and spectral analyses – this would allow at least

automatic quality control of these instances. For example, the spectrally best periods could be selected for use in flux calculations. This approach of rejecting poor periods of data is acceptable since the large spatial sampling volumes allow very short (1 to 5 minute) periods to be used to calculate statistically robust fluxes. Re-examination of the datasets from the Sheepdrove 2004 Experiment may provide high  $u_*$  data with which to test the fit of the  $C_{T^2}$  and  $C_{Q^2}$  stability function. Future experimental work could easily make use of bichromatic scintillometry, to directly measure  $r_{TQ}$ , to reduce the error in assuming a constant value. The work here has been confined to unstable conditions, due to increased uncertainty of the stability function for stable conditions; however, future work should also apply the technique during stable conditions.

## **5.6 Conclusions**

A new design of MWS has been tested. Its scintillation spectrum was found to obey the expected Clifford theoretical spectrum; an instrumental noise peak was found that in most cases could be removed from the  $C_{n^2}$  measurement by judicious filtering of the scintillation signal. Except at very low crosswind speeds, water vapour absorption effects were also removed without affecting the measurement of  $C_{n^2}$ .

Measuring both  $H_{LAS}$  and  $L_v E_{MWS}$  by two-wavelength scintillometry provides large area-averaged fluxes that can be readily validated by testing the energy balance closure, using a few additional point measurements. The addition of

an EC station allows the verification and quality control of  $u_*$ , as calculated by the LAS iteration. The two-wavelength method has been tested over complex topography and mixed vegetation, and the results show that reliable measurements of the landscape scale  $H_{LAS}$  and  $L_v E_{MWS}$  can be obtained. The 30-minute mean  $H_{LAS} + L_v E_{MWS}$  closes the energy balance to 94 % on average with an RMSD of  $60 \text{ W m}^{-2}$ , and closely follows the diurnal course of  $R_n - G$ . The scatter in the energy balance closure, for most days, can be attributed to the mismatch in SAs and temporal lags, especially of  $G$ . It was found, for the cases of near-zero crosswind speed and high wind speeds, that there were greater differences in the energy balance closure, indicating higher uncertainty of the  $H_{LAS}$  and  $L_v E_{MWS}$  measurements at these times. For near-zero crosswind speeds  $H_{LAS} + L_v E_{MWS}$  is up to 30% lower than  $R_n - G$ , possibly because the scintillometers are insensitive at zero crosswind and/or due to the low frequency cut-off of the scintillometers.

At high wind speed (and high  $u_*$ ) there is up to 25% over-closure that probably results from the application of MOST, and that this may be due to a poorly fitting  $C_{T^2}$  and  $C_{Q^2}$  stability function, although that cannot be directly tested here. It has also been noted that  $z_0$  is dependent on the LAS-MWS SA, and therefore the stability, thus treating  $z_0$  as a constant parameter, may contribute somewhat to these over-estimates of fluxes.

The two-wavelength method has been successfully applied over complex topography, resulting in high landscape-scale energy balance closure. For two special case noted above, there is increased uncertainty of the fluxes. The method has been shown to be powerful in capturing large-area information,

and is convenient, cost effective, and non-invasive. With further research to fine-tune the technique, particularly for high  $u_*$ , this work shows that the method can be more widely applied than the restrictions of MOST would suggest, and should become widely adopted.

## Chapter 6 Discussion

### 6.1 Overview

The work presented here has set out to extend and investigate the measurement of the landscape scale sensible and latent heat fluxes over topographically complex terrain with mixed vegetation. Advances have been made both through the extension of theory and the analysis of experimental campaigns, including the commissioning of a unique new design of MWS. In this chapter these findings are brought together and the synthesis of these results is further discussed, with reference to other published work, in order to present the state-of-the-art of scintillometry over complex terrain. Naturally there are issues here which are not unique to complex terrain, and these are included to give a more complete picture.

It is worthwhile to step back and recall the issues that complex terrain raises. Firstly, there are theoretical challenges:

1. The assumptions required to solve the wave equation as applied to the scintillometer.
2. The assumptions of MOST.

3. The determination of the effective heights.

Secondly, there are practical considerations (often these have associated theoretical counterparts):

4. How can either  $u_*$ , representative of the LAS source area (SA), be measured, or a representative estimate of  $z_0$  be determined?
5. How should the SA be calculated – also, how does the complex topography modify the SA?

Thirdly, there are more general issues for the application of scintillometry:

6. How can a scintillometer be calibrated?
7. How should the LAS-MWS data be filtered to remove the contribution of absorptions? At very low crosswind speeds, does the filtering attenuate the scintillation signals, or is a fundamental limit reached where the LAS and MWS become insensitive?
8. How well is the surface energy balance expected to close?

Overall, this chapter aims to provide guidance in the important considerations and requirements of scintillometry over complex terrain, and suggestions regarding best practice for particular applications – for example, the needs of the micrometeorological researcher are quite different to those of the irrigation scheduler. Finally, in 6.10 a summary of findings and future work is presented.

## **6.2 The Assumptions Required to Measure Structure Parameters by Scintillometry**

The method of solving the wave equation for electromagnetic wave propagation through the turbulent atmosphere, and its subsequent relationship to the scintillometer output, requires quite a number of assumptions. These are fully analysed and discussed by Moene et al. (2004), but are also briefly considered here, for completeness.

Firstly, the transmitting medium is assumed to be locally isotropic. As was already noted in Section 2.3, at sufficiently small scales ( $< 2 - 3$  m) this may generally be valid, but increasing anisotropy is expected at larger scales and heights. Particularly for the LAS, where the most sensitive scale is of the order of the aperture diameter (0.15 m), this assumption should be valid, whereas for the MWS it approaches the suggested limit of this assumption.

Small angle scattering is assumed, and this may be violated for a particular combination of  $\lambda, L, D$  and scattering strength of the medium; refractive inhomogeneities should be much larger than  $\lambda$ , to ensure small angle scattering, although it has been suggested that larger angle scattering will not in any case reach the receiver, and therefore does not need to be considered. However, Wheelon (2006) gives  $\sigma_{\chi}^2 < 1$  as the condition for weak scattering, hence the validity of measurements can be directly checked.  $\sigma_{\chi}^2$  increases approximately with decreasing  $\lambda$  and more strongly with increasing  $L$  (6.3). The much longer wavelength of the MWS compared with an optical scintillometer means that weak scattering can be safely assumed, but for the LAS consideration must be given to the possibility; as already noted, this can

be avoided by measuring at sufficient height. Suitable height and pathlength combinations can be determined from the graph provided in the LAS 150 Manual – this indicates that for the SOF setup, saturation will not occur at least until  $H_{LAS} > 450 \text{ W m}^{-2}$ . These curves assume that the path is parallel to the land surface, which is assumed to be flat; however, the effective height for the complex topography can be appropriately used to interpret these curves, as it takes account of the non-linear height scaling of  $C_{T^2}$ , as well as the path weighting function.

The assumption of the Kolmogorov spectrum is well accepted. The MWS Fresnel zone, and for the LAS the aperture diameter, are both large compared with the inner length scale of turbulence, and therefore, the modification to the spectrum for inner scale effects (Hill bump) is not required. Spectra presented in Chapter 5 show that the measured turbulence obeys the expected Kolmogorov spectrum under most conditions, including at high wind speeds. Since spectra for each and every 10-minute period could be examined for quality assurance and further investigation, an automated analysis program is required to assess how well spectra meet the expectations of theory.

The accuracy of the applied LAS-MWS combination to measure  $C_{T^2}$  and  $C_{Q^2}$  should be improved by the application of bichromatic scintillometry as demonstrated by Lüdi et al. (2005a), to directly measure  $r_{TQ}$  from the cross-correlation of the LAS and MWS scintillation signals.

### **6.3 Structure Parameter-Flux MOST Relationships**

Since the goal in hydro-meteorological applications is the measurement of  $H_{LAS}$  and  $LE_{MWS}$ , the dependence on similarity theory is critical to enable the scaling of  $C_{T^2}$  and  $C_{Q^2}$  to fluxes. It is worthwhile noting that scintillometry may be capable of properly measuring  $C_{T^2}$  and  $C_{Q^2}$  over complex terrain, and thus provide valuable micrometeorological information, but under some circumstances, may not be able to properly measure  $H_{LAS}$  and  $LE_{MWS}$ , because of inappropriate application of the  $C_{T^2}$ -flux MOST relationship.

The key assumptions are that the terrain is flat and homogeneous, and that conditions are stationary. Stationarity is an issue for homogeneous as well as complex terrain, and it is straight-forward to test the acquired dataset for this condition (Panofsky and Dutton, 1984). Furthermore, the much shorter time periods required for statistical stability of the scintillometer  $C_{n^2}$ , compared with EC measurements, reduces the effect of any non-stationarity, as shorter averaging periods can be used.

In the experimental work presented herein, the terrain is clearly neither homogeneous nor flat. However, it may be characterised as relatively smoothly changing for the majority of the SA, and there are few large obstacles. The SA-averaged  $z_0$  is low (depending on the crops planted), and it is estimated that there is only a small influence of the hedgerows and small trees on  $z_0$ .

It is postulated that whilst the topography is steeply changing in places along the path, for the prevailing wind directions (especially from SW), the SA is sufficiently smooth and smoothly changing (generally without abrupt features), that the mean streamlines follow the land surface and under most conditions remain parallel to it; the exception is the flow over the valley bottoms where there may be boundary layer separation (Stull, 1988). The Sheepdrove Organic Farm (SOF) scintillometer path is setup to be over a small tributary valley, such that this valley is more or less directly below the scintillometer beam, and therefore contributes little to the source area, except when the wind direction is aligned with the path. For wind directions along the scintillometer path, the steep valley close to the SE end of the path may produce more severe flow distortions, particularly at high wind speeds. This postulation is supported by the EC measurements on sloping topography in the SW SA, which only require a small rotation of the vertical coordinate system to achieve a zero mean vertical wind speed (as would be expected of mean streamlines that are parallel with the surface). The exception to this is the Meville's Trees EC station, which may be too close to the roughness sub-layer at high wind speeds.

By installing the scintillometer path sufficiently high above these topographic features, it is expected that the streamlines will be nearly parallel to one another, and close to horizontal. Under these circumstances the flow regime approximates that of extensive flat terrain. The issue then is to have robust methods to determine if and when the flow regime may have departed too far from the ideal, invalidating the application of MOST.

The constraint of land surface homogeneity is also overcome by making scintillation measurements at sufficient height. Meijninger et al. (2002b)

demonstrated that measurements made above the blending height could produce reliable area-averaged estimates over flat farmland with mixed crops. It is expected that above the blending height the individual boundary layers of each land surface type are well mixed, presenting a single homogeneous flux. The approach has been further tested successfully, over moderately varying topography, as well as heterogeneous land surface, in the LITFASS-2003 experiment (Meijninger et al., 2006).

In summary, care must be taken to ensure that scintillometry is appropriately applied, which means here that the measurement height must be sufficiently above the blending height, but not above the surface layer (constant flux layer). Such heights ( $> 20$  m) combine well with long paths (2 - 5 km) to give good sensitivity ( $\propto L^3$  for the LAS  $\propto L^{11/6}$  for the MWS), without risk of saturation (see Section 6.2) of the LAS (since  $C_{n^2}$  decreases rapidly with height). The dependency on the  $C_{T^2}$ -flux MOST relationship continues in the next section, where this relationship determines the scaling of  $C_{T^2}$  with height.

## **6.4 The Determination of the Effective Heights**

The  $z_{efH}$  and  $z_{efLE}$  can now be properly calculated according to the new derivations set out in Chapter 4. Over complex topography it is essential to recognise the difference in  $z_{efH}$  and  $z_{efLE}$ , in order to correctly scale the flux. These effective heights also appear in other calculations, most notably that of the source areas – which accentuates the differences in these SAs that are unavoidable, even for ideal paths (because of the different path weighting

functions). Crucially, the application of these calculations is dependent on MOST to scale  $C_{T^2}$  and  $C_{Q^2}$  with measurement height.

There are simplifying assumptions, in the derivation of the effective height, which might be challenged, particularly over complex terrain. Firstly, the assumption of perfect correlation of temperature and humidity fluctuations has been found to be invalid by several experiments, and the LAS-MWS data processed by the two-wavelength method assumed a value of  $r_{TQ} = 0.8$ , as a more realistic value (Beyrich et al., 2005); however this is not a serious violation of MOST. Secondly, the fluxes are assumed to be constant along the scintillometer path, which is a reasonable assumption if the measurements are above the blending height.

## **6.5 Determining a Source-area-averaged Friction Velocity**

The rule-of-thumb estimation of  $z_0$ , representative of the LAS SA, produces reasonable estimates of  $u_*$ , calculated by the LAS iteration, using a single wind speed, which compare well to the EC measured values. This method is certainly a pragmatic solution, given the resources required to have a better estimate, e.g. by making and aggregating EC measurements of  $u_*$  for different land surface types. An alternative method is to deploy a second LAS at a different height, in order to determine  $u_*$  directly, by simultaneously solving Eq 2-34 for the two different heights. However, in practice this is costly, and requires tall masts or towers; furthermore, to achieve sufficient

sensitivity by making the measurement heights sufficiently different, the SAs become increasingly different – this method has not been attempted experimentally. A path-averaged crosswind speed measurement may improve the estimation of  $u_*$ , and is possible with some scintillometer configurations (e.g. Poggio et al., 2000).

It is worth considering simple improvements to the single LAS iterative estimation of  $u_*$ . It has been suggested in Chapter 6 that  $z_0$  should be a dynamic parameter, which should be set depending on the stability, to reflect the SA dependence on stability and wind direction. A fairly coarse range of values would be sufficient, and could be provided in the form of a look-up table, as has been implemented herein for the effective height dependence on stability. Clearly the effect of introducing a dynamic value for  $z_0$ , dependent on the SA, is only significant if there are widely varying roughness lengths contributing to the different SAs. This would add an additional step to the iteration, as of course the stability (required to calculate the SA) is dependent on  $u_*$ .

## **6.6 The Estimation of the Scintillometer Source Area**

The method of estimating the SA of a scintillometer was first demonstrated by Meijninger et al. (2002b), over flat terrain. Herein the Schuepp et al. (1990) footprint model was applied at discrete steps along the scintillometer beam, in a similar fashion to Meijninger's method. The Schuepp model assumes flat topography, and uniform source strength. The SA was calculated using the height of the beam along the path; effectively assuming that the mean flow

follows the topography. If the streamlines do not follow the topography below the beam, and instead flow across the valley, not fully down into it, then the SA would be over-estimated due an inappropriate measurement height (as would the fluxes). However, as previously suggested (Section 6.3), the measurements indicate that the flow streamlines closely follow the land surface, under most conditions, in which case the beam height is appropriate for the calculation of the SA; under these conditions, the complex topography should not lead to any serious error in the application of the footprint model.

The requirement of constant source strength may be considered to be approximately met, because the source magnitudes are not many times greater than one another, and in any case the measurement is above the blending height where the separate sources are assumed to have been well mixed. However, systematic validation of the SAs calculated was not possible in the experiments presented here.

## **6.7 Calibration of Scintillometers**

How a scintillometer may be calibrated has received surprisingly little attention until very recently. A scintillometer measures  $\sigma_\chi^2$  at a particular wavelength, over an accurately known path length, so that according to theory,  $C_{n^2}$  may be calculated from  $\sigma_\chi^2$  (Eq 2-12, for the MWS, and Eq. 2-14 for the LAS). In this section the scintillometer calibration is defined as the relationship of the measured  $C_{n^2}$  with the true value of  $C_{n^2}$ , within the limitations of the measurement error – that is to say, if the calibration is perfect then we have only a random error associated with the instrument noise, otherwise a

calibration error leads to a bias error in the measurement. The difficulty of performing a scintillometer calibration then becomes clear: there are no other published methods of measuring a directly comparable  $C_{n^2}$ . The methods to test scintillometry and scintillometer calibrations depend on comparisons with micrometeorological measurements, which are point measurements and require additional theoretical assumptions. For example, the most closely related micrometeorological variable is  $C_{T^2}$  and it must be measured at the same height in order to avoid further assumptions and uncertainties of height scaling (Kohsiek and Herben, 1983). Such a comparison was first made by Gurvich's group in the USSR, as reported in Wheelon (2006). Wheelon remarks that the theoretical pathlength dependency has never been experimentally tested, because of the experimental difficulty of such a test, which ideally requires the different length paths to have the same  $C_{n^2}$  along the whole pathlength. Thus the fundamental theoretical relationships on which the scintillometers depend have become accepted with little formal testing.

As well as the testing of the scintillometer theory, there are instrumental factors to consider in the calibration. Perhaps because the transfer function of a scintillometer is quite simple, it has not been an issue in the literature; it may also be that the lack of a commercial source of scintillometers until about a decade ago, prevented multiple units being inter-compared, and very few groups have had access to more than one design of scintillometer, which would allow different designs to be inter-compared. However, there have now been three inter-comparison studies in the last 2 years. The Chilbolton 2007 experiment compared a LAS 150 with an earlier design of LAS built by Wageningen University, The Netherlands. This comparison showed a very large over-estimate (around +50%) by the LAS 150 of both  $C_{n^2}$  and  $H_{LAS}$ ,

when compared with the Wageningen LAS and EC measurements (Kesteren, 2008). Large inter-unit variations were found for the LAS 150 (Kleissl et al., 2008); and over-estimates of  $H_{LAS}$  compared with those calculated from a Scintec AG (Rottenburg, Germany) boundary-layer scintillometer (Kleissl et al., 2009). However, satisfactory calibration of the LAS 150 instrument used at SOF has not yet been possible due to the lack of a suitable reference instrument. It is also noted that the Chilbolton Test Range is only 500 m long and the measurements were made at a height of 4 m, whilst in Kleissl's intercomparison study the path was also short (635 m), and the scintillometers even closer to the ground (at a height of about 1.6 m). Thus for both of these studies  $C_{n^2}$  values were often much higher (up to an order of magnitude) than those measured during the Sheepdrove Experiments, whilst conversely the scintillometer signal recorded over the Sheepdrove path,  $\sigma_{\chi}^2$ , was much higher due to the much longer pathlength. Only in Kleissl's earlier LAS 150 intercomparison was the measurement regime comparable to Sheepdrove. Thus, due to the lack of a direct comparison with which to calibrate the Sheepdrove LAS 150, only the manufacturer's calibration has been applied herein (with an effective diameter of 0.145 m for the Fresnel lenses) – and within the uncertainties of the Sheepdrove 2004 experiment, there is no evidence to suggest that there is a significant calibration bias error in the measured  $C_{n^2}$ . Tests, similar to those by Kesteren (2008), with this unit at Chilbolton (without a suitable reference instrument) did discover a large noise peak in the measured spectra, which has since been corrected by the manufacturer. This would have contributed noise to the Sheepdrove data, resulting in a very small offset in  $C_{n^2}$  - the relative significance of the offset

having been greatly reduced by the much longer pathlength at Sheepdrove, which increases  $\sigma_{\chi}^2$  by a factor of 115.

## **6.8 LAS-MWS Filtering: Water Vapour Absorption and the Case of Near-zero Crosswind speeds**

The LAS receiver intensity fluctuations are limited in temporal frequency by the band-pass filter (BPF) built into the receiver analogue electronics. This scintillation signal bandwidth is specified as 0.2 to 400 Hz, which should give reasonable rejection of any water vapour absorption fluctuations which only contribute at very low frequencies. The type of filter is not specified, in particular, the steepness of its roll-off, but is unlikely (because of increased cost) to have a very steep cut-off. This would imply that there could be significant residual signal contribution at much lower frequencies (e.g. 0.1 Hz). It has been shown that absorption fluctuations increase in temporal frequency as the wind speed increases (Figure 2-4), and absorption fluctuations may therefore be introduced into the passband at higher wind speeds. At present there is no way to distinguish this effect, except perhaps by storing the raw demodulated signal (which has already been through the BPF) and applying additional filtering to reject lower frequencies – the effect of this may reveal, if there is low frequency contamination due to absorption. Information on the absorption strength of water vapour for the transmitter LED wavelength envelope should also be sought, to quantify the effect.

Spectra may reveal the low frequency contribution of absorption, but at such low frequencies there may also be intermittent turbulence, which can

obfuscate any absorption. Furthermore, for the spectra presented in Chapter 5, the application of the ARMASA smoothing routines to produce clearer, more readily interpreted spectra, may smooth-out any small absorption contributions. Kesteren (2008) was able to show a clear absorption spectrum for the unfiltered MWS at Chilbolton, and suggested that the filter cut-off may need to be at a higher frequency than 0.1 Hz. However, for the much longer path at Sheepdrove, the absorption strength relative to the scintillation strength is approximately one quarter of that at Chilbolton; therefore the use of a lower cut-off of 0.05 Hz is justified for the Sheepdrove MWS data, given the very much steeper roll-off of the Chebyshev type 2 digital filter. This lower cut-off frequency of 0.05 Hz was selected to prevent attenuation of the scintillation spectrum at low crosswind speeds, and is close to the value of 0.06 Hz applied to LITFASS-2003 MWS data by Lüdi et al. (2005a).

With suitable filter design, and selection of low frequency cut-off, water vapour absorption can be satisfactorily rejected – especially for moderately long paths. The exception to this is when the crosswind speed tends towards zero, and then the scintillation and the absorption coincide in the frequency domain. Under these circumstances, the fitting of the theoretical scintillation spectrum as advocated by Meijninger et al. (2006), may provide the best solution. Further analysis of near-zero crosswind speed scintillation is required in order to establish whether an inappropriate low-frequency cut-off of the BPF is responsible for the observed low  $C_{n^2}$  values. The alternative explanation proposed here, is that there are short periods of turbulence when the wind is aligned with the path (i.e. the crosswind speed is zero) and that, as theory predicts (Lawrence et al., 1972), the scintillometers have negligible sensitivity to these scintillations. Future spectral and/or time-series analysis should be

able to identify such events, and thereby exclude them from the time-averaged  $C_{n^2}$  measurement.

## **6.9 Closure of the Surface Energy Balance**

Much of the work presented herein relies upon the expected closure of the surface energy balance, and therefore further consideration is briefly given to that assumption in this section. The energy balance is a complex issue, and a full discussion of the subject is outside of the scope of this thesis. However, it is necessary to give some indication of the current thinking on this subject.

Lack of energy balance closure became a more widely recognised issue when carbon dioxide EC flux towers became prevalent towards the end of the 1990s. As well as instrumental deficiencies, the move to measurements over rough forest canopies was cited (e.g. Gash and Dolman, 2003) as a contributing factor - it was noted that earlier experiments over smooth surfaces such as grassland and short crops, sometimes achieved higher energy balance closure. However, the review of research on energy balance closure by Foken (2008) argues against most of these earlier suggestions for the causes of observed imbalance. Foken notes that with improvements in instrumentation over the last decade, the instrumental measurement errors are not sufficiently large to explain the typical (10 – 20 %) under-closure of EC based systems. This review concludes that the current experimental evidence suggests that there are large scale structures in the turbulent atmosphere over heterogeneous landscapes which EC stations cannot sample. The problem is one of scale – the EC sensors sample at a single point in space,

and therefore very long detrending times may be required to sample the large scale turbulence (which may conflict with the purpose of detrending, which is to remove slow background changes in the mean values of scalars e.g. Culf, 2000).

Foken goes further to hypothesise, citing studies of LITFASS-2003, that large scale secondary eddies exist due to the abrupt changes in the surface characteristics of a heterogeneous landscape and that these cannot be measured by the EC method – only by large-area averaging techniques such as scintillometry. Evidence to support this was also found by Von Randow et al. (2008) Whilst this hypothesis requires further testing, it has been established that there may be increased turbulent exchange at boundaries between land surface types, notably forest edges and hedgerows (e.g. Herbst et al., 2007). In LITFASS-2003 the scintillometer measurements were made above the blending height, as is the usual practice over heterogeneous terrain. Thus it is to be expected that the large-area scintillometer measurements will sample the additional contributions of boundaries and other discontinuities between land surface types. It may be the case that if EC measurements are made above the blending height, then they too would sample these additional contributions. Furthermore, the notion that either the LAS or MWS respond directly to such large scale eddies (of the order of 100 m) is incorrect – they are only sensitive to much smaller length scales (as shown in 2.6.3). There may be such smaller length scales associated with the proposed large scale secondary eddies, as they become unstable and break-down into smaller scales; however these could also be measured by an EC system.

Notwithstanding these comments, the fundamental advantage of very large spatial averaging by scintillometry appears to lead to improved energy balance closure, especially over heterogeneous terrain, under some conditions. However, it was found in the Sheepdrove 2004 Experiment, that the EC stations had very high energy balance closure, and in the context of the above discussion, this may imply that their energy balance is not influenced by large scale eddies, nor advection. Energy balances using the scintillometer fluxes were similarly well closed, for most conditions. Further research is required to test whether the high energy balance closure observed for the scintillometer fluxes is due to the gigantic spatial sampling of the scintillometer, or some other factor. Finally, it can be clearly stated that the surface energy balance is expected to close, and that this closure provides an appropriate test of the measured fluxes for both scintillometry and EC.

## **6.10 Recommended Measurement Strategies and Future Work**

It has been demonstrated by the experiments presented here, and the discussion developed, that scintillometry – both the LAS and LAS-MWS combination – can provide high quality flux measurements of both sensible and latent heats over complex topography with heterogeneous land surface types. The key findings of thesis are reproduced here, in terms of recommended measurement strategies, and future work:

- Large-area averaged sensible heat fluxes can be measured with a standalone LAS – giving results that compare very well to aggregated

EC measurements – with much more convenience and lower cost. Furthermore, the gigantic spatial sampling of the LAS provides statistically stable fluxes within minutes, which are representative of the heterogeneous landscape.

- MOST has been successfully applied over complex topography with some steep vertical gradients. It is suggested that because the landscape is fairly smoothly varying, the streamlines follow the landscape – and that this might be a simple rule-of-thumb requirement for MOST to remain valid. There is some evidence that, at high wind speeds, MOST may need adjustment either via the stability function or by a correction to the effective height – this should be the subject of future research.
- The standalone LAS can be used to calculate the latent heat flux, as the residual of the surface energy balance, provided that there are reasonable measurements of the ground heat flux and the net radiation. As it is quite difficult to measure or model the ground heat flux for the source area of the LAS, and to measure the large variations in the net radiation over the source area on cloudy days, this will introduce additional uncertainty. New satellite estimates of net radiation and models of soil heat flux, combined with *in situ* measurements may improve the accuracy of the calculated latent heat flux, without the need for spatial networks of point sensors. The standalone LAS system is capable of giving reasonable latent heat flux measurements, and the use of daily evaporation totals would average-out some of the temporal uncertainty; this would be particularly cost-effective for irrigation and water resource monitoring.

- New theory has been developed to improve the application of the LAS-MWS system over complex topography, by deriving an appropriate effective height for the measurement of the latent heat flux – thus both sensible and latent heat fluxes can be measured with confidence over complex topography.
- The LAS-MWS is a powerful technique to measure sensible and latent heat fluxes over large areas, even over complex topography and heterogeneous vegetation, and very high energy balance closure has been found. Truly large area-averages can be measured, without reliance on point measurements. Although the MWS is not commercially available, the LAS-MWS system can be considered to be cost effective, since it can replace a large number of in-field EC stations, is non-invasive, and the reduction in the number of stations has a lower operating cost. Providing both latent and sensible heat fluxes at such a large scale provides new research opportunities from process understanding to climate modelling.
- Future work is required to improve the methods for the calibration of the scintillometers.
- Systematic testing of MOST over complex topography is required. This should include both the detailed measurement of streamlines over complex topography, the height dependence of the temperature and humidity structure parameters and the determination of the exact form of the stability function. The stability function is currently the largest uncertainty in the application of MOST, for all terrains.

- The bichromatic method should be applied to the LAS-MWS system to directly measure the temperature-humidity correlation coefficient.
- It is recommended that the LAS-MWS system should be installed at a reasonable height above the ground, even close to the transceivers, because of the residual sensitivity of the MWS path weighting function at these points. A combination of short low vibration masts or towers with advantageous use of hills to provide additional height for the scintillometer path may be the best solution. Measuring any mast vibrations with accelerometers should be possible, and that would allow the contribution of vibrations to be removed the scintillation spectrum.

## **Appendix 1: Eddy Covariance Data Processing**

### **A1.1: Exploration of the Planar Fit Method for EC Processing**

Application of the EC method requires a flux coordinate rotation scheme to meet the condition that the mean vertical wind speed should be zero (i.e.  $\overline{w} = 0$ ), so that the measured flux is normal to the mean streamlines. In ideal situations of flat planar terrain, rotation should not be required, and conversely in complex terrain the applied rotations are particularly important, and have a large influence on the magnitude of the calculated fluxes. It is therefore necessary to explore the most appropriate rotation method and verify its validity. In particular, the finite time interval of the wind speed mean (e.g. 30 minutes) used to calculate a rotation may filter out eddies of a longer time - scale, which otherwise would contribute to the flux. Therefore it may be desirable to use a longer time interval, and if possible a long-term mean rotation.

Analysis was done for the Glebe Field, comparing un-rotated ARMA mean wind vectors with the results of different rotation schemes. Firstly a Planar Fit (PF) (Wilczak et al., 2001) was attempted by least squares fitting of a plane

through the un-rotated data. The PF was fairly poor ( $r^2 = 0.30$ ) and by viewing along the edge of the plane (sideways) it was evident that the data could be separated into two groups. An attempt was made to separate these data by wind direction; however no simple wind direction grouping was found. The conclusion was that this site is *not* suitable for the application of the PF method, simply because the terrain is more complex than a plane.

The requirement is to measure flux normal to streamlines, which should be the same as the flux normal to the surface, when the wind becomes parallel to the surface again at another location downstream. The flux is a scalar, so fluxes resulting from different rotations can still be added arithmetically, provided that they are normal to the mean streamlines. Hence given the complexity of the terrain, a simple and pragmatic approach, that meets the required criterion is the well-established McMillen style rotations (McMillen, 1988). These are calculated for each 30-minute mean period such that  $\overline{w} = 0$ , as well as the primary mean horizontal wind speed component ( $\overline{u}$ ) being rotated to the mean wind direction (i.e. the secondary mean horizontal wind speed component ( $\overline{v}$ ) becomes zero). Only these two rotations are applied (the latter is applied first). Note that the main advantage of the PF method is to reduce/eliminate the high-pass filtering effect of McMillen rotations, thereby increasing the low frequency contributions which may have otherwise been lost. This is of particular importance for forests, but much less so for Sheepdrove Organic Farm, because measurements are made at more than twice the canopy height, and mechanical turbulence (the friction velocity) is relatively high. It may be possible to reduce any low frequency loss by using a two or three hour period for the McMillen rotations, but it is expected that for

SOF this still may not make a significant difference to the fluxes, compared to 30 minute rotations, and thus this approach was not tested.

## **A1.2: The Relative Contribution of Eddy Covariance**

### **Processing Steps**

A major part of the data processing effort was the development of the EC raw data processing software known as *Mk4Processor* written in *Microsoft Visual Basic*. This program is called by the CEH flux data management software '*FluxView*', which was also extensively enhanced through this work. It was therefore both timely and necessary to set about some formal testing and verification of the CEH flux processing procedures. Some of this work is summarised here, with emphasis on the magnitude of the contribution of each processing step to the final calculated flux. It should be noted that whilst in the Eddy Flux community the term 'correction' is often used, this can be misleading. Often procedures that are termed corrections are in fact adjustments that are directly derived from the physics of the measurement, and are *not correcting for an error* but are applying a procedure to calculate the true flux.

Twenty-four hours of Glebe R3-LI7500 EC data, which had a good range of values and no quality control problems were used for these tests. The overall results are presented as stacked bar graphs in Figure A 1 and Figure A 2 for  $H$  and  $L_v E$  respectively, showing the relative contributions of each processing step and the final calculated fluxes. The solid blue line is the mean raw covariance used to calculate the final flux, before any further processing

steps are applied, except the application of the AoA re-calibration (which was applied to each 20 Hz record, before the covariance was calculated). Next, the data shown as the blue line, are transformed by coordinate rotation to give the black bars, and then the different coloured stacked bars show each subsequent additional contribution of a processing step (correction).

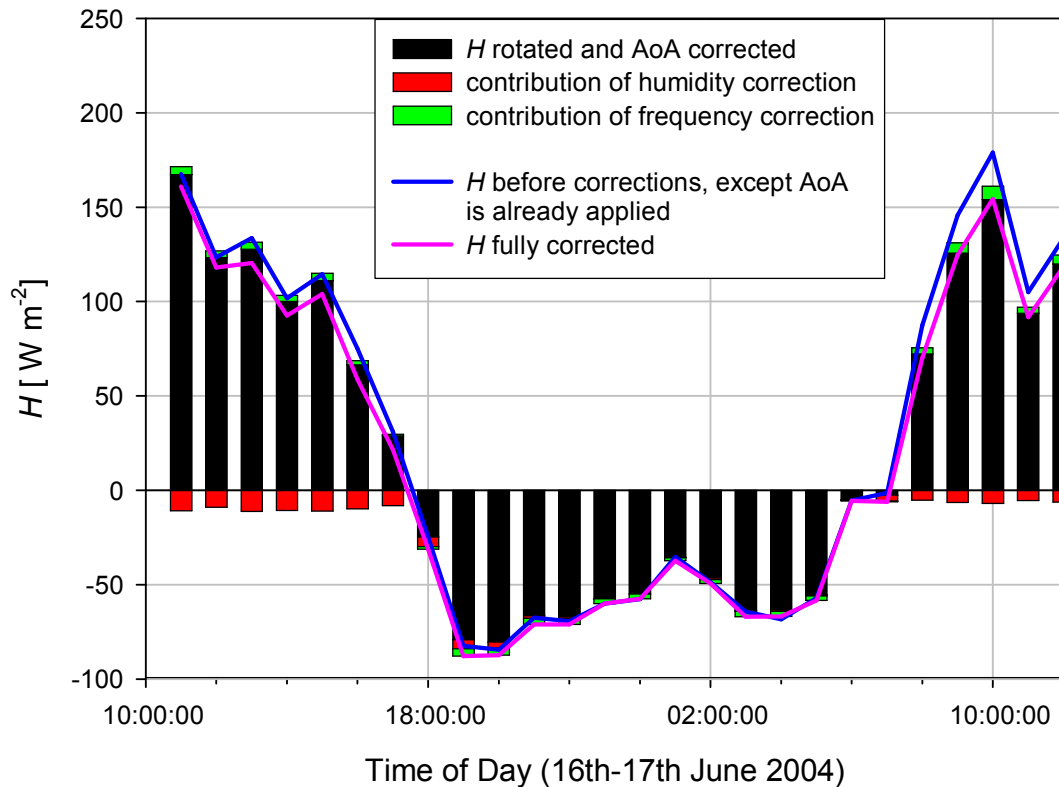


**Figure A 1. The analysis of the relative contributions to  $H$  of specific data processing steps (see text for full explanation).**

Finally, the solid pink line shows the summation of the stacked bars (some of which may be negative), and this is the final value of the fully corrected flux. These are very useful analyses, to gain understanding of the relative magnitude of the processing steps, to reveal at which times particular steps become more significant, and to check that the results are reasonable. With

relatively complex data processing it is important to ensure that processing errors are not hidden or masked by further processing, and to be able to diagnose which step is in error, if an error is suspected.

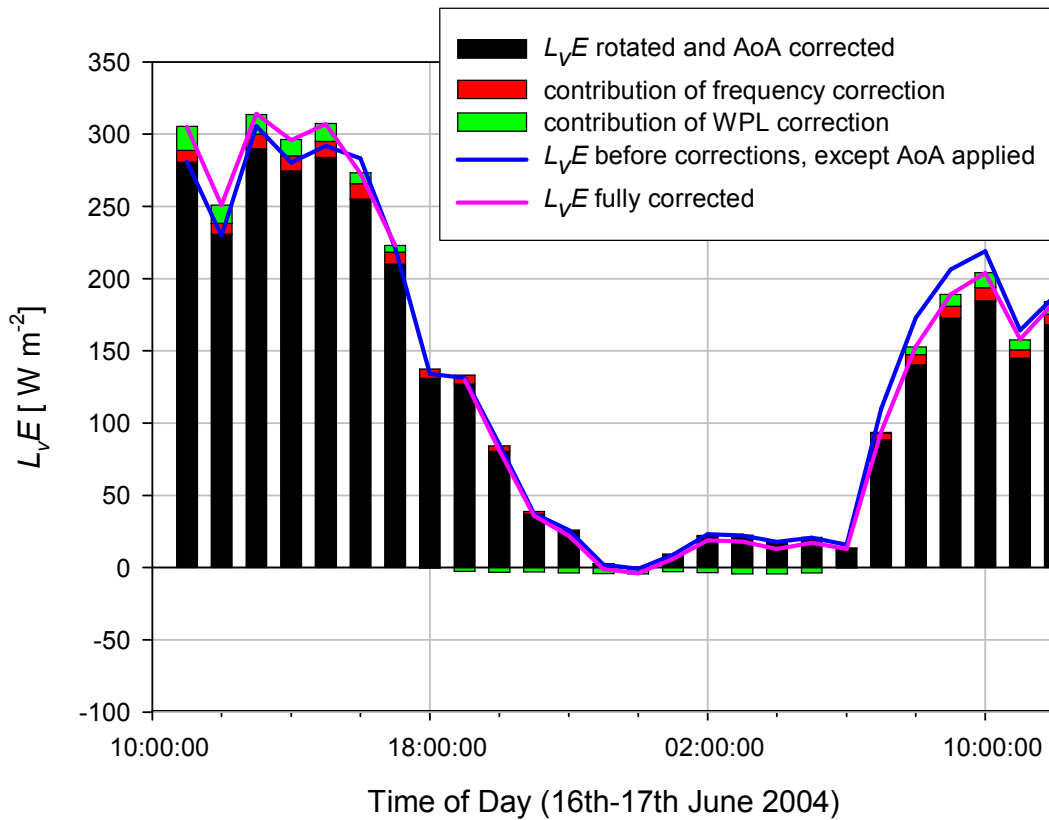


**Figure A 2.** The analysis of the relative contributions to  $L_v E$  of specific data processing steps (see text for full explanation).

### *Angle-of-Attack Recalibration of the Sonic Anemometer*

The Angle-of-Attack (AoA) sonic recalibration (Gash and Dolman, 2003) increases the flux magnitudes by 6 %. This is reasonable as the recalibration increases the magnitude of the vertical wind-speed component ( $w$ ) for angles-of-attack outside of the manufacturer's specification of  $\pm 20^\circ$  from the

horizontal, increasing all flux magnitudes. For the small amount of data tested, there is a linear gain in the fluxes with zero scatter. This suggests that the improved calibration can be retrospectively applied to mean data (at least for this site, under similar conditions of turbulence), although it was derived for the correction of raw, instantaneous sonic anemometer measurements, and has a non-linear dependence on the AoA.

### *Accounting for Sensor Lags*

Proper account must be taken of the spatial separation of the sonic anemometer (Solent R3) and the gas analyser (LI7500, Figure A 3) (Kristensen et al., 1997), as the EC method relies on the observations being at the same point in space and time. Due to electronic sensor delay, and variable time of passage of air between the sensors, there is a lag (and in some circumstances a lead) between the data of the LI7500 and that of the Solent R3. The accepted method to deal with this problem, is to seek the highest correlation between the sonic temperature and the gas data, whilst adjusting the lag time. This is done in a carefully controlled way, within expected bounds. It is very important to maintain physically realistic lags, as the peak of the correlation is often not well defined and there may be more than one peak. Tests were conducted using a fixed lag (just accounting for electronic delay), this gives a 23% increase for  $L_vE$  and 40% for the  $CO_2$  flux ( $FCO_2$ ).  $H$  also increases by 5%, probably due to the humidity flux correction to the sonic sensible heat flux. Secondly, the method seeking the maximum correlation was used, resulting in a further increase in  $L_vE$  of 4% and  $FCO_2$  of 8%. There was no significant change in  $H$ . This method typically found

gas-signal lags of 300 or 350 ms, depending on wind speed and direction. As data were sampled at 20 Hz, the maximum resolution of the lag time was 50 ms.



**Figure A 3. Spring Wheat Flux Station Showing Sensor Separation**

### *The Effect of the Detrending Method*

Linear block means are sometimes preferred over the auto-regressive moving average (ARMA) to avoid high pass filtering effects (and loss of low frequency flux), similar to the justification for the PF method. Again for this site, it is expected that this may result in more flux, but that the low frequency contributions are in any case quite small.

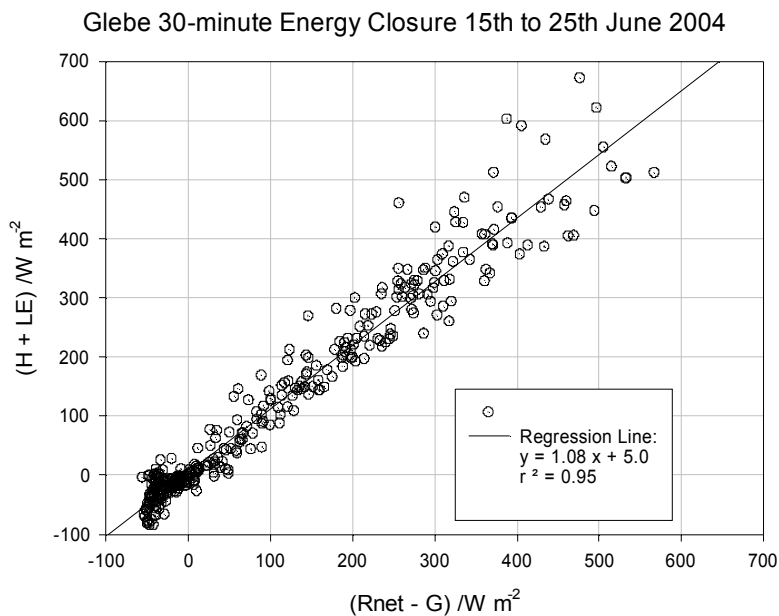
It was found that by applying a 30-minute block mean detrend, compared to the ARMA (with 10-minute time constant), there were increases of 1 % in  $H$ , 3 % in  $L_v E$ , and 2 % in  $FCO_2$ .

### *Frequency Loss Corrections*

The test data used here from the grass/red clover field (GC) were measured at a height of 2.34 m, relatively close to the fairly smooth surface, under conditions of relatively high wind speeds. This implies that the eddies measured will be small and that the low frequency part of the spectrum (with time constants greater than 10 minutes) will contribute very little turbulent energy (Rannik, 2001), minimising the low-frequency correction. Modern fast-response sonic anemometers with 20 Hz sampling also reduce the high frequency correction. Both low and high frequency corrections are thus quite small, of the order of a few percent.

## A1.3: Validation of EC Measurements by Closure of the Surface Energy Balance

Figure A 4. Energy balance closure for the Glebe grass/red clover (GC) field prior to LAS experiment when a LI7500 was installed at this EC



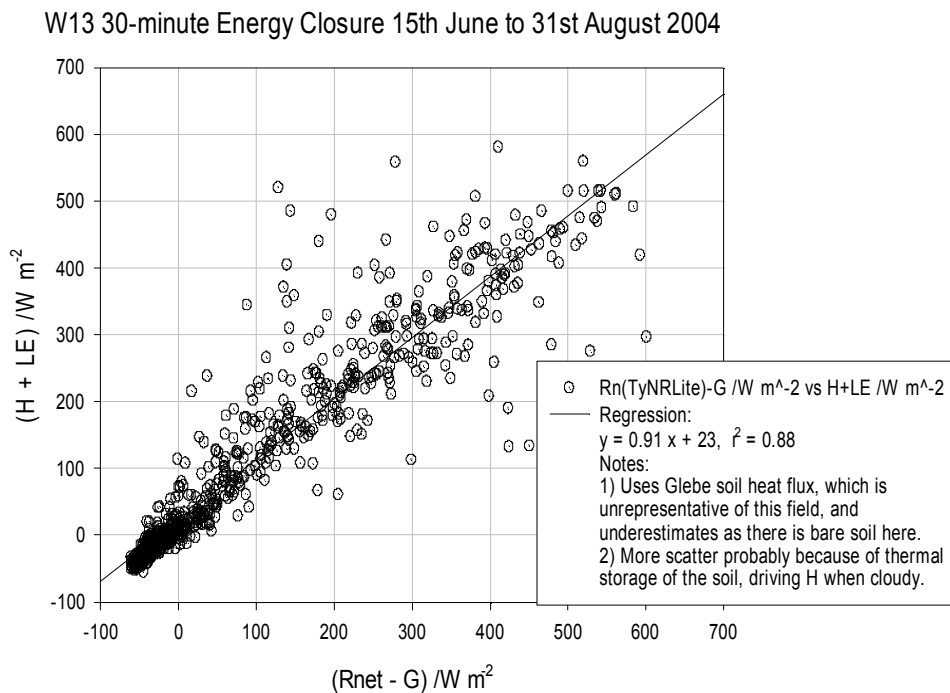
A good test of the performance of the EC technique for a particular site is to test the surface energy balance closure when all components ( $R_n$ ,  $H$ ,  $L_vE$  and  $G$ ) have been measured directly.

For the GC field the energy balance closure was tested with available  $L_vE$  data over a period prior to installation of the Spring Wheat EC system, due to a limited number of LI7500s, thus the energy balance closure tests were not

all concurrent with the same meteorological conditions. In particular, there are fewer data at higher energy fluxes for the spring wheat (SW) field.

Figure A 4 shows a small over-closure (+8%) for the GC field, which is better closed than most published results that show larger under-closure, in some cases greater than -20%. This is likely due to (a) favourable measurement conditions i.e. the turbulence spectrum is well represented by the measurements and (b) careful application of the most appropriate processing methods (very few published results use the AoA recalibration, and

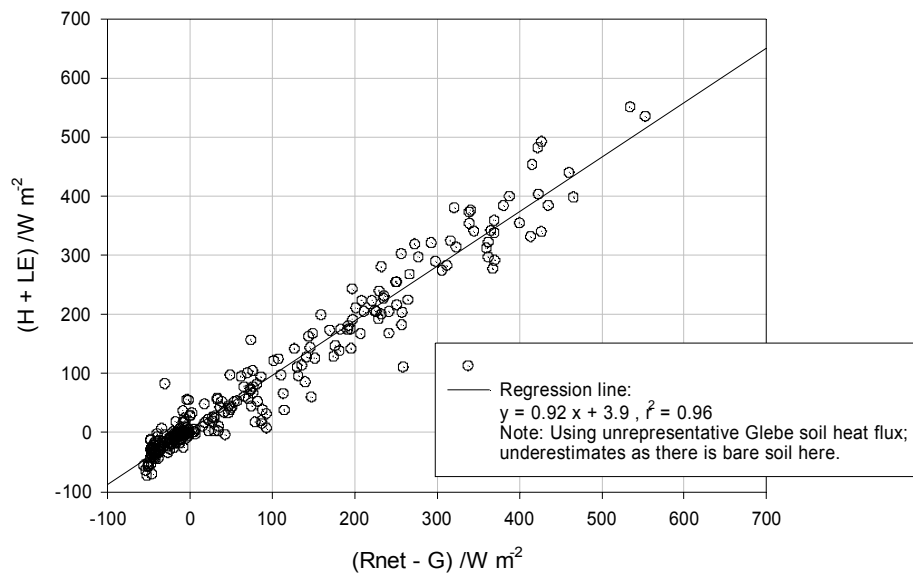
**Figure A 5. Energy balance closure for winter wheat (WW) field.**



sometimes sensor lag times are not accounted for properly.)

**Figure A 6. Energy balance closure for spring wheat (SW) field.**

Spring Wheat 30-minute Energy Closure 2nd July to 16th August 2004



The energy balance closure for winter wheat (WW) is shown in Figure A 5, for the period from mid-Summer to senescence. Here the closure is also good (-9 %), although the uncertainty is higher for  $G$ , as measurements from the GC field (below a grass/clover canopy) were used. It is expected that the energy balance closure would be higher if more representative  $G$  data was available.

The spring wheat (SW) EC data has similarly good closure (-8 %) to that of the WW (Figure A 6), also using the GC field  $G$ . It is not possible to test the closure of W16, as  $L_vE$  was not directly measured, but since very similar methodology and instrumentation was used, these measurements should also be valid. Overall, after careful quality control, confidence is then high in the EC and supporting meteorological and soil measurements, except for the noted omission of  $G$  measurements for the crop fields, which increases the uncertainty of their energy balances.

## References

- Andreas, E., 1989. Two-wavelength method of measuring path-averaged turbulent surface heat fluxes. *Journal of Atmospheric and Oceanic Technology*, 6: 280-292.
- Arya, S.P., 1988. Introduction to micrometeorology. International geophysics series, v. 42. Academic Press, San Diego.
- Beyrich, F., de Bruin, H.A.R., Meijninger, W.M.L., Schipper, J.W. and Lohse, H., 2002. Results from one-year continuous operation of a large aperture scintillometer over a heterogeneous land surface. *Boundary-Layer Meteorology*, 105(1): 85-97.
- Beyrich, F., Kouznetsov, R.D., Leps, J.P., Ludi, A., Meijninger, W.M.L. and Weisensee, U., 2005. Structure parameters for temperature and humidity from simultaneous eddy-covariance and scintillometer measurements. *Meteorologische Zeitschrift*, 14(5): 641-649.
- Beyrich, F., Leps, J.P., Mauder, M., Bange, J., Foken, T., Huneke, S., Lohse, H., Ludi, A., Meijninger, W.M.L., Mironov, D., Weisensee, U. and Zittel, P., 2006. Area-averaged surface fluxes over the litfass region based on eddy-covariance measurements. *Boundary-Layer Meteorology*, 121(1): 33-65.
- Beyrich, F. and Engelbart, D.A.M., 2008. Ten years of operational boundary-layer measurements at the Richard-Assmann Observatory Lindenberg: The role of remote sensing. In: J. Mann et al. (Editors), 14th International Symposium for the Advancement of Boundary Layer Remote Sensing, Copenhagen, DENMARK, pp. U223-U228.
- Blyth, E.M., Evans, J.G., Finch, J.W., Bantges, R. and Harding, R.J., 2006. Spatial variability of the English agricultural landscape and its effect on evaporation. *Agricultural and Forest Meteorology*, 138(1-4): 19-28.

- Broersen, P.M.T. and de Waele, S., 2006. Automatic Spectral Analysis. <http://www.mathworks.com/matlabcentral/> pp. Matlab Library.
- Chehbouni, A., Hartogensis, O., Kerr, Y.H., Hipps, L., Brunel, J.P., Watts, C., Rodriguez, J., Boulet, G., Dedieu, G. and de Bruin, H., 1998. Sensible heat flux measurements using a large aperture scintillometer over heterogeneous surface. Special Symposium on Hydrology: 20-23.
- Chehbouni, A., Watts, C., Lagouarde, J.P., Kerr, Y.H., Rodriguez, J.C., Bonnefond, J.M., Santiago, F., Dedieu, G., Goodrich, D.C. and Unkrich, C., 2000. Estimation of heat and momentum fluxes over complex terrain using a large aperture scintillometer. Agricultural and forest meteorology, 105(1-3): 215-226.
- Clifford, S.F., 1971. Temporal-Frequency Spectra for a Spherical Wave Propagating Through Atmospheric Turbulence. Journal of the Optical Society of America, 61(10): 1285-&.
- Clifford, S.F., Ochs, G.R. and Lawrence, R.S., 1974. Saturation of Optical Scintillation by Strong Turbulence. Journal of the Optical Society of America, 64(2): 148-154.
- Culf, A.D., 2000. Examples of the effects of different averaging methods on carbon dioxide fluxes calculated using the eddy correlation method. Hydrology And Earth System Sciences, 4(1): 193-198.
- de Bruin, H.A.R., vandenHurk, B. and Kohsiek, W., 1995. The scintillation method tested over a dry vineyard area. Boundary-Layer Meteorology, 76(1-2): 25-40.
- de Bruin, H.A.R., Nieveen, J.P., deWekker, S.F.J. and Heusinkveld, B.G., 1996. Large aperture scintillometry over a 4.8 KM path for measuring areally-average sensible heat flux; A case study. 22nd Conference on Agricultural & Forest Meteorology with Symposium on Fire & Forest Meteorology/12th Conference on Biometeorology & Aerobiology: 153-156.
- de Bruin, H.A.R., Moene, A.F. and Bosveld, F.C., 2004. An integrated MSG-scintillometer network system to monitor sensible and latent heat fluxes. Proceedings of the Second MSG RAO Workshop, 582: 137-142.
- de Bruin, H.R., Kohsiek, W. and Vandenhurk, B.M., 1993. A verification of some methods to determine the fluxes of momentum, sensible heat, and water-vapor using standard-deviation and structure parameter of

- scalar meteorological quantities. *Boundary-Layer Meteorology*, 63(3): 231-257.
- Evans, J.G. and de Bruin, H.A.R., 2009. The Effective Height for the Calculation of Heat Fluxes from Scintillometry over Complex Topography. In preparation.
- Ezzahar, J., Chehbouni, A., Hoedjes, J.C.B. and Chehbouni, A., 2007. On the application of scintillometry over heterogeneous grids. *Journal of Hydrology*, 334(3): 493-501.
- Field, M., 1983. The Meteorological-Office Rainfall And Evaporation Calculation System - MORECS. *Agricultural Water Management*, 6(2-3): 297-306.
- Finch, J.W. and Harding, R.J., 1998. A comparison between reference transpiration and measurements of evaporation for a riparian grassland site. *Hydrology and Earth System Sciences*, 2(1): 129-136.
- Foken, T., 2008. The energy balance closure problem: An overview. *Ecological Applications*, 18(6): 1351-1367.
- Gash, J.H.C. et al., 1997. The variability of evaporation during the HAPEX-Sahel intensive observation period. *Journal of Hydrology*, 189(1-4): 385-399.
- Gash, J.H.C. and Dolman, A.J., 2003. Sonic anemometer (co)sine response and flux measurement I. The potential for (co)sine error to affect sonic anemometer-based flux measurements. *Agricultural and Forest Meteorology*, 119(3-4): 195-207.
- Green, A.E., Green, S.R., Astill, M.S. and Caspari, H.W., 2000. Estimating latent heat flux from a vineyard using scintillometry. *Terrestrial Atmospheric And Oceanic Sciences*, 11(2): 525-542.
- Green, A.E., Astill, M.S., McAneney, K.J. and Nieveen, J.P., 2001. Path-averaged surface fluxes determined from infrared and microwave scintillometers. *Agricultural and Forest Meteorology*, 109(3): 233-247.
- Hartogensis, O.K., Watts, C.J., Rodriguez, J.C. and de Bruin, H.A.R., 2003. Derivation of an effective height for scintillometers: La Poza experiment in Northwest Mexico. *Journal of Hydrometeorology*, 4(5): 915-928.
- Hecht, E., 1988. *Optics / Eugene Hecht ; - 3rd ed. Addison-Wesley, Reading, Mass.*

- Herbst, M., Roberts, J.M., Rosier, P.T.W., Taylor, M.E. and Gowing, D.J., 2007. Edge effects and forest water use: A field study in a mixed deciduous woodland. *Forest Ecology and Management*, 250(3): 176-186.
- Hill, R.J. and Clifford, S.F., 1978. Modified Spectrum of Atmospheric-Temperature Fluctuations and Its Application to Optical Propagation. *Journal of the Optical Society of America*, 68(7): 892-899.
- Hill, R.J. and Ochs, G.R., 1978. Fine Calibration of Large-Aperture Optical Scintillometers and an Optical Estimate of Inner Scale of Turbulence. *Applied Optics*, 17(22): 3608-3612.
- Hill, R.J., Clifford, S.F. and Lawrence, R.S., 1980. Refractive Index and Absorption Fluctuations in the Infrared Caused by Temperature, Humidity and Pressure Fluctuations. *J. Opt. Soc. Am.*, 70: 1192-1205.
- Hill, R.J., Bohlander, R.A., Clifford, S.F., Mcmillan, R.W., Priestley, J.T. and Schoenfeld, W.P., 1988. Turbulence-Induced Millimeter-Wave Scintillation Compared with Micrometeorological Measurements. *IEEE Transactions on Geoscience and Remote Sensing*, 26(3): 330-342.
- Hill, R.J., 1992. Review of Optical Scintillation Methods of Measuring the Refractive-Index Spectrum, Inner Scale and Surface Fluxes. *Waves in Random Media*, 2(3): 179-201.
- Hill, R.J., Ochs, G.R. and Wilson, J.J., 1992. Measuring Surface-Layer Fluxes of Heat and Momentum Using Optical Scintillation. *Boundary-Layer Meteorology*, 58(4): 391-408.
- Jenkins, F.A. and White, H.E., 1957. *Fundamentals of optics*. McGraw-Hill, New York.
- Kesteren, A.J.H.v., 2008. *Sensible and Latent Heat Fluxes with Optical and Millimetre Wave Scintillometers: A Theory Review and the Chilbolton Experiment*, Wageningen University, Wageningen, The Netherlands, 99 pp.
- Kleissl, J., Gomez, J., Hong, S.H., Hendrickx, J.M.H., Rahn, T. and Defoor, W.L., 2008. Large aperture scintillometer intercomparison study. *Boundary-Layer Meteorology*, 128(1): 133-150.
- Kleissl, J., Watts, C.J., Rodriguez, J.C., Naif, S. and Vivoni, E.R., 2009. Scintillometer Intercomparison Study-Continued. *Boundary-Layer Meteorology*, 130(3): 437-443.

- Kohsiek, W., 1982. Measuring  $C_t^2$ ,  $C_q^2$ , and  $C_{tq}$  in the Unstable Surface-Layer, and Relations to the Vertical Fluxes of Heat and Moisture. *Boundary-Layer Meteorology*, 24(1): 89-107.
- Kohsiek, W. and Herben, M.H.A.J., 1983. Evaporation Derived from Optical and Radiowave Scintillation. *Applied Optics*, 22(17): 2566-2570.
- Kohsiek, W., 1987. A 15 cm aperture LED scintillometer for  $C_n^2$  and crosswind measurements. Scientific Report WR 87-3, KNMI.
- Kohsiek, W., Meijninger, W.M.L., Moene, A.F., Heusinkveld, B.G., Hartogensis, O.K., Hillen, W. and de Bruin, H.A.R., 2002. An extra large aperture scintillometer for long range applications. *Boundary-Layer Meteorology*, 105(1): 119-127.
- Lagouarde, J.P., McAneney, K.J. and Green, A.E., 1996. Scintillometer measurements of sensible heat flux over heterogeneous surfaces. In: J.B. Stewart, E.T. Engman, R.A. Feddes and Y. Kerr (Editors), *Scaling up in hydrology using remote sensing*. BAHC, ISLSCP, Institute of Hydrology. John Wiley & Sons. New York (1996). pp. 147-160.
- Lagouarde, J.P., Bonnefond, J.M., Kerr, Y.H., McAneney, K.J. and Irvine, M., 2002. Integrated sensible heat flux measurements of a two-surface composite landscape using scintillometry. *Boundary-Layer Meteorology*, 105(1): 5-35.
- Lagouarde, J.P., Irvine, M., Bonnefond, J.M., Grimmond, C.S.B., Long, N., Oke, T.R., Salmond, J.A. and Offerle, B., 2006. Monitoring the sensible heat flux over urban areas using large aperture scintillometry: Case study of Marseille city during the Escompte experiment. *Boundary-Layer Meteorology*, 118(3): 449-476.
- Lawrence, R.S. and Strohbehm, J.W., 1970. A Survey of Clear-Air Propagation Effects Relevant to Optical Communications. *Proceedings of the Institute of Electrical and Electronics Engineers*, 58(10): 1523-1545.
- Lawrence, R.S., Ochs, G.R. and Clifford, S.F., 1972. Use of scintillations to measure average wind across a light-beam. *Applied Optics*, 11(2): 239-&.
- Lee, X., Massman, W.J., Law, B.E. and NetLibrary, I., 2004. *Handbook of micrometeorology a guide for surface flux measurement and analysis*. Kluwer Academic Publishers, Dordrecht; Boston; London.
- Lüdi, A., 2002. *Line-of-Sight Propagation through the Turbulent Earth Atmosphere at Millimeter Wavelengths*, Bern University, Bern.

- Lüdi, A., Beyrich, F. and Matzler, C., 2005a. Determination of the turbulent temperature-humidity correlation from scintillometric measurements. *Boundary-Layer Meteorology*, 117(3): 525-550.
- Lüdi, A., Magun, A. and Costa, J.E.R., 2005b. First retrieval of vertical profiles of turbulence characteristics and horizontal wind velocity from solar transmission measurements at 212 and 405 GHz. *Applied Optics*, 44(6): 1067-1076.
- Mauder, M. and Foken, T., 2006. Impact of post-field data processing on eddy covariance flux estimates and energy balance closure. *Meteorologische Zeitschrift*, 15(6): 597-609.
- Mauder, M., Liebethal, C., Gockede, M., Leps, J.P., Beyrich, F. and Foken, T., 2006. Processing and quality control of flux data during LITFASS-2003. *Boundary-Layer Meteorology*, 121(1): 67-88.
- Mauder, M., Foken, T., Clement, R., Elbers, J.A., Eugster, W., Grunwald, T., Heusinkveld, B. and Kolle, O., 2008. Quality control of CarboEurope flux data - Part 2: Inter-comparison of eddy-covariance software. *Biogeosciences*, 5(2): 451-462.
- McAneney, K.J., Green, A.E. and Astill, M.S., 1995. Large-aperture scintillometry - the homogeneous case. *Agricultural and forest meteorology*, 76(3-4): 149-162.
- McMillen, R.T., 1988. An eddy-correlation technique with extended applicability to non-simple terrain. *Boundary-Layer Meteorology*, 43(3): 231-245.
- Meijninger, W.M.L. and de Bruin, H.A.R., 2000. The sensible heat fluxes over irrigated areas in western Turkey determined with a large aperture scintillometer. *Journal of Hydrology*, 229(1-2): 42-49.
- Meijninger, W.M.L., Green, A.E., Hartogensis, O.K., Kohsiek, W., Hoedjes, J.C.B., Zuurbier, R.M. and de Bruin, H.A.R., 2002a. Determination of area-averaged water vapour fluxes with large aperture and radio wave scintillometers over a heterogeneous surface - Flevoland field experiment. *Boundary-Layer Meteorology*, 105(1): 63-83.
- Meijninger, W.M.L., Hartogensis, O.K., Kohsiek, W., Hoedjes, J.C.B., Zuurbier, R.M. and de Bruin, H.A.R., 2002b. Determination of area-averaged sensible heat fluxes with a large aperture scintillometer over a heterogeneous surface - Flevoland field experiment. *Boundary-Layer Meteorology*, 105(1): 37-62.

- Meijninger, W.M.L., 2003. Surface fluxes over natural landscapes using scintillometry, Wageningen University, Wageningen, The Netherlands, 170 pp.
- Meijninger, W.M.L., Beyrich, F., Luedi, A., Kohsiek, W. and de Bruin, H.A.R., 2006. Scintillometer-based turbulent fluxes of sensible and latent heat over a heterogeneous land surface - A contribution to LITFASS-2003. *Boundary-Layer Meteorology*, 121(1): 89-110.
- Moene, A.F., 2003. Effects of water vapour on the structure parameter of the refractive index for near-infrared radiation. *Boundary-Layer Meteorology*, 107(3): 635-653.
- Moene, A.F., Meijninger, W.M.L., Hartogensis, O.K., Kohsiek, W. and de Bruin, H.A.R., 2004. A review of the relationships describing the signal of a Large Aperture Scintillometer, Wageningen University, Wageningen, the Netherlands.
- Monin, A.S. and Yaglom, A.M., 1971. *Statistical Fluid Mechanics: Mechanics of Turbulence*, 1. The MIT Press, Cambridge, Mass., 782 pp.
- Murray, T. and Verhoef, A., 2007a. Moving towards a more mechanistic approach in the determination of soil heat flux from remote measurements - I. A universal approach to calculate thermal inertia. *Agricultural and Forest Meteorology*, 147(1-2): 80-87.
- Murray, T. and Verhoef, A., 2007b. Moving towards a more mechanistic approach in the determination of soil heat flux from remote measurements - II. Diurnal shape of soil heat flux. *Agricultural and Forest Meteorology*, 147(1-2): 88-97.
- Nakai, T., van der Molen, M.K., Gash, J.H.C. and Kodama, Y., 2006. Correction of sonic anemometer angle of attack errors. *Agricultural and Forest Meteorology*, 136(1-2): 19-30.
- Newton, I., 1730. *Opticks or, a treatise of the reflections, refractions, inflections and colours of light*. The fourth edition, corrected. By Sir Isaac Newton, Knt. printed for William Innys, London, pp. [8],382,[2]p.,plates.
- Nieveen, J.P., Green, A.E. and Kohsiek, W., 1998. Using a large-aperture scintillometer to measure absorption and refractive index fluctuations. *Boundary-Layer Meteorology*, 87(1): 101-116.

- Ochs, G.R. and Clifford, S.F.J., 1972. Saturation of optical-amplitude scintillation at 0.6328  $\mu\text{m}$  wavelength. *Journal of the Optical Society of America*, 62(5): 728-&.
- Ochs, G.R., Clifford, S.F. and Wang, T.J., 1976. Laser wind sensing - effects of saturation of scintillation. *Applied Optics*, 15(2): 403-408.
- Oncley, S.P., Foken, T., Vogt, R., Kohsiek, W., de Bruin, H.A.R., Bernhofer, C., Christen, A., van Gorsel, E., Grantz, D., Feigenwinter, C., Lehner, I., Liebenthal, C., Liu, H., Mauder, M., Pitacco, A., Ribeiro, L. and Weidinger, T., 2007. The Energy Balance Experiment EBEX-2000. Part I: Overview and energy balance. *Boundary-Layer Meteorology*, 123(1): 1-28.
- Otto, W.D., Hill, R.J., Sarma, A.D., Wilson, J.J., Andreas, E.L., Gosz, J.R. and Moore, D.I., 1996. Results of the millimeter-wave instrument operated at Sevilleta, New Mexico, NOAA Environmental Research Laboratories, Boulder CO.
- Panofsky, H.A. and Dutton, J.A., 1984. Atmospheric turbulence models and methods for engineering applications. John Wiley & Sons, Inc.
- Poggio, L.P., Furger, M., Prevot, A.S.H., Graber, W.K. and Andreas, E.L., 2000. Scintillometer wind measurements over complex terrain. *Journal of Atmospheric and Oceanic Technology*, 17(1): 17-26.
- R, 2008. R: A Language and Environment for Statistical Computing. R Foundation for Statistical Computing, Vienna, Austria.
- Sarma, A.D. and Hill, R.J., 1988. A millimeter wave scintillometer for flux measurements. NOAA Environmental Research Laboratories, Boulder, CO, Boulder, CO.
- Schuepp, P.H., Leclerc, M.Y., Macpherson, J.I. and Desjardins, R.L.J., 1990. Footprint prediction of scalar fluxes from analytical solutions of the diffusion equation. *Boundary-layer Meteorology*, 50(1-4): 373.
- Schuttemeyer, D., Moene, A.F., Holtslag, A.A.M., de Bruin, H.A.R. and de Giesen, N.V., 2006. Surface fluxes and characteristics of drying semi-arid terrain in West Africa. *Boundary-Layer Meteorology*, 118(3): 583-612.
- Stull, R.B., 1988. *An Introduction to Boundary Layer Meteorology*. Kluwer Academic Publishers.

- Tatarski, V.I., 1961. Wave Propagation in a Turbulent Medium. McGraw-Hill, 1961, New York.
- Tillman, J.E., 1972. The Indirect Determination of Stability, Heat and Momentum Fluxes in the Atmospheric Boundary Layer from Simple Scalar Variables During Dry Unstable Conditions. *Journal of Applied Meteorology*, 11(5): 783-792.
- Townsend, A.A.R., 1980. The Structure of Turbulent Shear Flow. Cambridge Monographs on Mechanics. Cambridge University Press, Cambridge, 444 pp.
- Verhoef, A. and Campbell, C.L., 2005. Evaporation measurement. In: M.G. Anderson (Editor), *Encyclopedia of hydrological sciences*. J. Wiley, Chichester, West Sussex, England; Hoboken, NJ, pp. pp 589-601.
- Von Randow, C., Kruijt, B., Holtslag, A.A.M. and de Oliveira, M.B.L., 2008. Exploring eddy-covariance and large-aperture scintillometer measurements in an Amazonian rain forest. *Agricultural and Forest Meteorology*, 148(4): 680-690.
- Wang, T., Ochs, G.R. and Lawrence, R.S., 1981. Wind measurements by the temporal cross-correlation of the optical Scintillations. *Applied Optics*, 20(23): 4073-4081.
- Wang, T.I., Ochs, G.R. and Clifford, S.F., 1978. Saturation-resistant optical scintillometer to measure C-N(2). *Journal of the Optical Society of America*, 68(3): 334-338.
- Wesely, M.L., 1976. Combined effect of temperature and humidity fluctuations on refractive-index. *Journal of Applied Meteorology*, 15(1): 43-49.
- Wheeler, A.D., 2001. *Electromagnetic scintillation*. Cambridge University Press, Cambridge.
- Wheeler, A.D., 2006. *Electromagnetic scintillation : weak scattering*. Cambridge Univ Press, Cambridge.
- Wyngaard, J.C., Izumi, Y. and Collins, S.A., 1971. Behavior of Refractive-Index-Structure Parameter near Ground. *Journal of the Optical Society of America*, 61(12): 1646-&.